crystals

MDPI

Review

A Review of Nanocarbon-Based Anode Materials for Lithium-Ion Batteries

Nagaraj Nandihalli

Critical Materials Innovation Hub, Ames National Laboratory, U.S. Department of Energy, Iowa State University, Ames, IA 50011, USA; nagaraj.nandi001@umb.edu

Abstract: Renewable and non-renewable energy harvesting and its storage are important components of our everyday economic processes. Lithium-ion batteries (LIBs), with their rechargeable features, high open-circuit voltage, and potential large energy capacities, are one of the ideal alternatives for addressing that endeavor. Despite their widespread use, improving LIBs' performance, such as increasing energy density demand, stability, and safety, remains a significant problem. The anode is an important component in LIBs and determines battery performance. To achieve high-performance batteries, anode subsystems must have a high capacity for ion intercalation/adsorption, high efficiency during charging and discharging operations, minimal reactivity to the electrolyte, excellent cyclability, and non-toxic operation. Group IV elements (Si, Ge, and Sn), transition-metal oxides, nitrides, sulfides, and transition-metal carbonates have all been tested as LIB anode materials. However, these materials have low rate capability due to weak conductivity, dismal cyclability, and fast capacity fading owing to large volume expansion and severe electrode collapse during the cycle operations. Contrarily, carbon nanostructures (1D, 2D, and 3D) have the potential to be employed as anode materials for LIBs due to their large buffer space and Li-ion conductivity. However, their capacity is limited. Blending these two material types to create a conductive and flexible carbon supporting nanocomposite framework as an anode material for LIBs is regarded as one of the most beneficial techniques for improving stability, conductivity, and capacity. This review begins with a quick overview of LIB operations and performance measurement indexes. It then examines the recently reported synthesis methods of carbon-based nanostructured materials and the effects of their properties on high-performance anode materials for LIBs. These include composites made of 1D, 2D, and 3D nanocarbon structures and much higher Li storage-capacity nanostructured compounds (metals, transitional metal oxides, transition-metal sulfides, and other inorganic materials). The strategies employed to improve anode performance by leveraging the intrinsic features of individual constituents and their structural designs are examined. The review concludes with a summary and an outlook for future advancements in this research field.

Keywords: Li-ion battery; anode material; graphene; hollow carbon nanosphere; carbon nanofiber

Citation: Nandihalli, N. A Review of Nanocarbon-Based Anode Materials for Lithium-Ion Batteries. *Crystals* **2024**, *14*, 800. https://doi.org/10.3390/cryst14090800

Academic Editors: Ram S. Katiyar and Zhipeng Yu

Received: 1 August 2024
Revised: 29 August 2024
Accepted: 5 September 2024
Published: 10 September 2024

1. Introduction

Energy storage devices are a vital technology for the widespread use of electric vehicles and renewable energy harvesting. The demand for Internet of Things (IoT) and wearables continues to grow, with all domains of our lives being increasingly connected to the internet, including every gadget that requires a secondary energy storage device. Health sensors, in conjunction with WiFi and a miniaturized energy storage device, can be used to monitor health remotely [1,2]. Many health sensors do not require high power to operate. At present, a temperature sensor can consume 71 nW of power [3]. Motivated by increasing healthcare costs, implementations of wearable health monitoring systems ranging from simple pulse monitors to activity and sleep quality monitors, and even implantable sensors, have all stimulated the design and fabrication of low-cost secondary batteries [4,5]. As a result, these energy storage devices must be available in a variety of shapes and sizes to

complement the style and functionality of their host devices. Lithium-ion batteries (LIBs) are among the most promising energy storage systems because of their excellent energy storage efficiency. The LIB is a type of secondary battery (i.e., rechargeable battery). Lithium (Li) has a high theoretical specific capacity (3860 mAh/g), a low redox potential (−3.04 V), and a low density (0.59 g/cm^3). A primary battery provides energy until its storage capacity is depleted and then discarded. The anode plays a key function in LIBs and has an impact on battery performance. The physical and chemical properties of the anode material must be optimized as they influence the battery's performance [6]. Anode materials must meet three main requirements: (a) the potential for Li insertion and extraction in the anode versus Li must be as small as possible; (b) the amount of Li that can be accepted by the anode material should be as high as possible to attain a high specific capacity; and (c) the anode hosts must withstand repeated Li insertion and extraction without structural damage to achieve a long cycle life.

Graphite has been a common choice for anode materials in LIBs because of its superior cycling stability, flat discharge plateaus, and high electronic (in-plane) conductivity owing to delocalized π-bonds and an appropriate structure for Li-ion intercalation and diffusion [7,8]. In graphite, six carbon atoms can hold one Li to form LiC_6 with the intercalation of Li between carbon layers. Based on the reaction to form the LiC_6 compound, $Li^+ + 6C + e^- \rightarrow LiC_6$, LIB anodes made of graphite material have a theoretical specific capacity of 372 mA h/g, an observed capacity of 280–330 mAh/g, and a low charging–discharging rate based on the type of graphite employed [9]. Therefore, it is limited in its ability to meet growing energy demand. Further, since graphite's theoretical capacity has been nearly reached in practice, there is a strong interest in developing other anode replacements.

In the past, metals/metalloids (Sn, Si, Ge, Sb), metal oxides, and metal-phosphides/sulfides/nitrides (P, S, N) have been used as anode materials in LIBs. However, these materials have low rate capability due to weak conductivity [10], dismal cyclability, fast capacity fading owing to large volume expansion and shrinking leading to pulverization of the electrode, and severe electrode collapse throughout the cycle operations. Carbon is the most commonly used anode material. This is the principal material of choice, and it is the most commercially successful anode material. Further, carbon in the anode provides better electronic conductivity, a large surface area, and mechanical strength, allowing for superior electron transport and rate capability [11]. It has been shown that the reversible capacity of graphene-based materials can be as high as 1000 mAh/g [12,13]. Nanocarbons such as mesoporous graphene (MPG), carbon tubular nanostructures (CTNs), and hollow carbon nanoboxes (HCBs) are promising possibilities for LIB anodes. These nanocarbon anodes exhibit high capacities of around 1100, 600, and 500 mA h/g at 0.1 A/g for MPG, CTN, and HCB, respectively. MPG, CTN, and HCB anodes retain their capacities of 181, 141, and 139 mA h/g at 4 A/g, respectively [14]. Furthermore, these nanocarbon anodes exhibit remarkable cycling stability beyond 1000 cycles, indicating the formation of a passivating layer (a solid electrolyte interphase) that facilitates long-term cycling [14]. Nanocarbons with graphene layers that undergo the lithiation/delithiation process, a high ratio of graphite edge structure, and a large surface area that allows capacitive behavior provide high capacity and increased rate capability. High in-plane conductivity in Gr and the vertical interlayer spacing promotes improved ion intercalation, enhancing capacity and rate capability. Carbon shells in carbon nanospheres allow for volume expansion and contraction during charge storage while also assisting electron transport. The combination of these two factors results in increased cycling stability and better rate performance. The 1D carbon also supports Li-ion transport because of its high conductivity and 1D tubular architecture. Carbon shields the Li-ion from dendritic development during recharging [15]. The creation of an ideal porous structure in nanocarbons would provide the chemistry and structure needed to store Li-ions and guarantee the electrolyte ions' accessibility while also reducing transport pathways [16].

Given the advantages and disadvantages of nanocarbons and other high-Li storage materials such as metals and transitional metal oxides, the synergetic combination of these materials as nanocomposites can produce superior outcomes when compared to individual constituents. This review examines the recently reported synthesis methods of carbon-based nanostructure composite materials and the effects of their attributes on high-performance anode materials for LIBs. These include composites with various nanocarbon architectures in combination with nanostructured materials with significantly increased Li storage capacity. In particular, 1D structures (CNTs, carbon nanofibers, and carbon nanorods), 2D structures (graphene oxide and reduced graphene oxide, doped and undoped graphene), and 3D structures (carbon nanospheres, carbon-coated metal oxide nanospheres, core-shell structures, hollow hierarchical porous carbon spheres, doped-carbon-coated transition-metal oxides, and porous carbon-based anodes) are covered.

Basics of Lithium-Ion Batteries

Traditional LIBs are made up of four parts: positive electrodes (cathodes, e.g., $LiCoO_2$, $LiFePO_4$), negative electrodes (anodes, e.g., carbon), a separator, and an electrolyte, e.g., lithium salt/$LiPF_6$ (Figure 1a,b). During the charge and discharge processes, Li-ions move from the cathode to the anode. The charging process happens when Li-ions travel through the separator with the help of a conductive electrolyte from the Li metal oxide cathode to the carbon-based anode. When the cell is subjected to an external load, a discharging process occurs in which Li atoms intercalated in the anode lose electrons and transform into Li-ions, which then return to the associated counter-cathode [17]. Electrons that complete the half reaction traverse an external wire since electrolytes do not contain free electrons. The composition and structure of electrodes (both cathode and anode) are important aspects influencing battery performance. To create an electrode, conductive additives and active materials (e.g., carbon black, CNTs, carbon nanofibers (CNFs), graphene, and transitional metal oxides) are attached to a current collector made of metal (e.g., Cu or Al foil) with binders based on polymers. Between active materials and the current collector, conductive additives build a network that facilitates electron transfer, and the binder maintains the electrode's stability and integrity during battery cycling. Figure 1c depicts the procedures in sample preparation and electrochemical property characterization.

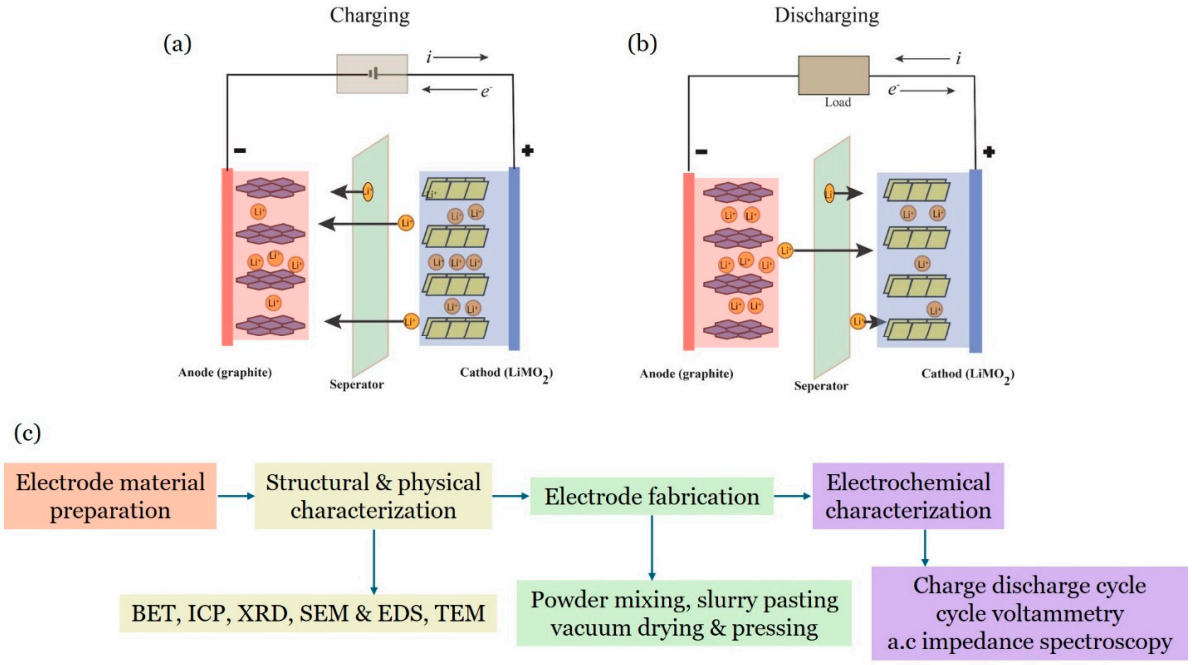

Figure 1. LIB in operation. (**a**) Illustration of a charging mechanism; (**b**) discharging mechanism; (**c**) generally employed technique used to fabricate anode material sample and its characterization techniques.

LIB performance is often measured using parameters, e.g., charging/discharging rate, specific/gravimetric capacity, specific energy, cycle stability, volumetric capacity, safety, and voltage profile. These parameters are impacted by several kinds of chemical and physical properties related to the material and electrode assembly. The specific (or gravimetric) capacity (mAh/g) relates to the quantity of energy capacity per unit mass of the battery. The volumetric capacity (mAh/cm^3) is the quantity of energy capacity per unit volume of the battery. The total energy within an electrode material can be expressed as the energy or charges per unit mass (specific energy, in Wh/kg) or energy per unit volume (energy density, in Wh/L). Power density is the rate at which an electrode material can deliver energy, and it is commonly expressed in per unit mass as specific power (W/kg) or per unit volume as power density (W/L). It determines how quickly a battery can provide energy. High-energy density batteries can store a larger amount of energy but may not deliver it rapidly.

The number of charge–discharge cycles before the battery significantly loses its energy is referred to as cyclability. The average capacity retention across multiple cycles is commonly referred to as cycle stability. Cycle stability is linked to the structural and chemical stability of the electrode materials [18]. A battery's rate of charge or discharge (C-rate) is defined as the time it takes to charge or discharge completely. For example, at 1C, it takes 1 h for the battery to fully discharge or release its maximum capacity [19], whereas at 2C, it takes 0.5 h.

Coulombic efficiency is defined as the ratio of discharge capacity to charge capacity throughout the same cycle. Initial coulombic efficiency (ICE) is an essential metric that describes the quality of the anode. It is a critical factor in full battery design since it influences the use of active materials and the weight of the assembled battery. The ICE of anode materials in half cells is determined by the ratio of the initial charge capacity to the initial discharge capacity, indicating their ability to prevent irreversible reactions and loss of capacity. This property is crucial for the practical use of anode materials in batteries, as it affects the available energy density. A low ICE value results in a low energy density of the battery. The formation of the solid–electrolyte interface (SEI) layer and the irreversible absorption of Li-ions within the anode materials contribute significantly to the low ICE of the intercalation type of anode [20]. A number of factors, including the basal to edge plane ratio, the chemical composition of the carbon surface, and the surface characteristics of the carbon (surface area and porosity), affect the formation of the SEI layer in carbon-based anodes like graphite and Gr. The SEI layer develops quickly on the edge plane and in carbon with the most surface area and defects. As a result, such characteristics can be tuned in order to obtain a low-capacity loss.

The electrical potential E (or voltage in V) at which electrode materials charge and discharge does not remain constant. Graphite usually has a rather flat discharge profile. For high-performance electronics, a flat working potential, comparable to graphite, is preferred.

2. One-Dimensional Carbon Nanocomposites Comprising Carbon Nanofiber (CNF), Carbon Nanotube (CNT), and Carbon Nanorod (CNR) Nanostructures

Nanostructured electrodes overcome the constraints of bulk crystalline expansion. It has been demonstrated that lowering the particle size of the material to the nanoscale can change the crystal structure and alter the process of volumetric expansion during lithiation [21]. CNTs have extremely high thermal conductivity, which improves composite electrode safety. CNTs have been found to have significantly higher Li capacity than graphite because of their unique structures and characteristics; they exhibit high conductivities (10^6 S/m and 10^5 S/m for SWCNTs and MWCNTs, respectively) and great tensile strength (~60 GPa) [22,23] and flexibility, which may improve battery cyclability. Because some carbonaceous materials can reversibly react with Li in LIB, CNTs have been proposed for use as Li storage materials [24,25].

When CNTs are utilized as anode materials, their morphology (number of defects, lengths, and diameters) has a significant impact on the electrochemical performance of LIBs.

CNT defects include sidewall holes, cap removal, and edge fragmentation. The presence of holes on CNT surfaces promotes improved intercalation and diffusion of Li-ions into the tubes, enhancing their capacity. Ball milling and chemical etching are two of the most frequent ways used to alter the morphology of CNTs. Short and defective CNTs can be produced via chemical etching, mechanical cutting, or a combination of the two. Chemical etching of CNTs is the treatment of CNTs with strong acids (such as HNO_3 and H_2SO_4). This procedure generates a large number of oxygen-containing groups, which destroys the CNT structure in the form of many defects [25]. Ball milling for a suitable period of time may boost CNTs' reversible capacity and coulombic efficiency [26]. However, both the mechanical ball-milling process and the chemical etching approach typically lead to a large loss of raw materials, inhomogeneous cutting with lengthy CNTs left, and the degradation of graphitic structure.

The mechanism by which Li-ions are stored in CNTs has been the subject of numerous investigations, including theoretical treatments [27–31]. Yang et al. investigated the electrochemical intercalation of Li into pristine end-closed CNTs and proposed a surface mechanism for storing Li species on the bare surface of CNTs and carbon nanoparticles. Because the CNTs investigated were end-capped and no other treatments were applied, the Li adsorbed was only discovered on the CNT surfaces [27]. Senani et al. [28] used ab initio quantum chemical computations to investigate the adsorption of Li-ions on the surface of (12,0) SWCNTs. The adsorption of a single Li-ion on the inside of SWCNTs is favored compared to the outside, as the Li adsorption energy is −0.98 eV on the inside and −0.86 eV on the outside. They also demonstrated that, following Li attachment, charge is transferred from Li-ions to CNTs, and the bonds between Li atoms and CNTs have ionic characteristics. They hypothesized that the amount of charge transfer should be proportional to the radii of curvature of CNT. Klink et al. presented a morphology modification method for gas-phase oxidation of CNTs that introduces more surface functional groups than liquid oxidation procedures [32]. MWCNTs were oxidized for varying amounts of time with liquid or gas-phase nitric acid. Gas-phase oxidized CNTs (*g*-CNT) have a substantially lower initial charge loss (172 mAh/g) than liquid-phase oxidized CNTs (*l*-CNT) (283 mAh/g) (Figure 2a,b). This is because exfoliation is less prominent in the former case, which is most likely due to an increase in surface carbonyl groups. As a result, gas-phase oxidized CNTs are thought to be better suited for battery-related applications because they have a lower specific initial charge loss, are easier to produce, and exhibit less mechanical degradation.

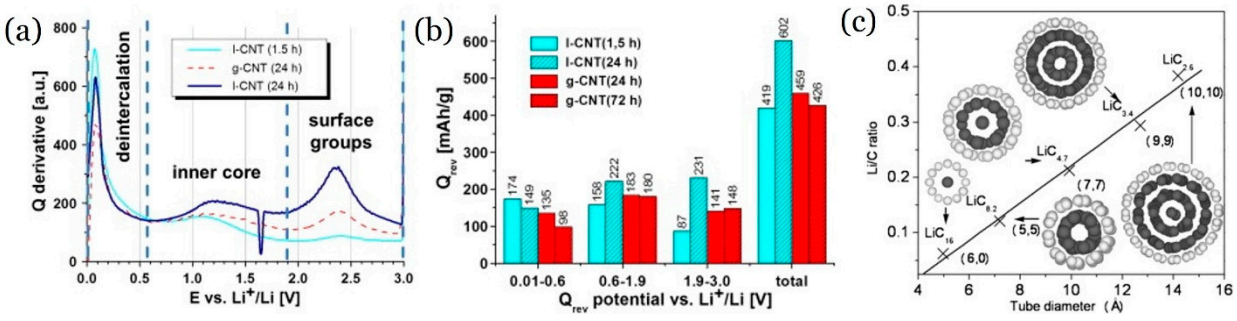

Figure 2. (**a**,**b**): g-CNT and l-CNT. (**a**) Derivative of 1st cycle reversible capacity; (**b**) reversible capacity of g-CNT and l-CNT, divided into three potential areas of Gr layer deintercalation (0.01–0.6 V), inner core de-insertion (0.6–1.9 V) and extraction from functional groups (1.9–3.0 V); ~0.5 mg/cm^2, 1 M LiPF6 in 1:1 EC:DEC, 50 mAh/g. Adapted with permission from ref. [32]. Copyright © 2011 Elsevier B.V. (**c**) Li/C ratio vs. tube diameter. Insets illustrate the equilibrium configurations of SWNTs packed with Li atoms. White and grey balls: carbon and Li atoms, respectively. Adapted with permission from ref. [33]. Copyright © 2005 Elsevier B.V.

First-principles computations have demonstrated that Li trapped inside SWNTs has significant mobility along/around the axial direction, while radial motion is restricted.

A clear link between the Li/C ratio and tube diameter was found. As the tube diameter increases, the intercalated Li atoms tend to form a multi-shell structure (Figure 2c) at equilibrium, formed of coaxial tubes with a linear chain in the axis, which improves Li capacity [33]. Li et al. have experimentally studied the Li insertion/extraction properties of nanocarbon material anodes, including SWNTs, MWNTs, C_{60}@SWNTs (C_{60}-peapod), graphite nanoflakes, and graphite nanoparticles containing some MWNTs [34]. According to the galvanostatic charge–discharge experiment, the Li storage capacity, coulombic efficiency, and cyclability of nanocarbon materials are highly influenced by their subtle architectures and subsequent treatments. Cyclic voltammetry demonstrated that Li oxidation potentials rise with the length in the Li reversible insertion/extraction route. Raman spectroscopy revealed a mechanism of Li insertion/extraction in SWNT and C_{60}-peapod electrodes, indicating that Li can enter the inner space of the tubes, the bundle's trigonal interstitial channels, and the intercalation site between nearby tubes, with the trigonal interstitial channels being the dominant reversible sites for Li storage.

Being 1D carbon nanostructures, carbon nanofibers (CNFs) and carbon nanorods (CNRs) have similar physical characteristics to CNTs. CNFs have a small diameter and excellent conductivity, enabling efficient charge transport of both Li-ions from the electrolyte and electrons from the current collector. Furthermore, because these composite nanofibers create free-standing, flexible, and electrically conductive mats that may be employed directly as binder-free electrodes, no binders or additives are required during the battery manufacturing process [35]. Therefore, CNFs have been developed as anode materials in Li-ion batteries due to their high surface area, compact structure, and numerous pores. Such features are ideal for huge volumes of Li-ion diffusions [36]. Numerous studies have supported and published 1D carbon-based nanostructure composites as anode materials for Li-ion batteries. Recent research has focused on CNT-based anodes for LIBs, with varied degrees of efficacy depending on the treatments used.

There have been several reports of 1D nanostructured carbon composites containing metalloid elements and post-transition metals: Si-CNT [37], Ge-CNF [38], Sn nanoparticles/CNT [39]. SnO_2 nanocrystals/MWCNT [40], Si/C@CNF [41], SiO nanoparticles/CNT [42], Si@C–SiO_2 [43], Sn/CNF, Si/CNF, Ge/CNF [38,44], Sn/SnO_2@CNF [45], and SnO_2@CNF [46]. Further, 1D nanostructured carbon-metal oxides composites also have been reported: Fe_2O_3 nanorods/CNFs [47], GeO_2/multichannel CNF [48], Co_3O_4 nanoparticles/MWCNT [49], porous $FeCO_3$/CNF [50], Zn_2SnO_4 nanoparticles/CNT [51], TiO_2 coated SnZnO/CNF [52], $FeCO_3$ NRs/CNT [53], $MgFe_2O_4$/CNF [54], Mn_3O_4 nanoparticles/CNT [55], Fe_3O_4 nanoparticles/CNF [56], MnO_2/CNF [57], MnO_2@CNT fabric [58], $NiCo_2O_4$ nanoparticles/CNT [59], and MnO/CNF free-standing fabric [60]. CNTs can be employed as a support matrix to create CNT/metal composites that take advantage of metals' higher capacities [61,62]. This strategy has many advantages: it permits an anode to benefit from the high Li capacity without the issue of pulverization. When metal nanoparticles abruptly alloy with Li and grow in size, an anode can remain intact in its structure because the CNT works as a flexible network, keeping the metal nanoparticles linked to the anode current collector. When metal nanoparticles alloy and dealloy, the CNTs can transport electrons to and from them. Furthermore, CNTs can store any additional Li that has not been alloyed with metallic nanoparticles [24].

Si, with a theoretical capacity of ~4200 mAh/g, has long been recognized as an appealing material for anodes in energy storage systems. However, the structural deterioration and instability of the SEI, as well as the low electrical conductivity, hampered commercialization. The volume expansion and poor conductivity can be remedied using CNTs. Zhu et al. used modified CVD to produce a neuron-like Si-CNT composite electrode (Figure 3a–c) [37]. The neuron-like Si-CNT composite not only contributed to the Si anode's excellent electronic conductivity and mechanical stability, but it also efficiently compensated for the Si particles' substantial volume change. When compared to the physical Si + CNT mixture, the Si anode's rate capability and cycling stability are greatly improved. The neuron-like Si-CNT composite nonetheless delivered a reversible capacity

of 1161.5 mAh/g at a high current density of 20 A/g. After 200 cycles, capacity retention reached 96% (Figure 3b). The electronic conductivity of the Si + CNT mixed electrode laminate was 0.81 S/cm, compared to approximately 0.52 S/cm for the bare Si electrode. The conductivity of the as-prepared neuron-like Si-CNT composite electrode was 0.95 S/cm (Figure 3c).

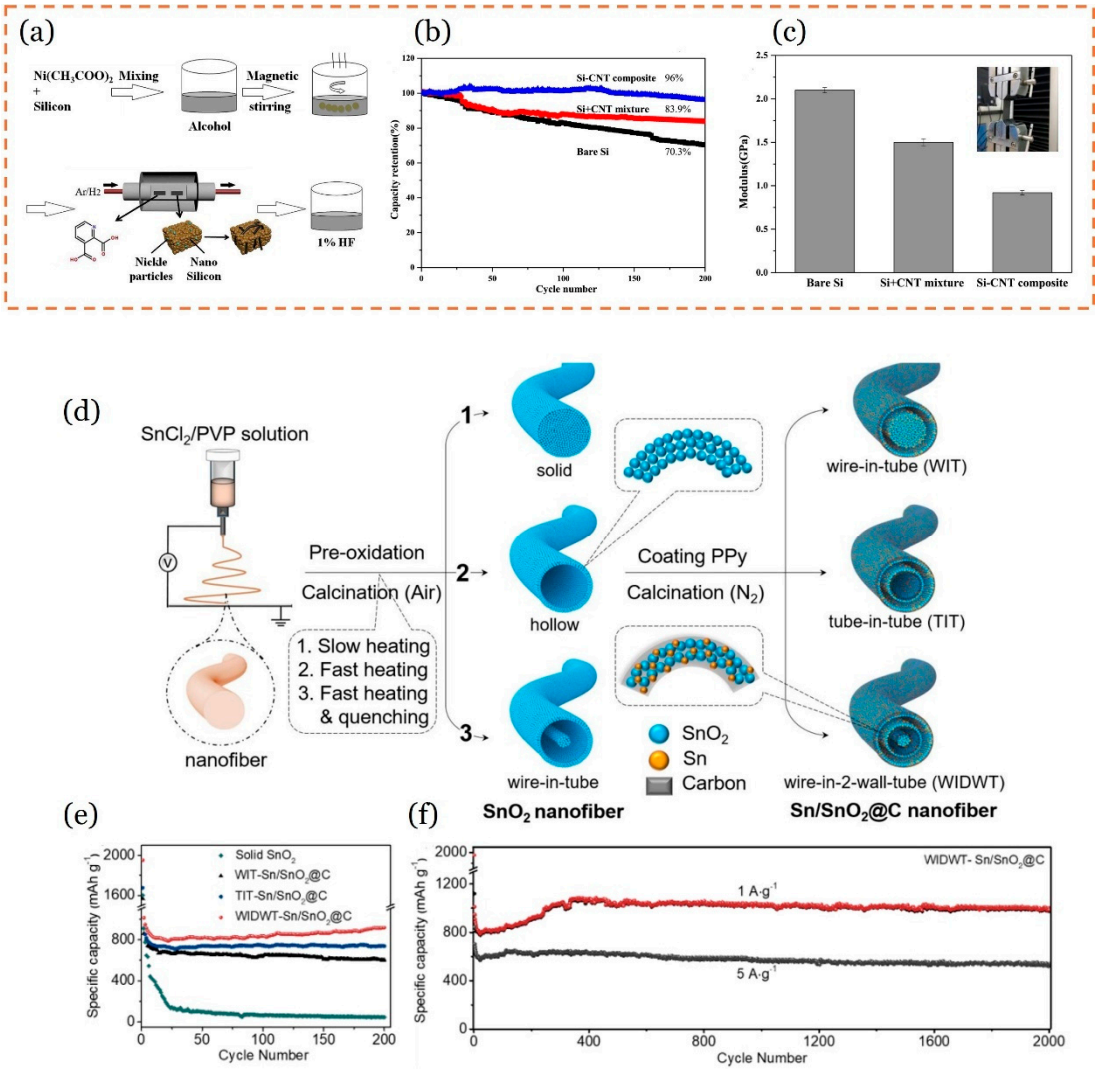

Figure 3. (**a**–**c**): Neuron-like Si-CNT composite. (**a**) The preparation approach of the neuron-like Si-CNT composite using a modified CVD method; (**b**) the electrochemical properties of different Si electrodes: rate capability; (**c**) the physical property of different Si electrodes: electronic conductivity. Adapted with permission from ref. [37]. Copyright © 2019 Elsevier B.V. (**d**–**f**): Multi-wall Sn/SnO_2@Carbon hollow NFs. (**d**) Fabrication scheme of multi-wall Sn/SnO_2@C hollow NFs. The Sn precursor nanofibers are first created using electrospinning. Solid, hollow, and WIT structured SnO_2 nanofibers are produced from the same precursor by varying the heating rate during calcination. Then polypyrrole (PPy) is in situ polymerized onto outer and inner surfaces of the above three kinds of SnO_2 NF. After calcinating the PPy/SnO_2 composite nanofibers in N_2, Ppy turns to carbon, which partially reduces SnO_2 to metal Sn. As a result, WIT, TIT, and WIDWT Sn/SnO_2@C composite NFs are prepared. (**e**) Cycling performance for 200 cycles (at 1 A/g rate). (**f**) Long cycling performance of the WIDWT Sn/SnO_2@C at a current rate of 1 A/g and 5 A/g for 2000 cycles. Adapted with permission from ref. [63]. © 2019 Wiley-VCH Verlag GmbH & Co. KGaA, Weinheim.

Emerging nanostructure such as Si nanowire has been shown to be capable of repeated discharges of >3000 mAh/g [64]. The nanowires resist anode crumbling because their

small width reduces the effect of volume expansion, allowing them to expand and contract without breaking. A paper-like ultrathin and flexible Si/CNT composite anode for LIBs was created via conformal electrodeposition of a thin layer of Si on CNTs at room temperature (RT) [65]. The flexible Si/CNT composite had a high volumetric capacity (~1400 mAh/cm^3 at 200 mA/g) due to its active material and current collector. Furthermore, prelithiation treatment can effectively increase the Si/CNT composites' low initial coulombic efficiency, and a red LED can be easily lit by a full pouch cell with a Si/CNT composite as a flexible anode in flat or bent states. Similarly, carbon-coated Si nanoparticles (30–100 nm in diameter) dispersed in CNT (6–13 nm in diameter, 2.5–20 µm in length) networks were tested as an anode material for LIBs. This material showed a capacity retention of 70% after 40 cycles [66]. The carbon layer in Si@C-CNT improved electrical conductivity while allowing for volume variations. The CNT network strengthened the electrode, stabilized the electric network for active Si, and improved cycle performance. In contrast, without the CNT network, the Si@C anode developed cracks, pulverization, and disintegration due to volume expansion.

A chemical reduction approach was used to develop a Sn/carbon nanotube (CNT) composite anode material for LIB [39]. The Sn/CNT composite displayed consistent cycling performance with a reversible capacity of 413 mAh/g at the 100th cycle and a high initial reversible capacity of 630.5 mAh/g. The increased electrochemical performance of the Sn/CNT composite might be due mostly to the excellent dispersion of Sn nanoparticles on CNTs and the partial filling of Sn nanoparticles within the CNTs. It was proposed that chemical treatment of CNTs with concentrated nitric acid, which cuts CNTs into small fragments and increases the number of oxygen-functional groups on the surface, serves an important role in positioning Sn nanoparticles on CNTs and preventing Sn nanoparticle clustering during the charge-discharge process.

Sn-based oxide materials, such as SnO_2, with high theoretical reversible specific capacity (e.g., 781 mA h/g), have been widely studied as prospective alternatives for graphitic anode materials (theoretical capacity: 372 mA h/g). However, the main disadvantage of its industrial application is poor cycle performance, which stems from the significant specific volume change caused by repetitive charging and discharging of the battery, resulting in mechanical failure and loss of electrical contact at the anode [46,67]. To improve cycle performance, anodic capacity, and rate capacity, SnO_2 anode materials must be morphologically and structurally modified. The introduction of carbon components into SnO_2@C composites is an effective technique for improving their electrochemical performance.

Electrospinning was used to fabricate SnO_2@C nanofibers (NFs), which were then tested as anodes in LIB half cells. The NF anodes had initial discharge capacities of 1375.5 mAh/g at 80 mA/g current density [46]. This high Li-ion storage capability of SnO_2 NFs is most likely due to the amorphous carbon protection and the synergy created by the ultrafine SnO_2 particles implanted in the CNF matrix. The nanometer-sized SnO_2@C NFs can not only provide minimal ion diffusion durations, resulting in faster phase transitions, but also ample room to buffer volume changes during the Li insertion and extraction process.

Gao et al. developed a method for producing designable and well-controllable multiwall Sn/SnO_2@C hollow nanofibers: wire-in-tube (WIT), tube-in-tube (TIT), and wire-in-double-wall-tube (WIDWT) nanofibers (Figure 3d) [63]. WIDWT nanofibers can increase the contact area between the electrolyte and electrode while also providing active areas for redox processes. Throughout the charging and discharging process, the twin tube inner layers provide a suitable but not excessive gap between the core and shells, thus reducing volume expansion and guaranteeing favorable transport kinetics for both Li-ions and electrons (Figure 3d). The Sn/SnO_2@C composite outperforms bare SnO_2 in terms of electrochemical performance (Figure 3e,f). The collaboration of multi-structure and composition optimization contributes to the great rate capability (812.1 mAh/g at 1 A/g and 566.5 mAh/g at 5 A/g) and better cycling performance (986.3 mAh/g at a current of 1 A/g and 508.2 mAh/g at 5 A/g after 2000 cycles).

As stated previously, Si has the highest theoretical capacity (4200 mAh/g), but its volume changes by 400% during the anode operation [68]. Ge has a lesser theoretical capacity of 1600 mAh/g, and its volume change is reduced to 370% [69]. Sn has the lowest theoretical capacity of 990 mAh/g, with a volume change of only 259% during the alloying process [70]. In order to enhance electrode conductivity—which is progressively lost owing to the significant volume change—and enable strain relaxation, nanocomposites of Si, Ge, and Sn containing confinement materials (such CNFs) have been produced. They have shown promising specific capacities and cyclability for use in LIBs [71,72]. Electrospinning and carbonization were used to create Si/C, Ge/C, and Sn/C composite nanofibers with varying nanoparticle content [38]. The resulting composite nanofibers were employed as anodes in Li-ion half cells, where they demonstrated reasonably high reversible capacities and good cycle performance. CNFs have a small diameter and high conductivity, allowing for effective charge transport of Li-ions from the electrolyte and electrons from the current collector. When Si/C, Ge/C, and Sn/C composite anodes were compared, Si/C nanofibers had the largest initial coulombic efficiency due to the minor effect of SEI. Nevertheless, Ge/C and Sn/C anodes excelled compared to Si/C anodes in terms of cycle performance, especially at higher filler concentrations, owing to superior nanoparticle distribution in carbon nanofibers and a lesser volume change during the Li insertion and extraction processes.

Because of its high theoretical capacity, adequate lithiation potential, low cost, and ecologically friendly nature, Mn_3O_4 is regarded as a promising LIB anode material [55]. However, the low electronic conductivity and rapid volume increase during cycling make improving Li-ion storage qualities difficult. Mn_3O_4 nanoparticles (~18 nm) anchoring on CNTs (CNTs@Mn_3O_4) are created by employing CNTs@MnO_2 as a precursor, which is made in a simple room-temperature technique. Taking advantage of the features provided by the microstructure and hybrid material components, the as-prepared CNTs@Mn_3O_4 electrode has a reversible capacity of 895.0 mAh/g at 0.5 A/g after 200 cycles and 743.7 mAh/g at 5.0 A/g when utilized as a LIBs anode [55].

Cyclic voltammetry (CV) is a popular technique for studying the oxidation, reduction, and phase transformation processes in electrode reactions. The electrochemical performance of the CNTs@Mn_3O_4 was assessed using CV at a scan rate of 0.25 mV/s as a LIB anode (Figure 4a). The first lithiation step generates two separate cathodic peaks. The cathodic peak at ~0.15 V is related with the reduction of Mn_3O_4 into Mn metal nanoparticles, whereas the left peaks at ~0.05 V are attributed to CNT lithiation. Three peaks at around 0.20, 1.25, and 2.10 V were seen during the anodic process, corresponding to CNT delithiation, Mn metal oxidation into Mn_3O_4, and higher valence Mn oxides. In subsequent cycles, the reduction potential of Mn_3O_4 changes to 0.30 V, and the voltage hysteresis between the reduction and oxidation processes decreases, implying that the kinetics of the electrochemical reaction improve after the first lithiation–delithiation event. Figure 4b shows the rate capability of the CNTs@Mn_3O_4 electrode.

Because of their high capacity, low cost, and natural availability, $FeCO_3$ nanomaterials have been extensively researched as anode materials for LIBs. Nonetheless, the sluggish diffusion of Li-ions in bulk materials and their low electronic conductivity limit $FeCO_3$'s power performance. The $FeCO_3$/carbon nanotube composites ($FeCO_3$/CNTs) were created employing CNTs, ferrous sulfate, and urea as raw ingredients in a single-step in situ crystallization method. The inclusion of modest CNTs can significantly improve the electrochemical performance of $FeCO_3$. At a current density of 200 mA/g, $FeCO_3$/CNT-15 ($FeCO_3$/CNT-*x*, where *x* is wt%) has an initial discharge capacity of 1436 mAh/g and retains a capacity of 694 mAh/g after 140 cycles [53]. Figure 4c shows plots of discharge–charge capacities against cycle number for voltages ranging from 0.05 to 3 V and current densities of 200 mA/g. The as-prepared $FeCO_3$ and $FeCO_3$/CNT composites can achieve an initial discharge capacity of more than 1400 mAh/g. The generation of SEI films and electrolyte deterioration are the primary causes of the first capacity reduction. The capacities decreased during the first twenty cycles, but subsequently stabilized at 451, 560, 550, 694, and

481 mAh/g for $FeCO_3$, $FeCO_3$/CNT-5, $FeCO_3$/CNT-10, $FeCO_3$/CNT-15, and $FeCO_3$/CNT-20, respectively, throughout the next 140 cycles. $FeCO_3$/CNT-15 demonstrated the best electrochemical performances. After 10 cycles, the coulombic efficiency of $FeCO_3$/CNT-15 approached 100%, and the maximal reversible capacity of 694 mAh/g was maintained even after 140 cycles. The structure of $FeCO_3$/CNT-15 after 140 cycles stayed almost identical to that of $FeCO_3$/CNT-15 prior to the cycling stability test [53].

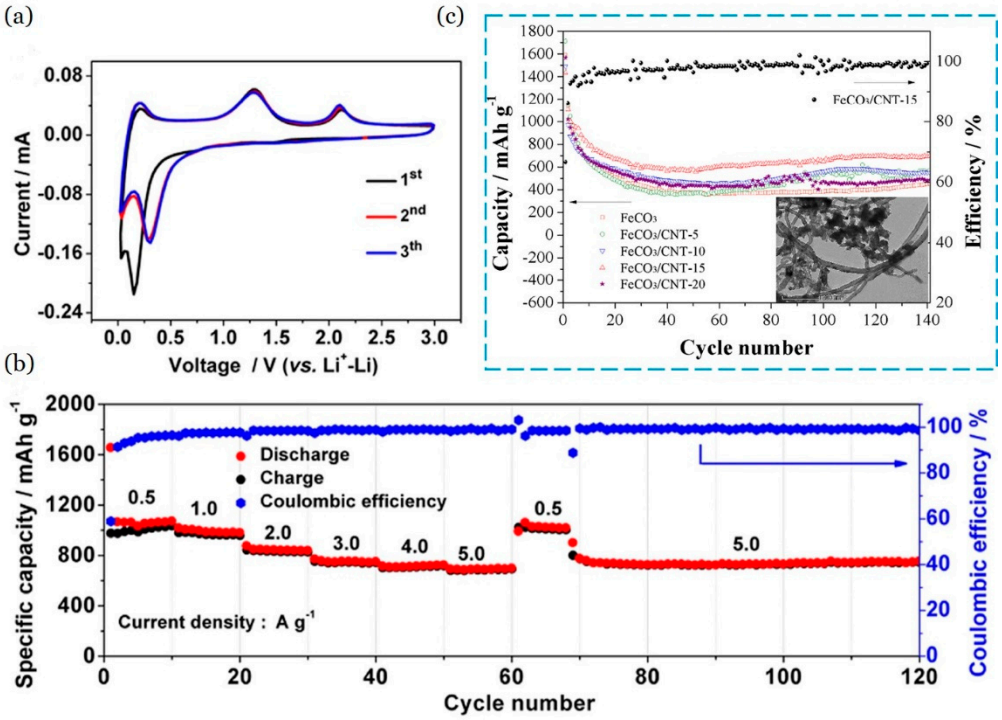

Figure 4. (**a**,**b**): CNTs@Mn_3O_4 electrode. (**a**) CV curves of the as-prepared CNTs@Mn_3O_4 electrode; (**b**) rate capability of CNTs@Mn_3O_4 electrode. Adapted with permission from ref. [55]. © 2020 Elsevier B.V. (**c**) $FeCO_3$/CNTs. Cycling stability of electrodes using $FeCO_3$, $FeCO_3$/CNT-5, $FeCO_3$/CNT-10, $FeCO_3$/CNT-15, and $FeCO_3$/CNT-20 (inset shows the morphology of $FeCO_3$/CNT-15 after 140 cycles). Adapted with permission from ref. [53]. © 2018 Elsevier B.V.

Transitional metal oxides have been observed as suitable anode materials for LIBs [73]. The spinel $NiCo_2O_4$ (NCO) has a theoretical capacity of 890 mAh/g and a two-fold higher electronic conductivity than nickel oxides or cobalt oxides [74]. However, NCO has limited cyclability and rate capability because of its slow electron/ion transport rates and significant volume expansion/contraction during the charging–discharging process [75], restricting its potential usage in high-energy storage systems. To solve this issue, by lowering the size of nanoparticles and building hybrid nanostructures of NCO and a carbon matrix, one may achieve good electrochemical performance due to the shorter ion or electronic diffusion path [76]. Microwaves have attracted a lot of attention in a variety of fields, including microwave-absorbing applications [77], thermoelectric applications [78], and supercapacitors [79], because of their ability to shorten reaction times, increase yields, and allow for the fabrication of nanostructures with smaller and more uniform sizes, which results in improved performance.

Zhang et al. used a novel and rapid microwave-assisted approach to successfully fabricate porous $NiCo_2O_4$@CNTs 1D structure nanocomposites [59]. The hybrid material was composed of ultrafine $NiCo_2O_4$ nanoparticles measuring 6–10 nm that were securely anchored on the surface of CNTs. When compared to pristine $NiCo_2O_4$, the $NiCo_2O_4$@CNTs composite material demonstrated more intriguing electrochemical properties, such as a greater specific capacity, an excellent current charge–discharge capacity, and improved cycle stability. As a negative electrode for LIBs, a flexible carbon electrode was developed

by impregnating magnetite nanoparticles (Fe_3O_4-NPs, ~32 nm) on electrospun CNFs [56]. The Fe_3O_4-NPs particles were found to be well adsorbed on 400 nm CNFs. The addition of Fe_3O_4-NPs increased the electrochemical performance of the CNFs, resulting in an initial high discharge capacity of 1146 mAh/g—higher than that of pure CNFs (480 mAh/g). The composite active material also demonstrated a higher coulombic efficiency (90%). However, because of the reduced electrical conductivity of Fe_3O_4-NPs, the composite showed a modest drop in capacity retention at high C rates.

Using a combination of hyper-crosslinking, liquid phase oxidation, and a hydrothermal (HT) technique, three types of carboxyl modification tubular CFs (CMTCFs) and MnO_2 composite materials (CMTCFs/MnO_2) were created [57]. The HT reaction period was adjusted (6, 8, and 12 h) to control the morphology and crystal phase of MnO_2 in CMTCFs/MnO_2. CMTCFs wrapped in δ-MnO_2 nanosheets (CMTCFs@MNS) were employed as anodes and compared to the other two CMTCFs/MnO_2. According to electrochemical study, the CMTCFs@MNS (which underwent a 6 h HT treatment) electrode has a large reversible capacity of 1497.1 mAh/g after 300 cycles at 1000 mA/g and a long cycling reversible capacity of 400.8 mAh/g after 1000 cycles at 10,000 mA/g. At the same time, following twelve modifications in current density, CMTCFs@MNS exhibits an avg. reversible capacity of 256.32 mAh/g at 10,000 mA/g.

Tzeng et al. improved anode cycling performance by partially encapsulating Si flakes in silicon dioxide and covering them with conductive nanocarbon sheets and CNTs [80]. A silicon dioxide surface layer on a Si flake improves the physical integrity of a Si-based anode. The exposed Si surface facilitates the quick passage of Li-ions and electrons. CNTs and nanocarbon sheets operate as electrical contacts between the Si flakes and the current collector [80].

In carbonaceous materials, heteroatom doping (donor or acceptor atoms) is useful for controlling the active site, ion transport, and electronic transfer for electrochemical energy storage [81–84]. N and B doping in carbon can result in increased conductivity and pseudocapacitance [85–87]. Further, due to their comparable atomic radii, both B and N atoms are capable of reaching a high doping concentration. A composite, $Li_4Ti_5O_{12}$ (LTO)/MWCNT-co-doped with nitrogen (N) and boron (B), has shown a reversible capacity of 120 mAh/g at a rate of 20 C [88]. After 150 cycles at 20 °C, 97.5% of the capacity was preserved, with minimal capacity fading. The co-doped CNTs' improved electrochemical performance compared to LTO could be attributed to the separate forms of N and B. This not only maintained the benefits of the N and B additives, such as good electron-donating and electron-accepting capabilities, but also resulted in a synergistic effect due to their unique electronic structure [89]. To obtain the composite, a mixture of N, B-CNT, and LTO was calcinated.

Transition-metal sulfides (TMSs) involving conversion and/or alloying reactions are regarded as promising anode materials for advanced LIBs and sodium-ion batteries (SIBs) [90]. However, the poor electronic conductivity and significant volume expansion severely limit their practical application. Hou et al. proposed a covalent coupling technique for TMS-based anode materials that employs amide linkages to bind TMSs and carbon nanotubes (CNTs) [90]. During the synthesis, thiourea serves as both the capping agent for morphological control and the linking agent for covalent coupling. In this covalently coupled ZnS/CNT composite, the ZnS nanoparticles (∼10 nm) securely anchored to CNT bundles. The compact ZnS-CNT heterojunctions are highly beneficial for promoting electron/ion transmission and maintaining structural integrity. Because of the strong coupling interaction between ZnS and CNTs, the composite exhibits prominent pseudocapacitive behavior and highly reversible electrochemical processes, resulting in reversible capacities of 333 mAh/g at 2 A/g over 4000 cycles for LIBs and 314 mAh/g at 5 A/g after 500 cycles for SIBs.

3. Two-Dimensional (2D) Carbon Nanostructure (GO and Gr) Composites

Because of their unique structures, 2D carbon nanomaterials have attracted a lot of attention for use in flexible LIBs due to their large specific surface area, excellent charge mobilities, inherent flexibility, and high Li storage capacity.

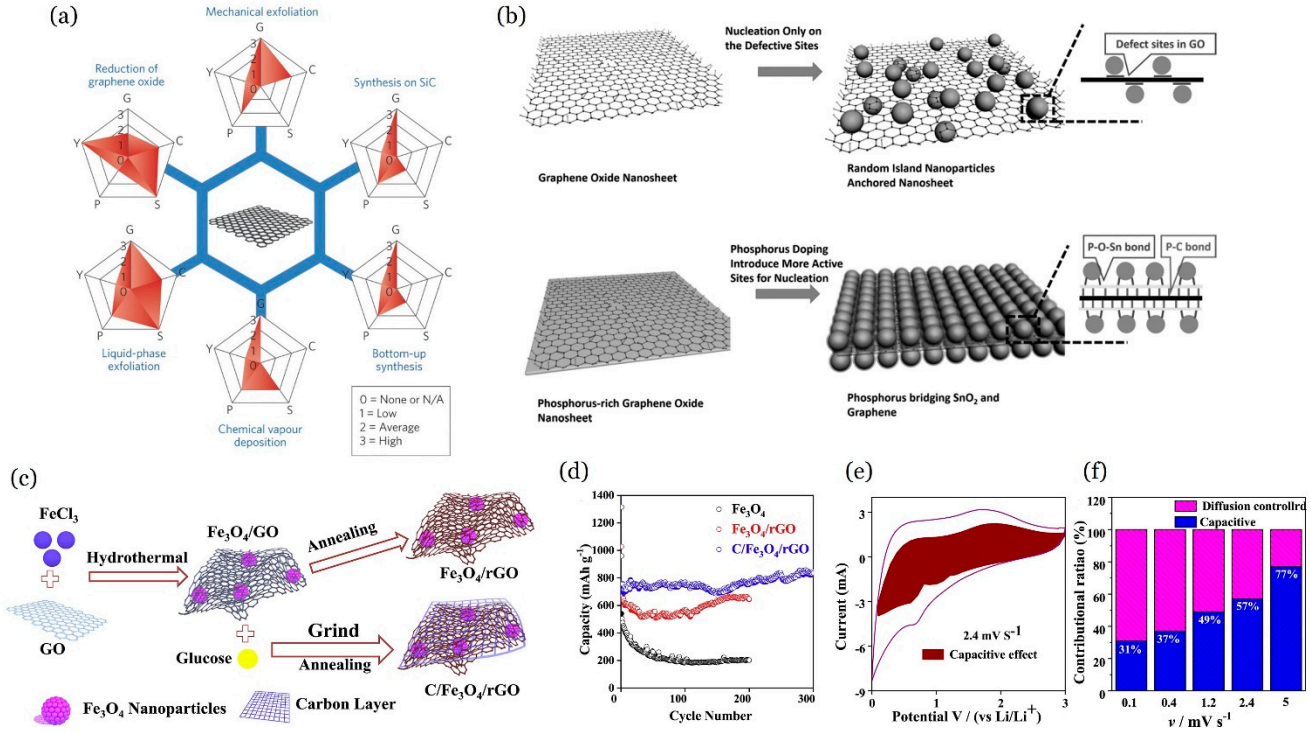

Figure 5. (**a**) Schematic of the most common Gr production methods. Each method has been evaluated in terms of Gr quality (G), cost aspect (C; a low value corresponds to high cost of production), scalability (S), purity (P), and yield (Y) of the overall production process [91]. (**b**) Phosphorus covalently crosslinked SnO_2 and Gr. Illustrations of formation process of SnO_2/GO and SnO_2@P@GO.Adapted with permission from ref. [92]. © 2017 WILEY-VCH Verlag GmbH & Co. KGaA, Weinheim. (**c**–**f**): Carbon layer encapsulated Fe_3O_4@rGO. (**c**) Schematic diagram of the Fe_3O_4/rGO and C/Fe_3O_4/rGO composites; (**d**) cyclic performance at 0.2 A/g of the Fe_3O_4, Fe_3O_4/rGO and C/Fe_3O_4/rGO electrode; (**e**) CV curves with capacitive contribution at 2.4 mV/s; and (**f**) separation of contributions from capacitive effects and diffusion controlled capacities at different scan rates. Adapted with permission from ref. [93]. © 2020 Elsevier Ltd. and Techna Group S.r.l.

Graphene (Gr), which has atoms organized in two dimensions to form a sheet structure, has robust mechanical flexibility, its surface area is large, its chemical stability is outstanding, and its electrical conductivity is excellent [94]. However, its coulombic efficiency is low. It is proposed that Gr's double atomic surfaces allow it to store more Li atoms than graphite. The interaction between Li and Gr is facilitated by charge transfer and the van der Waals (vdW) effect. The coulombic interaction is governed by charge transfer and is thus mostly determined by the electronic structure. As a result, the coulomb interaction in Gr is similar to graphite's. With the vdW effect, Li adsorption on Gr is somewhat weaker than in graphite. Introducing vacancies, pores, or defects on Gr enhances the adsorption of Li, leading to an increase in capacity [95]. Additionally, Gr has derivatives that include graphene oxide (GO) and reduced graphene oxide (rGO), both of which include different kinds of oxygen functional groups. GO and rGO are particularly useful for wrapping and dispersing nanoparticles, reducing volume strain, and facilitating Li storage and electron transport. Figure 5a depicts a wide range of ways used to produce Gr [91]. Gr may be built into a 2D thin film using vacuum filtering and a 3D network using solvothermal/CVD techniques to create suitable supporting

substrates for the direct development of active cathode materials. This presents numerous prospects for Gr and Gr derivatives to develop binder-free nanostructured electrodes with high reversible capacity in LIBs. To maximize the performance of Gr as an anode material for Li-ion batteries, Gr composites with supporting material are preferable to Gr as a single component. The quantity of ions per gram of material controls the battery's capacity, and consequently its energy. Gr, like graphite, can be utilized as an anode for hosting Li^+ as a carbonaceous matrix in composites with other Li-storing materials. Numerous studies on Gr-based materials for electrochemical energy storage have been conducted in the last few years [96]. Several Gr composites with post-transition-metal oxide and phosphor have been found in a series of studies in the literature: SnO_2/Gr [97], 3D SnO_2/rGO [98], carbon-coated SnO_2/rGO foam [99], cobalt-doped SnO_2/Gr sheets (Co-SnO_2@GS) [100], MOF/SnO_2/Gr [101], rGO/Fe_2O_3/SnO_2 ternary nanocomposite [102], SnO_2/$NiFe_2O_4$/Gr [103], and SnO_2@P@rGO [92]. Further, Gr/transition-metal oxide composites have also been reported: Gr anchored with Co_3O_4 nanoparticles [104], CuO/Gr [105], MnO/Gr [106], Zn_2GeO_4 nanorod/Gr composites [107], CoO-rGO [108], hollow 3D mesoporous $CoFe_2O_4$ NSs/Gr [109], core shell structured $ZnFe_2O_4$@C/G nanocomposite [110], CNF/MnO/rGO thin film [111], nanocubic $CoFe_2O_4$/Gr [112], Mn_3O_4/rGO [113], hollow α-Fe_2O_3 nanotube-Gr [114], C/Fe_3O_4/rGO [93], hollow Co_3O_4 nanoparticles/porous rGO [115], CoO NW@Gr cloth [116], $ZnFe_2O_4$/rGO [117], porous α-Fe_2O_3 nanoparticles/Gr [118], hierarchical nanospheres Fe_2O_3/Gr [119], TiO_2 nanotubes/rGO [120], and self-supporting Co_3O_4/Gr films [121].

Metal oxide/Gr composite material structures can be generally classified into the following models: widely employed anchored type (SnO_2 [122], Fe_2O_3 [123]), wrapped (Fe_3O_4 [124], MoO_2 [125]) encapsulated (Fe_3O_4 [126], Fe_2O_3 [127]) sandwich-like (TiO_2 [128]) layered stacking (SnO_2–NiO–MnO_2 [129], MnO_2 [130]), and mixed ($Li_4Ti_5O_{12}$ [131], Fe_2O_3 [132]) (Figure 6).

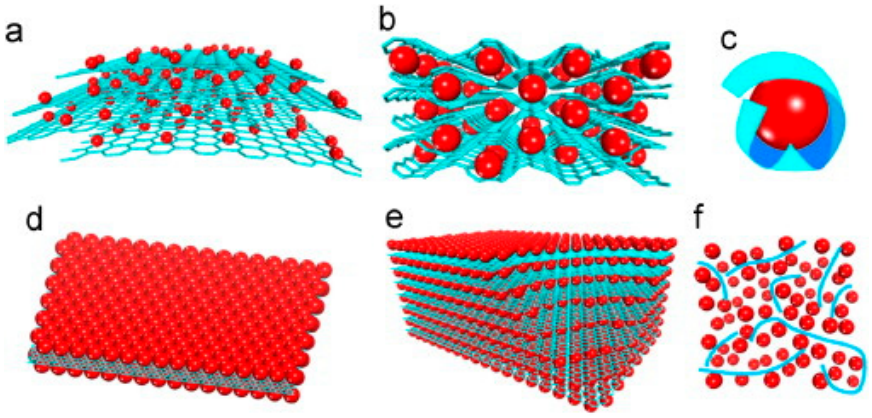

Figure 6. Schematic of structural models of Gr/metal oxide composites: (**a**) Anchored model: nanosized oxide particles are anchored on the surface of Gr. (**b**) Wrapped model: metal oxide particles are wrapped by Gr. (**c**) Encapsulated model: oxide particles are encapsulated by Gr. (**d**) Sandwich-like model: Gr serves as a template for the creation of a metal oxide/Gr/metal oxide sandwich-like structure. (**e**) Layered model: a structure composed of alternating layers of metal oxide nanoparticles and Gr. (**f**) Mixed model: Gr and metal oxide particles are mechanically mixed and Gr forms a conductive network among the metal oxide particles. Red: metal oxide particles; blue: Gr sheets [133].

Table 1 summarizes the performance of 2D carbon nanostructure composites as LIB anodes mentioned in the literature.

Glucose was utilized as a crosslinking agent in the HT process to improve the bond between SnO_2 and rGO. The authors developed a carbon-coated SnO_2/rGO (SnO_2/rGO/C) foam by constructing a 3D foam structure of distributed SnO_2 nanoparticles on rGO sheets and covering it with a thin layer of amorphous carbon using a HT approach and then freeze

drying [99]. The carbon layer may aid in the binding of active SnO_2 nanoparticles to rGO sheets, increasing the composite's electrical conductivity. The electronic conductivity of the SnO_2/rGO/C foam was found to be 2.44 S/cm, which is significantly greater than that of the SnO_2/rGO foam (0.24 S/cm) without the carbon layer. The rGO and carbon layer collaborate to successfully preserve the structural arrangement's stability, preventing SnO_2 detachment from the rGO substrate. The as-prepared SnO_2/rGO/C film electrode outperforms SnO_2/rGO and bare SnO_2 as anode materials for LIBs in terms of specific capacity, rate performance, and cycling performance due to its 3D porous nanostructure and excellent mechanical flexibility. This outstanding performance is due to the synergistic action of SnO_2, rGO, and the carbon layer. As a free-standing anode for LIBs, the foam demonstrated high capacity and outstanding cycling stability (717 mAh/g after 130 cycles at 100 mA/g).

Table 1. The electrochemical performance of 2D nanocarbon-based anodes documented in the literature. Abbreviations: Gr = graphene; HT = hydrothermal.

Composites	Synthesis Method	1st Discharge–Charge Capacity (mAh/g)	Current Density (mA/g)	Cycling Performance (mAh/g): Capacity Retention (Number of Cycles)	Current-Density Applied (mA/g)	Reference
Zn_2GeO_4 Nanorod/Gr	HT	1508/1020	200	768 (50)	200	[107]
CuO/Gr composite	solution method	900	65	600 (100)	65	[105]
SnO_2/Gr	Chemical method	1719/852	100	634 (50)	100	[97]
Co_3O_4 nanoparticles@Gr	Solution phase dispersion	1097/753	50	935 (30)	50	[104]
Gr/Fe_2O_3/SnO_2	In situ precipitation followed by reduction	1179/746	168	700 (100)	400	[102]
SnO_2/Gr	In situ reduction, spray drying, thermal treatment	1542/837	500	704 (150)	500	[98]
3D C-Coated SnO_2/rGO foam	One-pot HT method	2544/960	100	717 (130)	100	[99]
SnO_2@P@GO	Solvothermal	1278/405	100	550 (200)	1000	[92]
3D CoO–Gr hydrogel	HT	1230/984	100	1010 (100)	100	[108]
CNF/MnO/rGO thin free-standing binder-free film	Electrospinning, Electrospraying	1582/1107	100	574 (3000)	5000	[111]
Hexagonal Mn_3O_4@RGO	Chemical reduction	1086/884	—	638 (250	123	[113]
3D sandwich-like C/Fe_3O_4/rGO	Solvothermal	1315/721	200	832 (300)	200	[93]
Hollow-Co_3O_4/Porous-rGO	Facile etching strategy and the Kirkendall effect	1164/813	200	1016 (200)	200	[115]
$ZnFe_2O_4$ nanoparticle/rGO	Metal reduction	1939/1285	1000	1022 (500)	1000	[117]

Table 1. *Cont.*

Composites	Synthesis Method	1st Discharge–Charge Capacity (mAh/g)	Current Density (mA/g)	Cycling Performance (mAh/g): Capacity Retention (Number of Cycles)	Current-Density Applied (mA/g)	Reference
$Cu_2Sn_3S_7/Cu_2SnS_3/SnS_2$/rGO	Liquid phase	1043/859	500	965 (300)	500	[134]
Mesoporous Fe_2O_3/N-doped Gr	HT	1426/1143	0.1 C	905 (250)	1 C	[135]
SnO_2/G coated with polyacrylic acid	In situ polymerization, In situ carbonization	1652/987	100	480 (500)	1000	[136]
Co-doped SnO_2 and Gr sheets	Hydrolysis	2102/1280	100	828 (200)	500	[100]
Cuboid particles MOF/SnO_2/Gr	Solvothermal	1332/660	100	450 (1000)	1000	[101]
$SnO_2/NiFe_2O_4$/Gr	HT	1465/905	200	613 (100)	800	[103]
MnO on Gr	Solution based, subsequent reduction	891	200	843 (400)	2000	[106]
$ZnFe_2O_4$@C/Gr	Solvothermal, mussel inspired	1059/688	232	705 (180)	232	[110]
Hollow mesoporous $CoFe_2O_4$ nanospheres/Gr	HT	1459/942	100	805 (300)	2000	[109]
Nanocubic $CoFe_2O_4$/Gr	HT	1473/953	200	835 (200)	1000	[112]
MoS_2 and N-doped Gr (MoS_2/NG)	HT	1884/818 at 200	200	817 (120)	200	[137]
3D Gr aerogel/hollow α-Fe_2O_3 nanotubes	HT	1973/1320	100	1512 (65)	100	[114]
Nanoporous CoO NW/3-D porous Gr	HT; annealing	1493/1231	200	1246 (350)	500	[116]
Black phosphorus/Gr	Solvothermal	2587/1836	-	1401 (200)	100	[138]
Mesoporous manganese sulfide spheres/Gr sheets	In situ solvothermal	1444/1231 at 50	50	735 (300)	200	[139]

Covalent bonds, which are chemically stable, can give great mechanical integrity and an electrical connection between two materials [140,141]. SnO_2 cycle performance can be improved by creating a nanostructure with covalent bonds. Zhang et al. created a phosphorus covalently crosslinked SnO_2 and graphene (reduced from graphene oxide (GO) and indicated as SnO_2@P@GO, Figure 5b) [92]. Phosphorus covalently connects both Gr and SnO_2 nanocrystals in this unusual structure via P-C and Sn-O-P bonding, respectively, and acts as a buffer layer during charging and discharging (Figure 5b). As a result, SnO_2@P@GO can support the large volume variation of SnO_2 while retaining outstanding structure integrity and exhibiting long-life, high-rate cycling. As a result, when used as the anode of a LIB, SnO_2@P@GO demonstrated excellent stable performance, preserving 95% of the second capacity after 700 cycles at a current density of 1 A/g. An elastic conductive network and fast electron transport were provided by Gr. Even after 700 cycles, the SnO_2 particles are completely wrapped up by Gr rather than being exposed to the electrolyte, improving the structure's stability even further.

Pseudocapacitance arises when quick, reversible faradaic reactions occur on or near the surface of an electrode material, causing charge accumulation in the interfacial region. The surface area affects the pseudocapacitive storage of transition-metal oxide electrodes. If the surface area grows, the pseudocapacitive becomes more significant. Most carbon nanomaterials with a large surface area, such as porous Gr, simply provide large pseudocapacitance for delithiation. Consequently, pseudocapacitive storage has a direct impact on rate capability and cycling performance. Wu et al. [93] found that increasing the capacity of C/Fe_3O_4/rGO for 300 cycles resulted in pseudocapacitive behavior, as illustrated in Figure 5d. This is related to the transition of Fe_3O_4 nanoparticles into smaller ones after 100 cycles. Figure 5e,f show a comparison of C/Fe_3O_4/rGO's capacitive effect and diffusion effects. This study adopts a two-step strategy to developing a double carbon layer 3D network composite anode material of C/Fe_3O_4/rGO for LIB. First, GO is utilized to hydrothermally produce interlayer cauliflower-like Fe_3O_4. Then, a layer of carbon source is applied to the surface of Fe_3O_4/GO and the result is annealed to create the C/Fe_3O_4/rGO composite. Annealing increases the surface interaction of Fe_3O_4, rGO, and carbon (Figure 5c). Carbon material applied to the surface of Fe_3O_4/rGO can improve conductivity and electron transport in the electrode. This 3D nanostructure limits the volume growth of the C/Fe_3O_4/rGO composite throughout charging and discharging. After 300 cycles, the C/Fe_3O_4/rGO composite had a specific capacity of 844 mAh/g (at 0.2 A/g cycling) and outstanding rate capability (Figure 5d). Furthermore, cyclic voltammetry analysis of the pseudocapacitance of the C/Fe_3O_4/rGO composite at various scan rates demonstrates that the material contains a significant amount of pseudocapacitance. At 0.1, 0.4, 1.2, 2.4, and 5 mV/s, pseudocapacitance constitutes 31, 37, 49, 57, and 77% of total capacity, suggesting that the C/Fe_3O_4/rGO composite exhibits considerable pseudocapacitance behavior during high rate performance (Figure 5f). Figure 5e depicts the separation of capacitance and diffusion currents at a 2.4 mV/s scan rate. The electrochemical performance of Fe_2O_3/rGO produced by oleic acid-assisted HT in situ is characterized by a first-cycle discharge capacity of 1431 mAh/g at a current density of 100 mA/g, which decreases to 600 mAh/g after 30 cycles [142]. The cycle reversible capacity remains at 478 mAh/g after 50 cycles. Gr has a conductive network that greatly improved conductivity and electrolyte transfer. The steric hindrance of Gr may limit the crystal formation of iron oxide, enhance or decrease its active site, and reduce the route of Li-ions in the crystal [142].

In addition to binary compounds, ternary compounds were employed to form Gr composites. Ternary nanocomposite, as an alternative material, demonstrated increased capacity and reduced volume expansion. Zn_2GeO_4 nanorod/Gr composites (ZGCs) were produced using a two-step HT procedure [107]. A single Zn_2GeO_4 nanorod had both crystalline and amorphous areas. Gr sheets were used to compactly cover and anchor the Zn_2GeO_4 NR surface. As an anode for LIBs, partially crystalline ZGC containing 10.2 wt% Gr exhibited excellent electrochemical performance: reversible capacity of 1020 mAh/g in the first cycle, cyclic performance of 768 mAh/g after 50 cycles, and excellent rate capability of 780 mAh/g at a current density of 0.8A/g. The amorphous zone in partly crystalline Zn_2GeO_4 NRs and the elastic Gr sheets allowed for volume changes during the charge and discharge processes. Xia et al. reported a ternary nanocomposite of rGO/Fe_2O_3/SnO_2 formed by homogenous precipitation of Fe_2O_3 nanoparticles onto GO, followed by reduction of GO with $SnCl_2$ [102]. SnO_2 nanoparticles were deposited on the GO surface when the GO was reduced. Fe_2O_3 nanoparticles (20 nm) were uniformly disseminated in the Gr nanocomposite, surrounded by SnO_2 nanoparticles. Because of the differing Li insertion/extraction potentials, the primary role of SnO_2 nanoparticles during cycling is to inhibit Fe_2O_3 aggregation. Gr can act as a matrix for Li^+ and electron transport, alleviating stress that would otherwise accrue in the Fe_2O_3 nanoparticles during Li absorption and release. The electrochemical performance of a ternary nanocomposite of rGO/Fe_2O_3/SnO_2 as an anode in LIBs has been greatly enhanced, with initial discharge and charge capacities of 1179 and 746 mAh/g, respectively. Nearly 100% charge–discharge efficiency was maintained over the next 100 cycles with a specific capacity of >700 mAh/g.

As with CNT, Gr has been frequently alloyed or mingled with Si to increase Li storage capacity. Mn, like Si, is an alloying anode material having an excellent capacity; however, its performance is limited by large volume expansion. A ternary nanocomposite of Si, Mn, and rGO (Si–Mn/rGO), wherein the Si–Mn alloy offers high capacity properties and embedded rGO nanosheets provide structural stability, was prepared by mechanical complexation and thermal reduction of Si nanoparticles, MnO_2 nanorods, and rGO nanosheets in combination [143]. The LIB anode material had a specific capacity of 600 mAh/g and retained around 90% capacity after 50 cycles at 100 mA/g. The improved performance is due to facilitated Li-ion interactions with the MnSi alloy phase, as well as the creation of a structurally reinforced electroconductive matrix composed of rGO nanosheets.

$CoFe_2O_4$, a binary transition-metal oxide, is an attractive option due to its high theoretical capacity (916 mA h/g) and thermal/chemical stability [144,145]. $CoFe_2O_4$, like other transition-metal oxides (TMOs), undergoes significant volume change during cycling, causing pulverization and aggregation. This destroys the electrode's structural integrity and causes a loss of electrical connection with the current collector, resulting in rapid capacity fading [146]. Furthermore, $CoFe_2O_4$'s innately low conductivity makes it difficult to achieve excellent electrochemical performance [147]. Combining $CoFe_2O_4$ electrodes with carbon materials including carbon nanofiber [148], nanotubes, nanosheets [149], and Gr [150] is a typical technique to improve its electrochemical performance.

A simple one-pot technique was used to create a nanocomposite of $CoFe_2O_4$ nanocubes (edge length of ~5–15 nm) that were evenly distributed and adhered to Gr [112]. The results reveal that the inserted Gr oxide can cause nanocubic $CoFe_2O_4$ to form as well as close the junction between $CoFe_2O_4$ and Gr (Figure 7a). The plane-to-plane contact mode between $CoFe_2O_4$ nanocubes and Gr nanosheets in the composite nanostructure not only facilitates electron and ion interfacial transport, but also ensures the overall structural integrity of the $CoFe_2O_4$/Gr electrode during cycling. The $CoFe_2O_4$/Gr electrode has high cycling performance (1109 mA h/g after 100 cycles at 0.2 A/g and 835 mA h/g after 200 cycles at 1 A/g) (Figure 7b) and rate capability (420 mA h/g at 5 A).

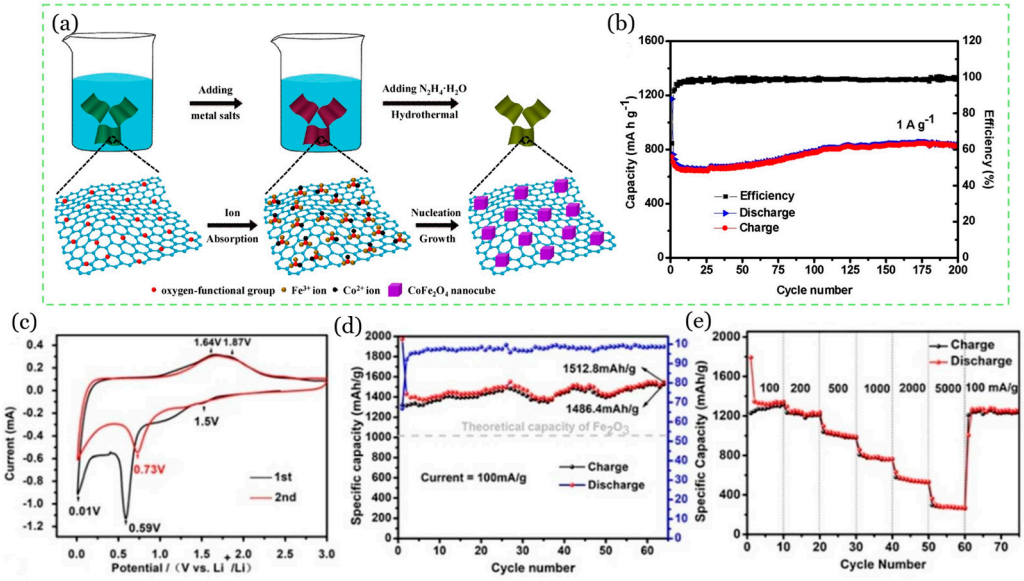

Figure 7. (**a**,**b**) One-pot synthesis of $CoFe_2O_4$/G. (**a**) Illustration of synthesis procedure for $CoFe_2O_4$/Gr; (**b**) cycling performance of the $CoFe_2O_4$/G electrode at 1 A/g. Adapted with permission from ref. [112]. © 2018 Elsevier B.V. (**c**–**e**): Hollow α-Fe_2O_3 nanotubes embedded in Gr aerogel; (**c**) CV curves of the first and second cycle for the c electrode; (**d**) cyclability of specific capacity and coulombic efficiency between 0.01 V and 3 V at a current density of 100 mA/g; (**e**) rate performance of the material at stepping current density and back to 100 mA/g at last. Adapted with permission from ref. [114]. © 2019 Wiley-VCH Verlag GmbH & Co. KGaA, Weinheim.

Wang et al. used a one-step HT method to create an α-Fe_2O_3 hollow nanotube (HNT)/Gr aerogel (GA) hybrid that enhances hematite characteristics by controlling the shape and mixing with 3D Gr [114]. There was no polymerization agent added to the Gr polymerization conditions. The α-HNTs/GA demonstrated remarkable electrochemical characteristics, with a specific capacity of ~1500 mAh/g and a consistent rate performance of 280 mAh/g at 5 A/g after 55 cycles. Furthermore, the high capacity retention, reversibility, and coulombic efficiency could be attributed to the synergistic effect of Gr sheets with hematite and the specific hollow nanotube morphology of Fe_2O_3, both of which buffered the large volume change caused by the insertion/extraction reaction of Li^+ ions. Furthermore, the 3D porous framework structure of GA, with a large BET area and a high hematite load on GA, contributed to its high initial specific capacity. The electrochemical properties of α-HNTs/GA as an anode material were studied using CV at a scan rate of 0.2 mV/s for the first two cycles (Figure 7c). Figure 7d depicts the specific capacity obtained during galvanostatic discharge–charge testing with a current density of 100 mAh/g. During the first cycle, the specific discharged and charged capacities were ≈1973 and 1320 mAh/g, respectively, resulting in an initial coulombic efficiency (ICE) of around 67%. In subsequent cycles, the specific capacity and CE tended to stabilize and then increase. After 65 cycles, the specific capacity reached 1512 mAh/g discharged and 1406 mAh/g charged, with a CE level of 97% to 99% and a rising trend. Figure 7e depicts the material's rate performance at varying current densities, culminating at 100 mA/g.

In contrast to conventional electrodes, a freestanding binder-free electrode film eliminates the usage of electrochemically inactive components such as conductive additives, and/or current collectors, which account for around 20% of the total battery weight. Zhou et al. used a simple HT reaction and subsequent annealing to create nanoporous CoO nanowire clusters on 3D porous graphene fabric (CoO-NW@GC) [116]. The self-supported Gr cloth has a large surface area, high porosity, and superior electric conductivity, all of which can contribute significantly to fast electron and ion transport. The CoO-NW@GC hybrid as an anode for LIBs achieves 1190 mAh/g and 429 mAh/g under current densities of 0.2 A/g and 3.2 A/g, respectively, due to the nanoporous CoO nanowire clusters uniformly depositing on the solid 3D skeleton of the GC substrate. The capacity was still 1100 mAh/g after more than 200 cycles at a current density of 0.5 A/g.

SnO_2/Gr nanocomposites were created using a chemical technique in which surface charge control leads echinoid-like SnO_2 nanoparticles to form and be uniformly decorated on Gr [97]. Under regulated pH, the electrostatic attraction between a Gr nanosheet (GNS) and echinoid-like SnO_2 particles results in a novel nanostructure with extremely small SnO_2 particles uniformly spread on the GNS. After 50 cycles, the anode preserved a reversible capacity of 634 mAh/g and a coulombic efficiency of 98%. The great reversibility can be attributed to the GNS's mechanical buffering against the substantial volume change in SnO_2 during the delithiation and lithiation reactions. Additionally, the nanostructure considerably improves power capability by allowing easy electron transport across the GNS and rapid delithiation and lithiation processes within the echinoid-like nano SnO_2.

Using a combination of processes, including in situ metal tin reduction, spray drying, and thermal treatment, a SnO_2/rGO composite was fabricated [98]. Under moderate HT conditions, metal tin acts as a reducing agent for few-layered graphene oxide (GO) for generating restacked 2D rGO sheets and a metal source for homogeneously dispersed nanostructured Sn and Sn oxides (Sn/SnO/SnO_2). After heat treatment, a SnO_2/rGO composite is generated, in which Sn and SnO species are converted to SnO_2, and the micro-sized 3D porous rGO supporting framework effectively stabilizes the nanosized SnO_2. When compared to its 2D counterpart, the 3D SnO_2/rGO composite has a greater reversible capacity of 708 mAh/g under a current density of 500 mA/g over 150 cycles, as well as a long and stable cycling life under a high current density of 1000 mA/g.

Recent investigations show that element doping improves the electrical conductivity and chemical stability of SnO_2 materials [151–153]. SnO_2-based anodes with transition-metal doping have significantly improved electrochemical performance [154,155]. A hybrid

material comprising cobalt-doped SnO_2 and Gr sheets (Co-SnO_2@GS) was created using a co-hydrolysis method to improve the electrochemical performance of SnO_2-based anodes [100]. In this hybrid structure, several Co-SnO_2 nanoparticles (4–7 nm) are uniformly positioned on the GS. Additionally, Co doping can improve the interface interactions between SnO_2 and GS. The Co-SnO_2@GS hybrid, which benefits from the synergistic effects of Gr hybridization and Co doping, has dramatically improved Li storage capability when compared to undoped SnO_2@GS and bare SnO_2. Figure 8a compares the cyclic performance of Co-SnO_2@GS, SnO_2@GS, and SnO_2 electrodes at 0.1 A/g. As demonstrated, the cyclic performance of Co-SnO_2@GS is clearly superior to that of undoped SnO_2@GS and bare SnO_2. Figure 8b examines the dealloying and conversion capabilities of SnO_2@GS and Co-SnO_2@GS. After 200 cycles, a steady capacity of ~828.5 mAh/g is still possible, with 83.2% retention from the sixth cycle (Figure 8c). Furthermore, this hybrid material has an excellent rate performance with a capacity of 674.7 mAh/g at 1 A/g.

A one-step HT synthesis approach was used to create SnO_2/$NiFe_2O_4$/graphene (SNG) nanocomposites for LIBs [103]. The nanocomposites exhibit good electrochemical performance due to the synergistic effect of Gr, $NiFe_2O_4$, and SnO_2 nanoparticles. The electrochemical performance improved as the SnO_2 level increased. After 50 cycles, a nanocomposite containing 50% SnO_2 has a high reversible capacity of 731.5 mA h/g at a current density of 200 mA/g, which can retain 80.9% of the initial cycle. After 100 cycles, the material has a comparatively high discharge capacity of 613 mA h/g at 800 mA/g. These increased electrochemical performances are related to the potential of $NiFe_2O_4$/SnO_2 buffer layers, which prevent electrode material pulverization during Li insertion and extraction. Furthermore, Gr sheets can enhance electrical conductivity and retard volume change to some level, allowing the structure to remain integrated and improving cycling stability and rate capability.

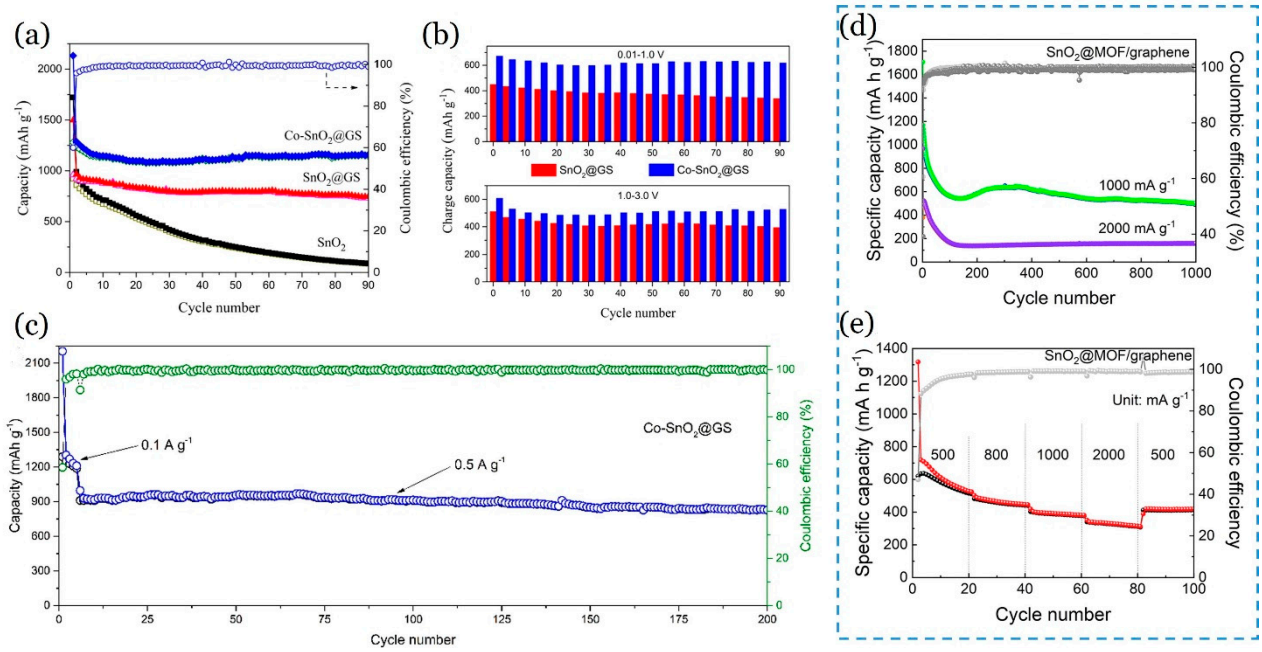

Figure 8. (**a**) Cyclic performances of the Co-SnO_2@GS, SnO_2@GS, and SnO_2 at 0.1 A/g with the CE of Co-SnO_2@GS; (**b**) charge capacities of Co-SnO_2@GS and SnO_2@GS from voltage regions of 0.01–1.0 and 1.0–3.0 V; (**c**) cyclic performance and corresponding CE of Co-SnO_2@GS at 0.5 A/g. Adapted with permission from ref. [100]. (**d**,**e**): MOF/SnO_2/Gr. (**d**) SnO_2@MOF/Gr at current densities of 1000 and 2000 mA/g; (**e**) rate performance of SnO_2@MOF/Gr at current densities of 500, 800, 1000, 2000, and 500 mA/g, respectively. Adapted with permission from ref. [101]. © 2020 Elsevier Ltd.

The particle size of SnO_2 plays a crucial role in controlling the reversibility of the conversion reaction from SnO_2 to Sn ($SnO_2 + 4\ Li^+ + 4e^- \leftrightarrow Sn + 2Li_2O$) for Li storage [156].

That is, the size of the SnO_2 particles is important to the anode material's capacity. Nano-sized SnO_2 can shorten electron and Li-ion diffusion paths, endure substantial volume fluctuations, and increase electrolyte–anode contact [157]. Several strategies for adjusting the particle size of SnO_2 have been proposed [158,159], including altering temperature, pressure, and additives. Metal–organic frameworks (MOFs), a new type of porous material, have sparked widespread interest in recent years [160]. MOFs, with their enormous specific surface areas and variable pore diameters, have shown great promise in gas adsorption and separation, catalysis, and drug delivery [161]. Furthermore, because MOFs are made up of metal ions and organic ligands, they are thought to be good precursors or templates for the development of TMOs/carbon hybrid materials [162].

Gao et al. developed the SnO_2@MOF/Gr composite anode, in which SnO_2 nanoparticles are packed into an Al-MOF. A wet impregnation technique traps SnO_2 nanoparticles inside the pores of Al-MOF. As a result, Al-MOF can tolerate SnO_2 volume variations during charge and discharge cycles and retain a stable SEI film. During the electrochemical alloying–dealloying process, Sn nanoparticles generated from SnO_2 tend to coalesce into bigger Sn clusters, resulting in capacity decline [163]. The Al-MOF layer in the SnO_2@MOF/Gr composite, on the other hand, will be capable of efficiently preventing Sn clustering. Due to the low electronic conductivity of SnO_2 and MOF, Gr sheets were used to surround the SnO_2@MOF composite to improve electronic conductivity. Furthermore, Gr has a reasonable theoretical capacity as an anode material, in addition to a large surface area and excellent mechanical flexibility [164]. After 1000 cycles, the SnO_2@MOF/Gr anode had a capacity of 450 mAh/g at a current density of 1000 mA/g, whereas the pure SnO_2 anode had essentially no capacity after 50 cycles (Figure 8d). Figure 8e depicts the rate capability of SnO_2@MOF/Gr at 500, 800, 1000, and 2000 mA/g, with high stable capacities of 565, 450, 385, and 324, respectively. After 100 cycles, the capacity recovers to 410 mAh/g as the current density drops to 500 mA/g.

$ZnFe_2O_4$ exhibits a high theoretical capacity (1000.5 mAh/g), making it a viable anode material for LIBs. However, rapid capacity fading and low rate capability pose practical challenges to its utilization [165,166]. $ZnFe_2O_4$@C nanoparticles with a core-shell structure were uniformly bonded to Gr nanosheet surfaces using a method inspired by mussels and calcination. Among the reported $ZnFe_2O_4$ anodes, the resulting $ZnFe_2O_4$@C/G nanocomposite exhibited one of the best Li storage properties, delivering a reversible capacity of 705 mA h/g at 0.25 C after 180 cycles (with a capacity retention of 99.4%) and an elevated rate capability of 403.5 mAh/g at 5 C. The excellent electrochemical performance is mostly owing to the conductivity, buffering, and shielding properties of carbon shells and Gr nanosheets on $ZnFe_2O_4$ nanoparticles.

Manganese monoxide (MnO) is a particularly appealing manganese oxide due to its high theoretical capacity (755 mAh/g), high density (5.43 g/cm^3), comparatively low electrochemical motivation force (1.032 V vs. Li/Li$^+$), low cost, and good natural abundance [167]. Despite these major characteristics, MnO is still limited by its low rate capability, which stems from weak conductivity and rapid capacity fading caused by large volume expansion and severe electrode collapse during the cycle operations [168]. Wang et al. used a simultaneous electrospinning and electrospraying method, followed by heat treatment, to create a CNFs/MnO/rGO film for high-performance LIB anodes [111]. The 2D reduced Gr sheets are dispersed on each of the 1D CNFs/MnO composite filaments to obtain freestanding and binder-free composite film electrodes, which not only improves the material's electrical conductivity and flexibility but also increases the specific surface area, resulting in a significant increase in specific capacity. Because of the large elastic buffer region, it was revealed that the CNFs/MnO/rGO framework film could successfully handle volume changes in MnO particles. The composite electrode has a high discharge capacity of 1118 mAh/g at 0.1 A/g and then returns to 0.1 A/g after 80 cycles, with capacity retention of up to 98%; at high rates (e.g., 5 A/g), the composite maintains a high reversible capacity of 574 mAh/g after 3000 cycles with a substantial coulombic efficiency of 99%. Furthermore, this method offers a simple way of combining 1D fibers/2D nanosheets in a

composite film with a controllable fiber diameter using simultaneous electrospinning and electrospraying methods.

The Kirkendall effect [169] (Section 4) and a simple etching technique were used to create a hollow Co_3O_4 (H-Co_3O_4) NP-embedded porous rGO (H-Co_3O_4/P-rGO) nanocomposite, which served as a model study for other TMOs [115]. Structure wise, one nanoparticle (NP) had one carved pore around it. It has outstanding reversible capacity (1016 mAh/g after 200 cycles at 0.2 A/g, Figure 9b), strong rate performance (810 mAh/g at 0.5 A/g, 510 mAh/g at 10 A/g), and good cycling endurance when used as an anode for LIBs. As a control sample, a Co_3O_4 NP-embedded porous reduced graphene oxide (Co_3O_4/P-rGO) composite was also made to highlight the benefits of hollow structured Co_3O_4 in H-Co_3O_4/P-RGO. Figure 9a compares the rate performance of H-Co_3O_4/rGO and Co_3O_4/P-rGO at rates ranging from 0.1 to 10.0 A/g. The discharge capacity of H-Co_3O_4/P-rGO is 840, 810, 760, 620, and 510 mA h/g at rates of 0.1, 0.5, 1.0, 5.0, and 10.0 A/g, respectively. Co_3O_4/P-rGO has discharge capacities of just 580, 530, 490, 360, 260, and 90 mAh/g at the same current densities.

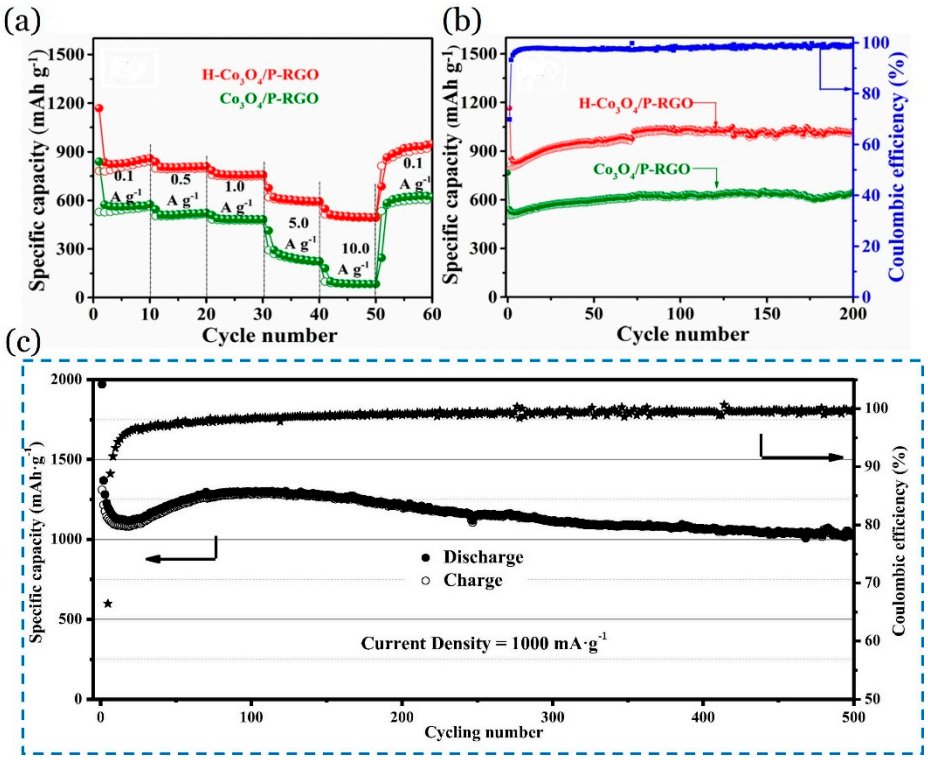

Figure 9. (**a**,**b**): H-Co_3O_4/PrGO. (**a**) The comparisons of rate performance (current densities, from 0.1 to 10.0 A/g); (**b**) cycling performance of H-Co_3O_4/P-rGO, Co_3O_4/P-rGO, and corresponding coulombic efficiency over 200 cycles (current density: 0.2 A/g). Adapted with permission from ref. [115]. © 2020 Elsevier B.V. (**c**) Cycling capability of the $ZnFe_2O_4$/rGO electrode at the current rate of 1000 mA/g. A line with stars indicates how the coulombic efficiency varies with cycle number. Adapted with permission from ref. [117]. © 2020 Elsevier Inc.

Among the currently studied anode materials, $ZnFe_2O_4$ is a promising binary transition-metal oxide (TMO) anode material with a high theoretical capacity (1000 mAh/g) due to its combination of conversion and alloy Li-ion storage mechanisms, cost-effectiveness, abundance, eco-friendliness, and a low discharging voltage plateau of ~1.5 V [170]. Furthermore, the $ZnFe_2O_4$ crystal has an AB_2O_4 spinel structure, in which oxygen is cubically close-packed to establish a 3D framework for Li-ion diffusion. As a result, the binary $ZnFe_2O_4$ anode can exhibit increased electrochemical activity [171]. The quick reversible capacity fading throughout each cycle, induced by both pulverization caused by massive volume changes and the $ZnFe_2O_4$ crystals' weak inherent electrical

conductivity, is undesirable [172]. As a result, hybridizing nanostructured $ZnFe_2O_4$ with a conductive and flexible carbon supporting framework is one of the most effective ways.

Immobilizing nanosized electrochemical active materials with a 3D porous framework made of conductive Gr sheets improves Li-ion storage characteristics [117]. A simple approach is used to create a rGO-supported zinc ferrite ($ZnFe_2O_4$) composite anode material ($ZnFe_2O_4$/rGO). To begin, a redox reaction occurs between oxygen-containing functional groups on multilayered graphene oxide (GO) sheets and a regulated quantity of metallic Zn atoms. ZnO nanoparticles are nucleated in situ and grow directly on GO sheets. Second, numerous Fe atoms totally reduce the GO sheets, resulting in the formation of γ-Fe_2O_3 nanoparticles next to the ZnO nanoparticles. This stage involves building a 3D porous rGO supporting framework with γ-Fe_2O_3@ZnO nanoparticles efficiently contained between the rGO layers. Finally, the γ-Fe_2O_3@ZnO/rGO intermediate product is thermally treated to allow for a solid-state reaction, resulting in the $ZnFe_2O_4$/rGO composite. The $ZnFe_2O_4$/rGO composite has a high reversible capacity of 1022 mAh/g for 500 consecutive cycles at a high current rate of 1.0 A/g (Figure 9c).

Wang et al. presented a high-performance anode material made of tungsten-doped SnO_2/rGO composite synthesized using the one-pot HT technique [173]. Tungsten ions were doped inside the unit cells of tin dioxide rather than just sticking to its surface. Tungsten-doped SnO_2 was formed in situ on Gr sheets, creating a three-dimensional conductive network that improved electron transport and Li-ion diffusion. Tungsten-doped SnO_2 nanoparticles were evenly placed on a Gr sheet, preventing potential problems with aggregation and volume expansion. As a consequence, the nanocomposite electrodes comprising tungsten-doped SnO_2 and reduced graphene oxide demonstrated long-term cycling properties. After 100 cycles, the residual capacity remained as high as 1100 mAh/g at 0.1 A/g. It stayed at 776 mAh/g after 2000 cycles with a current density of 1 A/g.

Heteroatom-doped Gr can improve cycle performance, first cycle charge–discharge capacity, and Li storage capacity through facilitating Li-ion contact with active sites. Heteroatom doping (B, N, F, S, or P) increases electrochemical performance because Li-ion storage is affected not only by heteroatom contents, but also by synergistic coupling effects between heteroatoms [174–176]. Recent theoretical investigations have shown that doped Gr is more efficient at storing Li-ions due to increased defects in the Gr plane [177,178].

First-principles calculations were performed to investigate the effects of electron deficiency in N-doped Grs on their application in LIBs. Three different defect models, graphitic, pyridinic, and pyrrolic Grs, were used [177]. The pyridinic Gr was found to be the most suitable for Li storage with a high storage capacity, while the graphitic structure was the weakest of the three. It was discovered that the reversible capacity of the pyridinic structure can reach 1262 mAh/g, which is greater than the experimental 1043 mAh/g. Figure 10a shows a comparison of the most stable sites after Li atoms adsorbed on Gr sheets having different defects. Figure 10b depicts the hybridization peaks of the N and Li atoms in pyridinic and pyrrolic N-doped Gr. The binding energy between Li and pyridinic Gr is higher than for graphitic Gr. Figure 10c shows the avg. intercalation voltage of Li in the pyridinic, pyrrolic, and defect Grs, indicating the highest voltage when nine atoms of Li are embedded.

Graphite oxide (GO), tri-block co-polymer P123, and thiourea were used as the N and S sources in the HT technique and heat treatment to synthesize N and S co-doped mesoporous graphene (NSMG) [179]. XPS analysis of the NSMGs revealed the presence of active pyridinic-N, pyrrolic-N, graphitic-N, pyridinic N-oxide, thiophene, and -SO_x groups in the structure. Annealing temperature was used to adjust the N and S content. Super capacitors and LIBs showed enhanced electrolyte ion mobility and Li-ion diffusion, respectively; this could be related to structural characteristics such as numerous pores and defects, wrinkles, and N/S co-doping. NSMG treated at 600 °C had the maximum capacitance of 261 F/g at 0.5 A/g in supercapacitors, whereas NSMG treated at 800 °C had the best performance in LIBs with a discharge capacity of 460 mAh/g at 100 mA/g, good cycle stability (440 mAh/g), and higher rate capability. The high capacity of the

NSMG (800 °C) is due to the stable and desired residual oxygen, such as the carbonyl group (C-O), which increases with heat treatment [180]. Precursor-assisted CVD was used to prepare hierarchically porous graphene-like microspheres (3D NS-GSs) doped with N and S [181]. By employing $(NH_4)S_2O_8$ as a N and S dopant, the 3D NS-GSs have a larger surface area than pure Gr-like microspheres. The combination of large surface area and proper heteroatom doping resulted in a high reversible capacity, good rate capability, and long cycling stability in 3D NS-GS as the LIB anode. Doped Gr has an electron-adopting propensity in pyrrolic and pyridinic structures, and their sites may attract more Li-ions while adjusting the electronic characteristics of neighboring carbon atoms over the cycles [177,182]. As a result, N- and S-co-doped Gr sheets of 3D NS-GSs can accept more charge than pristine Gr sheets.

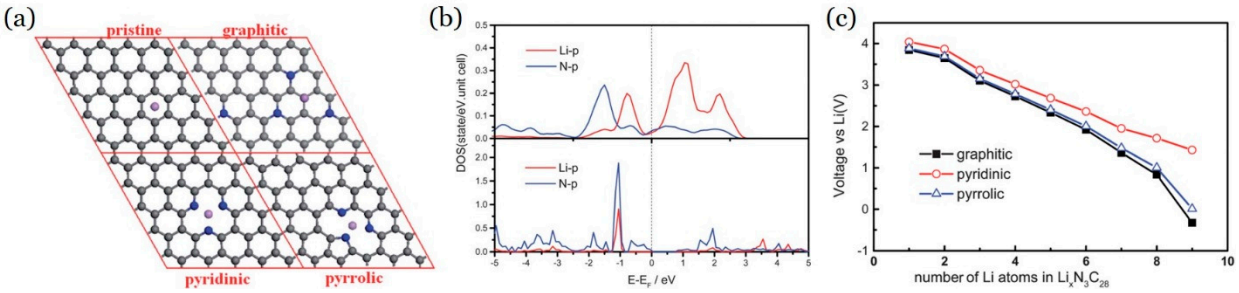

Figure 10. (**a**) An analysis of the more stable sites following Li atoms are adsorbed in defect Gr sheets. Li (pink); N (blue); and C (gray); (**b**) a comparison of the partial density of states (PDOS) of N atoms in graphitic (top panel) and pyridinic (bottom panel) Grs. The dashed line indicates the Fermi level; (**c**) a comparison of the avg. potential of Li intercalation in the graphitic, pyridinic and pyrrolic defect structures of Gr [177].

The addition of F atoms to the Gr surface effectively adjusts its electrical structures and creates surface defects [183]. N and F co-doped graphene (NFG) with N and F concentrations of 3.24 and 10.9 at%, respectively, was synthesized using the HT reaction of trimethylamine tri(hydrofluoride) $[(C_2H_5)_3N{\cdot}3HF]$ with aqueous-dispersed graphene oxide (GO) as an anode material for LIBs [184]. N and F co-doping in Gr raised the framework's disorder and defects, increased the interlayer space, wrinkled the nanosheets with multiple open-edge sites, and so improved Li-ion diffusion across the electrode compared to sole N or F-doped Gr. XPS study of NFG revealed the existence of active pyridine and pyrrolic type N, significantly higher electrically conductive graphitic N, and a semi-ionic C-F bond in the structure. The N and F doping content, as well as the component types of N and F functional groups, may be regulated by the high temperature. The NFG produced at 150 °C had a coulombic efficiency of 56.7% in the first cycle, reversible specific discharge capacity of 1075 mAh/g at 100 mA/g, rate capability of 305 mAh/g at 5 A/g, and excellent cycling stability (capacity retention of ∼95% at 5 A/g after 2000 cycles).

4. Three-Dimensional (3D) Carbon Nanostructured Composites

4.1. Carbon Nanospheres, Carbon-Coated Metal Oxide Nanospheres, Core-Shell Structures, and Doped Carbon-Coated Transition-Metal Oxides

Carbon nanospheres (CNSs) and carbon nanoporous (CNP) structures are also promising carbon nanostructures, alongside CNTs, nanofibers, nanorods, and Gr. As Li-ion battery anodes, CNSs and CNPs have excellent cycle stability and coulombic efficiency. If 3D carbon nanostructures are combined with proper electrolytes, they will produce a stable SEI. However, 3D carbon nanostructures alone have a poor capacity. To overcome this drawback, carbon nanospheres/nanoporous structures can be mixed with other materials to create composites. Carbon shells not only allow for volume expansion and contraction during charge storage, but they also assist electron transport. The combination of these two variables results in extended cycling stability and exceptional rate performance. Fur-

thermore, the broad surface can improve the contact area between the electrode and the electrolyte, which is advantageous for the use of active materials. The porous and hollow construction results in a short diffusion length of ions in the electrode, which improves electrochemical performance. One of the key factors for C hollow sphere (CHS)-based anodes is to boost the anode's areal and volumetric energy density by utilizing all CHS voids [185]. The carbon sphere's porous structure is divided into three types: micropores (avg. pore size < 2 nm), mesopores (2–50 nm), and macropores (>50 nm).

To synthesis diverse hollow micro/nanospheres, self-templated methods have been devised, including those based on the nanoscale Kirkendall effect (Figure 11a) [186], Ostwald ripening (Figure 11b) [187], galvanic replacement (Figure 11c) [188], and surface-protected etching [189]. These methods are particularly appealing since the hollow shells are created through a chemical reaction, and the template can be depleted spontaneously during the hollowing process. Methods based on the nanoscale Kirkendall effect offer a variety of benefits: high-quality colloidal nanocrystals with consistent sizes and shapes are readily produced, and their reaction with appropriate materials, together with the nanoscale Kirkendall effect, can produce extremely crystalline hollow nanocrystals with a high yield even in the quantum domain [190]. Ostwald ripening is a phenomena that occurs in solid or liquid solutions when small nanoparticles dissolve and are redeposited on larger nanoparticles [78]. This phenomenon is caused by small particles having a higher average surface energy, which causes material to evaporate (or dissolve) more quickly. At a constant amount of material, Ostwald ripening induces the evolution of a population of nanoparticles, resulting in less and fewer big aggregates surviving for long periods of time. The main step in galvanic replacement reactions is the replacement reaction between a suspension of nanoscale metal templates and a salt precursor containing a less active metal. Figure 11c depicts the schematic formation of a nanostructure made up of an Au/Ag alloy core and an Au/Ag alloy shell. In step (A), a conformal coating of pure silver is electrolessly deposited on the surface of an Au/Ag alloy nanoparticle; and (B), the resulting particle is reacted with an aqueous $HAuCl_4$ solution to change the pure silver coating into a bigger Au/Ag alloy shell. For a detailed discussion on the templating methods of HCS, readers are urged to refer to an article by Liu et al. [185].

The following is a list of some carbon nanospheres (CNSs) and nanoporous composites that contain metalloids and post-transition metal: xarbon-Si-SiO_2-CNS [191], Si/CNS [192], SiO_2-CHS [193], mesoporous C-SnO_2-CNS [194], double-shell structured Si@SnO_2@C [195], carbon-encapsulated SnO_2 hollow spheres [196], Si-TiO_2-CNS [197], and carbon-coated Si/carbon nanotube/GO (C-Si/CNT/GO) [198]. Several studies also detailed the effective production of composites containing metal oxide and heteroatoms: hollow carbon spheres with encapsulation of Co_3O_4 nanoparticles (HCSE-Co_3O_4) [199], core-shell porous Fe_3O_4@C nanospheres [200,201], core-shell structured ZnO@C nanosphere [202], TiO_2/CNS [203], ball-in-ball ZnO/$ZnFe_2O_4$@carbon nanospheres [204], α-Fe_2O_3/CNS [205], porous Mn_3O_4/C nanospheres [206], Co_3O_4-doped hollow hierarchical porous carbon spheres [207], Cu_2O/CNS [208], nitrogen-doped carbon-coated TiO_2 (TiO_2/N-C) [209], and Mn_3O_4/N-doped porous carbon sphere (NPCS) [210]. The electrochemical performance of a few hollow carbon sphere-based materials for LIBs that have been reported in the recent years is listed in Table 2.

The template approach and carbon thermal vapor deposition were used to create an interconnected sandwich-type composite of carbon/Si-SiO_2/carbon nanospheres [191]. The carbon conductive layer enhances the electronic conductivity of Si-based anodes and reduces volume expansion during discharge or charging. The interconnected sandwich carbon/Si-SiO_2/carbon nanospheres composite has strong battery characteristics, with a reversible capacity of 1094 mAh/g and a reversible capacity of 1050 mAh/g after 200 cycles, and a capacity retention of 96%. A simple method for creating SiO_2@C hollow spheres involves hydrolyzing tetraethyl orthosilicate (TEOS) to generate SiO_2 shells on organic spherical templates [193]. The shells are then calcined in air to remove the templates and carbon layers are used to cover them (Figure 11d). SiO_2@C hollow spheres with varying SiO_2

concentrations show a steady rise in specific capacity with discharge–charge cycling. The SiO_2@C with 67 wt% SiO_2 content has discharge–charge capacities of 653.4/649.6 mAh/g across 160 cycles at a current density of 0.11 mA/cm^2.

Table 2. Electrochemical performance of some hollow carbon sphere-based materials for LIBs. Abbreviation: HCS = Hollow carbon sphere.

Material	Highest Reversible Capacity (mAh/g)	Current Density (A/g)	Reversible Capacity (mAh/g)	Current Density (A/g)	Cycles	Ref.
Tin embedded in nitrogen-doped carbon shells	917	0.2	600	0.2	250	[211]
Yolk shell Sn@C microspheres	829	1.0	691	1.0	500	[212]
Tin nanoparticles encapsulated in HCS	1250	0.2 C	650	0.2 C	100	[213]
Ultra-small Tin embedded in carbon shells	743	0.5	423	4.0	6000	[214]
Fe_3O_4/C open hollow spheres	917	0.09	587	1.0 C	30	[215]
Fe_3O_4 in macropores of carbon HCS	1092	0.2	645	2.0	1000	[216]
α-Fe_2O_3@C hollow spheres	1136	0.1 C	1400	0.1 C	50	[217]
Fe_2O_3 nanoparticles embedded in N-doped HCS	1573	0.1 C	1142	1.0 C	100	[218]
F-doped Fe_3O_4/C hollow sphere	930	0.1 C	620	1.0 C	200	[219]
Yolk–shell structured Fe_3O_4@HCS	1010	0.15	750	1.0	70	[220]
Fe_2O_3 nanoparticles anchored on nitrogen-doped HCS	1120	0.1	702	0.5	65	[221]
Ge encapsulated in HCS	1270	0.4 C	1020	0.4 C	100	[222]
Coaxial SnO_2@C hollow spheres	520	0.32 C	475	0.8 C	100	[223]
NiSb embedded in carbon shell	667	0.05	497	0.1	100	[224]
Double-shelled SnO_2/C spheres	1100	0.25 C	911	0.25 C	100	[225]
Yolk-shelled SnO_2@C spheres	780	0.1	512	0.1	30	[226]
N-doped carbon/SnO_2 hollow sphere	1003	0.16 C	910	0.16 C	100	[227]
SnO_2/C hollow core–shell spheres	640	0.05	576	0.05	100	[228]
SnO_2/C hollow nanospheres	983	0.1	473	0.1	50	[229]
SnO_2/C hollow microspheres	700	0.2	550	0.5	100	[230]
SnO_2/C/MnO_2 hollow sphere	800	0.1	644	0.1	200	[231]
Nanosized SnO_2 embed in HCS	627	0.2	501	0.2	100	[232]
SnO_2/Fe_2O_3/C hollow sphere	1147	0.2	475	2.0	1000	[233]
Si nanocrystallites sealed in HCS	1570	0.25	1020	0.25	250	[234]
Mesoporous SiO_2/carbon hollow sphere	624	0.1	560	3.0	180	[235]
Core-shelled SiO_2@C hollow sphere	153	0.11	653	0.11	160	[193]
Carbon-coated CuO hollow sphere	670	1 C	750	1 C	300	[236]
CoO nanoparticles encapsulated in HCS	584	0.1	554	0.1	50	[237]
Co_3O_4 nanoparticles encapsulated in HCS	732	0.074	732	0.074	20	[199]
Triple-shelled MoO_2/C hollow sphere	867	0.2	580	0.5	200	[238]
MnO_2/HCS with 3D network	900	0.1	692	0.1	100	[239]

Table 2. *Cont.*

Material	Highest Reversible Capacity (mAh/g)	Current Density (A/g)	Reversible Capacity (mAh/g)	Current Density (A/g)	Cycles	Ref.
HCS/MnO_2 nanosheets	947	0.1	826	0.5	140	[240]
Carbon-coated $CuFe_2O_4$ hollow sphere	815	0.1	550	0.1	100	[241]
ZnCo-oxide/C hollow sphere	992	1.0	823	4.0	1000	[242]
CeO_2/C hollow sphere	400	1.0	313	1.0	500	[243]
MoS_2 nanosheets coated HCS	1190	0.1	750	0.2	100	[244]
Bowl-like SiC encapsulated in HCS	1345	0.6	742	3	1000	[245]
C@TiO_2@MoS_2 hierarchical nanospheres	1030	0.2	993.2	0.2	100	[246]
WS_2-decorated nitrogen-doped HCS	801	0.1	631	0.5	150	[247]
SeS_2 impregnated in double-shelled HCS	1070	0.1 C	600	1 C	1000	[248]
Ni_3S_4/C hollow sphere	1003	0.1	480	1.0	500	[249]

For carbon-coated SnO_2 nanocolloids [250] and SnO_2/carbon hybrid hollow spheres [251], capacity deterioration occurs due to the aggregation of SnO_2 nanoparticles after repeated cycling. Furthermore, the SEI layer generated atop the typical core-shell structure is unstable because it cannot resist massive volume changes over long periods of time [252]. The dual carbon shell-coated SnO_2 hollow nanospheres (C@SnO_2@C) were created for stable LIBs by combining the benefits of porous carbon and hollow structured SnO_2 [194]. The double carbon shells served as a protective layer to stop the aggregation of nanosized SnO_2 and structural damage, in addition to acting as a conducting medium (Figure 11e). The C@SnO_2@C hollow nanosphere anode showed noticeably improved cycle stability and rate performance when compared to its counterparts, the pure SnO_2 hollow nanospheres and the carbon-coated SnO_2 nanospheres [250,251]. With the aid of a dually coated structure-based space-bound protection approach, the C@ SnO_2@C hollow nanospheres demonstrated an initial specific capacity of 1483.9 mAh/g at 200 mA/g and a reversible capacity of 713.8 mAh/g after 300 cycles, corresponding to a capacity fading of 0.071% per cycle from the 2nd to the 300th cycle. The rate performance of the C@SnO_2@C and pure SnO_2 electrodes (Figure 11f) shows that even at a low current density of 0.2 A/g, SnO_2 capacity rapidly decays, with almost no capacity remaining at 1.6 A/g and 3.2 A/g. Conversely, the C@SnO_2@C electrode outperforms pure SnO_2 hollow nanospheres in terms of rate. When the tested current density is reset to 0.2 A/g, the SnO_2 electrode has a negligible capacity of 62.3 mAh/g after 100 cycles, whereas the dually coated C@SnO_2@C electrode can recover a high reversible capacity of 675 mAh/g while remaining completely stable in subsequent cycles. The high rate capacity of the C@SnO_2@C composite is most likely attributable to its spatial double protection nanostructure and refined SnO_2 nanocrystals. The uniformly porous carbon layers can act as a highly conductive medium. Figure 11g displays C@SnO_2@C's long-term cycling performance at 5 A/g over 10,000 cycles.

Carbon-encapsulated SnO_2 hollow spheres for LIBs were created using a self-templating process from Sn spheres [196]. High-temperature annealing (for example, 700 °C) invariably resulted in the production of Sn on the outer surface, which was detrimental to long-term cycling. In contrast, annealing at an ideal temperature of 600 °C followed by acid etching totally encased the SnO_2 within a carbon shell while maintaining a stable hollow structure (Figure 12a). After 120 cycles, the as-prepared carbon-encapsulated SnO_2 hollow spheres (SnO_2@C-6H) demonstrated a reversible capacity of 898 mAh/g at 200 mA/g (Figure 12b) and a promising rate capacity of 549.8 mAh/g at a high current density of ~2000 mA/g (Figure 12c). The observed excellent outcomes might be related to

the development of a unique hollow structure with an increased specific surface area of 215.18 m^2/g and a reasonably high degree of graphitization of the carbon shell (i.e., Raman intensity ratio of D to G band, I_D/I_G = 0.84). The reason for this is that the acquired hollow spheres not only provide a barrier effect for volume expansion and SnO_2 aggregation, but also increase Li storage [196].

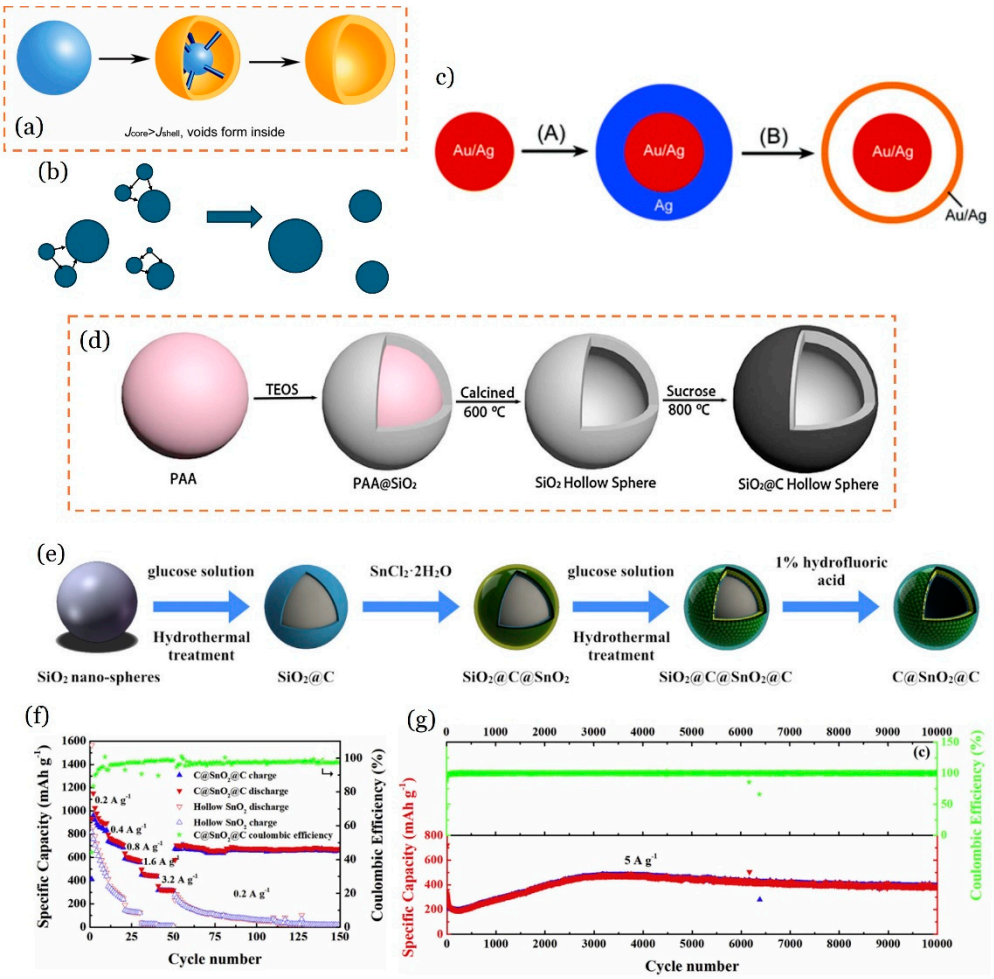

Figure 11. Hollow micro/nanosphere synthesis methods. (**a**) Schematic representation of the nanoscale Kirkendall phenomenon in the synthesis of hollow nanocrystals; J stands for diffuse flux [169]; (**b**) Ostwald ripening; (**c**) galvanic replacement. Illustration of the procedure for preparing a nanostructure consisting of Au/Ag alloy core and Au/Ag alloy shell [188]. Copyright © 2004, ACS. (**d**) Fabrication process of the SiO_2@C hollow spheres. SiO_2 shell is formed on the PAA (polyacrylic acid) sphere template, and then a C coating layer covers the shell after calcination of the template. Adapted with permission from ref. [193]. Copyright © 2017, The editorial office of Journal of Materials Science & Technology. (**e**–**g**): C@SnO_2@C composite. (**e**) fabrication steps of porous dual carbon shell-coated SnO_2 hollow nanospheres (C@SnO_2@C); (**f**) rate performance of the hollow SnO_2 and C@SnO_2@C electrodes at varying current density from 0.2 A/g to 3.2 A/g; (**g**) the long-term cycling performance of C@SnO_2@C at 5 A/g for 10000 cycles. Adapted with permission from ref. [194]. © 2019 Elsevier B.V.

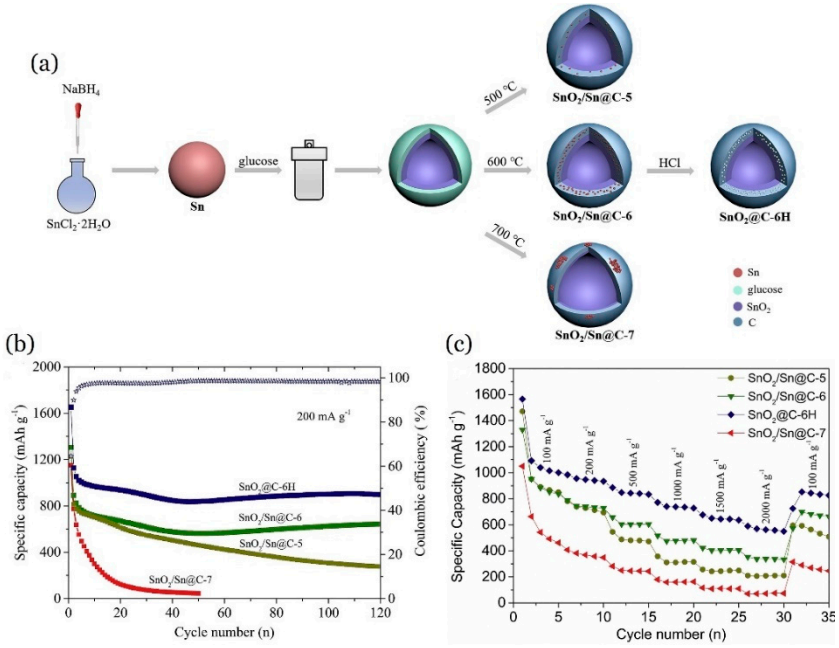

Figure 12. Carbon-encapsulated SnO_2 hollow spheres. (**a**) Schematic illustration of the synthesis of SnO_2/Sn@C-5, SnO_2/Sn@C-6, SnO_2@C-6H, and SnO_2/Sn@C-7; (**b**) cycling stability of SnO_2/Sn@C-5, SnO_2/Sn@C-6, SnO_2@C-6H, and SnO_2/Sn@C-7 at 200 mA/g; (**c**) rate capability of SnO_2/Sn@C-5, SnO_2/Sn@C-6, SnO_2@C-6H, and SnO_2/Sn@C-7. Adapted with permission from ref. [196]. © 2019 Elsevier B.V.

Many metallic oxide coatings on Si particles have been investigated to increase electrochemical performance, including Co_3O_4, MnO, and NiO [253–255]. However, due to their inherent shortcomings, most metallic oxides frequently experience large volume variations and poor structural stability [106]. In this sense, TiO_2 coating, with its simple synthesis procedure and strong cycling stability, stands out among the metallic oxide possibilities listed above and receives a lot of attention. TiO_2 particles have a fast (de)lithiation process with negligible volume expansion (<4%) and a high operating voltage from 1 to 3 V (vs. Li/Li^+), resulting in high electroconductivity and restrained exothermic reactions. This ensures an attractive and reliable battery by preventing the generation of dendritic Li and SEI [256]. One-step sol–gel coating and magnesiothermic reduction techniques were used to create the dual stabilized core-shell-shell Si-based composites with hollow spherical morphologies (Figure 13a,b) [197]. The Si@TiO_2@C nanospheres, as synthesized, have a high specific surface area of 280.9 m^2/g, a homogeneous carbon layer of ~3 nm thick, a TiO_2 interlayer of about 6 nm, and a hollow structured Si core with a shell of 124 nm. For this designed architecture, the hollow Si@TiO_2@C nanospheres achieve an initial discharge specific capacity of 2557.1 mAh/g at 0.2 A/g and a reversible steady capacity of 1262 mAh/g after 250 cycles at 1 A/g. Furthermore, after 400 cycles, the Si@TiO_2@C nanospheres maintain a reversible discharge capacity of 1058.3 mAh/g at 4 A/g (Figure 13c). When evaluated at greater current densities of 0.5 and 8 A/g, the Si@TiO_2@C nanospheres maintained discharge capacities of 2457.2 and 718.2 mAh/g (Figure 13d). The two shells, a rigid TiO_2 interlayer and a conductive outer carbon layer, can drive expansion into the cavity rather than the exterior, acting as a compact fence to keep the central Si core from breaking and pulverizing. They also provide numerous conductive pathways for rapid Li^+ transport and electron transfer, improving structural stability and electrical conductivity.

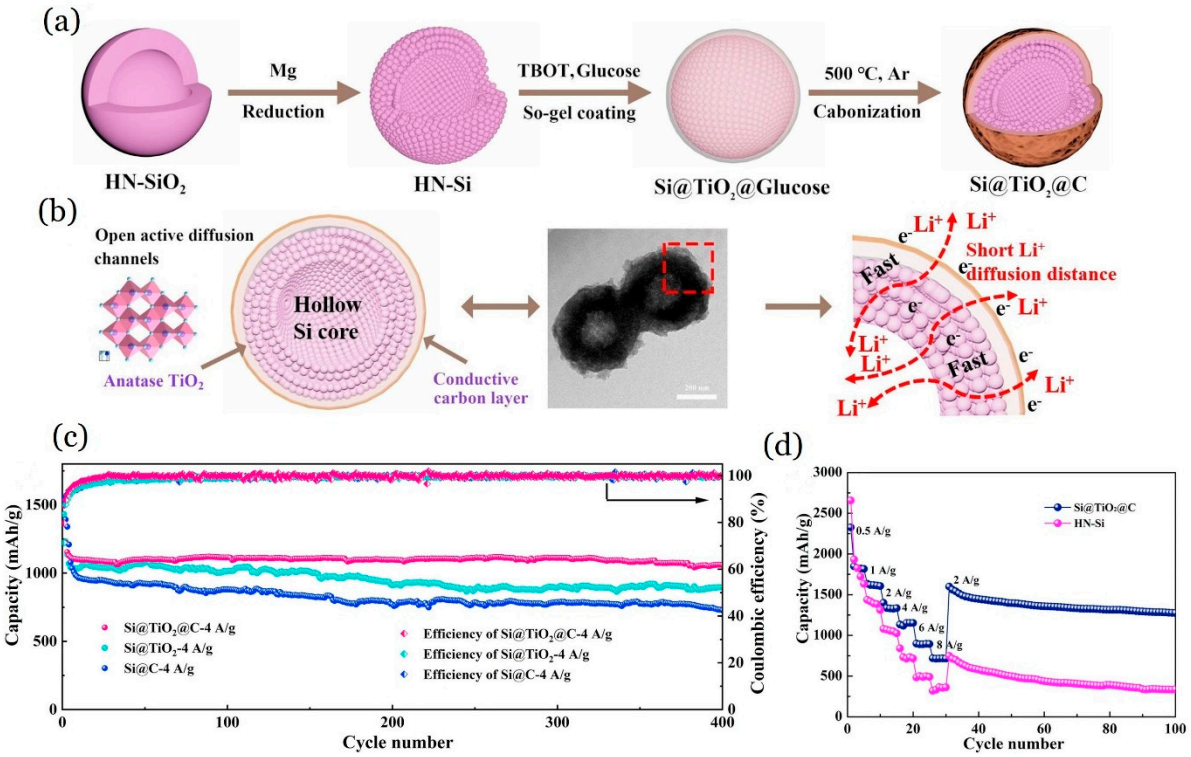

Figure 13. Hollow Si@TiO_2@C nanospheres. (**a**) Fabrication schematic of the hollow Si@TiO_2@C nanospheres by the one-step sol–gel coating process; (**b**) a dual stabilized monodisperse hollow Si@TiO_2@C nanosphere, which offers a stable and conductive framework and prevents the Si host from fracture and pulverization during the (de)lithiation processes; (**c**) the cycle behaviors for the hollow nanosphere (HN)-Si particles, TiO_2 particles, and the hollow Si@TiO_2@C nanospheres under various current densities; (**d**) rate capabilities for the HN-Si particles and the hollow Si@TiO_2@C nanospheres under various current densities. Adapted with permission from ref. [197]. © 2018 Elsevier B.V.

Carbon coating is a highly effective approach for improving the electrochemical performance of nanostructured TMOs. A scalable approach for fabricating hierarchical Fe_3O_4@C nanospheres has been developed [201]. The method of production consists of a one-step solvothermal synthesis of the Fe_2O_3/MIL-100(Fe) precursor coupled by an annealing treatment in Ar. The Fe_3O_4@C nanospheres (avg. size of ~200 nm) are composed of several interconnected nanoparticles with an amorphous carbon layer on the surface of Fe_3O_4, leading to a distinct hierarchical nanostructure with a greater specific surface area of 176.5 m^2/g. The comparison of rate capabilities of the hierarchical Fe_3O_4@C and hollow Fe_2O_3 electrodes (Figure 14a) reveals that the Fe_3O_4@C electrode provides high reversible specific capacities of 852.2, 736.5, 529.8, and 362.1 mAh/g at current densities of 200, 400, 800, and 1600 mA/g. In comparison, the hollow Fe_2O_3 electrode has lower specific capacities than the Fe_3O_4@C electrode at each rate studied. The hierarchical Fe_3O_4@C nanosphere electrode achieves a high capacity of 757.9 mAh/g after 500 cycles at a current density of 500 mA/g, indicating better high-rate Li storage performance (Figure 14a). This might be explained by the distinct hierarchical nanoarchitecture, increased specific surface area, and homogenous in situ carbon layer produced by MIL-100(Fe).

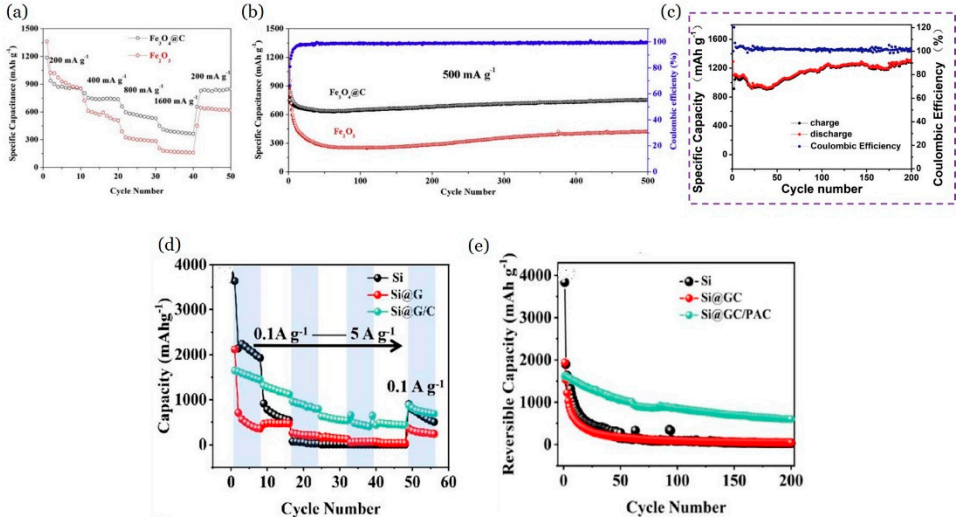

Figure 14. (**a**,**b**): Hierarchical Fe_3O_4@C nanospheres. (**a**) Rate performances of Fe_3O_4@C and Fe_2O_3; (**b**) long-term cycling performances of Fe_3O_4@C and Fe_2O_3 at 500 mA/g. Adapted with permission from ref. [201]. © 2018 Elsevier B.V. (**c**) Co_3O_4-doped hollow hierarchical porous carbon spheres. The cycling performance of S 6–8 at 0.2 A/g, where S 6–8 is a sample in which the molar ratio of glucose and cobalt nitrate in precursor solution is 6:8 during the preparation of hollow Co_3O_4-doped carbon microspheres. Adapted with permission from ref. [207]. © 2019 Elsevier Ltd. (**d**,**e**): Si@GC/PAC. (**d**) rate curves of pristine Si, Si@GC, and Si@GC/PAC; (**e**) rate curves. Adapted with permission from ref. [257]. © 2022 The Society of Powder Technology Japan, Elsevier B.V. & The Society of Powder Technology Japan.

As already mentioned, in Si-based anode materials, the considerable volumetric variability of Si has resulted in severe chalking and quick capacity loss. To tackle these problems, a carbon-coated Si matrix composite (Si@GC/PAC (PhyA-derived amorphous carbons)) with a 3D conductive network structure was created utilizing glucose and phytic acid [257]. In this case, glucose carbonization forms an indeterminate carbon coating that uniformly surrounds the Si nanoparticles, creating a distinct core-shell structure, while the controlled space between the Si nanoparticles and the carbon shell allows the Si nanoparticles to expand during the charge–discharge processes. In addition, the pyrolytic carbon formed by the PhyA's heat degradation wraps the outer layer, leading to a large surface area and a highly 3D conductive network. The arrangement offers various advantages: the uniform amorphous carbon coating can improve the electrical conductivity and mechanical stability of the Si anode. The carbon skeleton formed by PhyA can also handle the volume variation of the Si anode. Pyrolytic carbon, together with glucose's carbon coating, has a double limiting impact on volume expansion. The produced anode material, as modified by the two carbon sources, exhibits better structural and property synergy. The suitable doping of the glucose-based carbon matrix with phosphorus elements in the phytate can increase the interaction between Li-ions and the carbon coating. The developed Si@GC/PAC anode for Li-ion batteries has a reversible capacity of 1612 mAh/g at 0.1 A/g and retains 600 mAh/g after 200 cycles. Figure 14d shows the rates of bare Si, Si@GC, and Si@GC/PAC. The cycle stability of bare Si, Si@GC, and Si@GC/PAC was tested at 0.1 A/g, as shown in Figure 14e. After 200 cycles, the reversible specific capacity of the Si@GC/PAC composite remained at 600 mAh/g (56% of its initial capacity). The capacity of the bare Si and Si@GC electrodes was lowered to 652 and 766 mAh/g, respectively, with capacity retention rates of 20% and 27%.

Since α-Fe_2O_3 is abundant, nontoxic and inexpensive, and it has a larger theoretical capacity (1007 mAh/g), it is thought to be one of the most promising anode materials for LIBs with ultra-long cycle performance [206,207]. However, the significant volume expansion during the lithiation process (~96%) and poor electronic conductivity are the

key issues that prevent the practical implementation of α-Fe_2O_3 anodes [258]. The hollow α-Fe_2O_3 with spherical morphology has been synthesized using the citric acid-assisted HT synthetic method, and the core-shell α-Fe_2O_3@C may be formed after carbon coating via the annealing process [205]. The results demonstrate that the α-Fe_2O_3@C hollow spheres have a high reversible Li storage capacity as well as good cycling stability, with an initial discharge–charge specific capacity of 1377 mAh/g and 723 mAh/g at 1C, and a discharge specific capacity of 793.2 mAh/g after 600 cycles. Further, better rate performance is achieved: 997.8 mAh/g at 0.1 C, 943.8 mAh/g at 0.2 C, 829.2 mAh/g at 0.5 C, 764.8 mAh/g at 1 C, and 697.6 mAh/g at 2 C, with a capacity of 966.3 mAh/g recoverable when the current density returns to 0.1 C. The hollow structure of α-Fe_2O_3@C not only reduces volume change during cycling, but it also facilitates Li-ion and electron transport and helps to stabilize the SEI layer.

Because of its abundance, low oxidation potential, and competitive electrochemical performance, Mn_3O_4 has been thoroughly explored as one of the most promising anode materials [259]. However, a number of difficulties prevent the use of TMOs as anode materials in LIBs. It has been widely acknowledged that nano-engineering and carbon hybridization are effective methods to overcome or reduce these difficulties [260]. A solvothermal reaction was used to create a self-assembled manganese (Mn)-based metal organic complex (Mn-MOC) with a spherical structure [206]. Thermal annealing was used to transform the Mn-MOC precursor materials to hierarchical porous Mn_3O_4/C nanospheres. As an anode in LIBs, these nanospheres demonstrated high reversible specific capacity (1237 mAh/g at 200 mA/g), good ratability (425 mAh/g at 4 A/g), and extraordinarily extended cycle life (no substantial capacity decline after 3000 cycles at 4 A/g). The higher capacity of the Mn_3O_4/C nanospheres to store Li was facilitated by their unique porous hierarchical structure, which is composed of uniformly distributed Mn_3O_4 nanocrystals with thin carbon shells.

Considering the combined benefits of carbon and TMOs, Yu et al. used spray pyrolysis with cobalt nitrate and glucose as precursors to produce Co_3O_4-doped hollow hierarchical porous carbon spheres [207]. The wall thickness of hollow porous spheres can be altered by varying the cobalt nitrate–glucose ratio. The electrochemical test results show that the product has a discharge capacity of 1297.1 mAh/g after 200 cycles at 0.2 A/g when 6.8 is the molar ratio of glucose to cobalt nitrate. The sample has a discharge specific capacity of 841.0 mAh/g after 300 cycles at 1 A/g. The hollow hierarchical porous structure effectively reduces the path of Li-ion transport, and the appropriate wall thickness can accommodate volume changes during charge and discharge. Figure 14c clearly shows that the sample's charge and discharge ability is stable, with a coulombic efficiency of >98%. Trukawka et al. accomplished completely reversible conversion in hollow carbon spheres (HCSs) functionalized with copper oxide (Cu_2O) when tested as an anode material for LIBs [208]. HCSs were created using a hard template and glucose as a carbon precursor. Cu_2O was created by a thermally decomposing copper precursor. The uniform diameter of the spherical structure was ~160 nm and the shell thickness was ~10 nm. Cu_2O nanoparticles (~25 nm in diameter) are uniformly dispersed inside HCSs. The carbon structure between Cu_2O nanoparticles buffers the volume change and prevents Cu_2O nanoparticle aggregation. It also provides open channels for electron transport and Li^+ diffusion during charge and discharge processes. When compared to HCSs, HCSs with Cu_2O nanoparticles give an enhanced high specific capacity of 682 mAh/g at a current density of 50 mA/g and highly stable cycling capabilities even at higher current rates when used as anode material for LIBs.

Nitrogen-doped carbon-coated TiO_2 (TiO_2/N-C) demonstrated a reversible specific capacity of 277 mAh/g after 220 cycles at a current density of 0.6 C as an anode material for LIBs [209]. An acceptable rate capability was also obtained at various current densities. The elevated performance of the TiO_2/N-C was caused by the N-doped carbon and assembly structure, which might facilitate electrical conductivity and buffer volume expansion during the charge and discharge process. Furthermore, small nanoparticles can shorten the Li-ion

transportation path, and the gaps formed between connected small nanoparticles can accommodate volume change.

4.2. Porous Carbon-Based Anodes

Due to their high electronic conductivity, large surface area, tunable pore size and structure properties, chemical stability, and low cost, porous carbon materials are widely used in electrochemical energy storage, including LIBs, metal–air batteries, hydrogen-oxygen fuel cells, and supercapacitors (Figure 15a). Furthermore, porous carbons can be easily blended with active materials to create composites via sol–gel [261], ball-milling [262], grinding [263], melt-diffusion [264], sonochemical [265], and wet impregnation [266] methods. Vulcan XC-72 [267] and carbon black (super P) [268] are examples of porous conductive carbons. Industrially produced Vulcan XC-72R is known to have a surface area of ~250 m^2/g and high electric conductivity of ~2.77 S/cm [269]. Porous carbon allows for volume expansion while also providing rapid Li-ion diffusion and electron transportation paths through the 3D porous structure's channels (Figure 15b) [270]. In LIB, using solely porous carbon as an electrode results in mainly irreversible capacity loss during the first cycle due to electrolyte decomposition and SEI development on the large surface area.

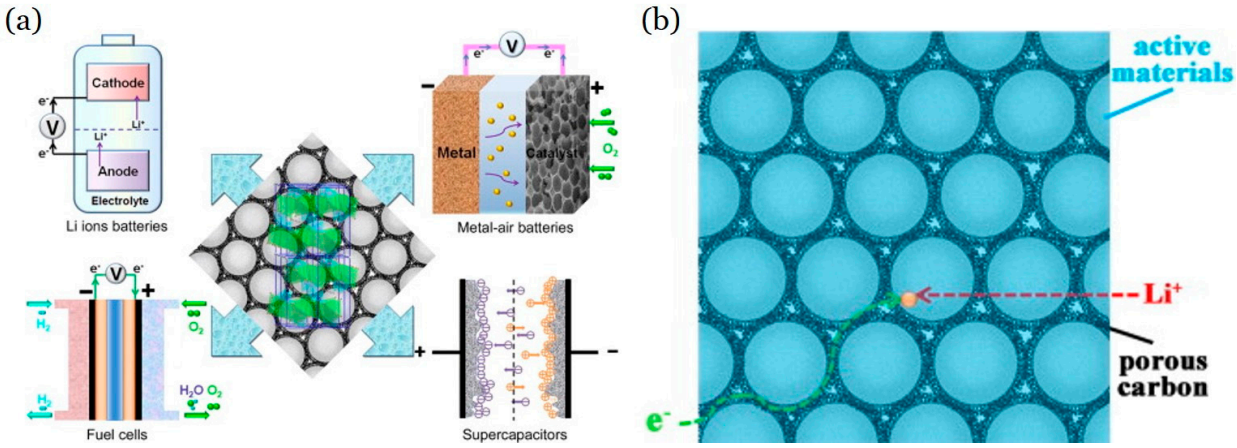

Figure 15. (**a**) Applications of porous carbons in the field of electrochemical energy conversion and storage (Li-ion batteries, metal–air batteries, fuel cells, and supercapacitors); (**b**) illustration of e^- and Li^+ transports in the composite electrode materials of porous carbons and inorganic compounds [271].

Template methods [272] and activation processes [273] are the most common methods used to fabricate porous carbons. The template approach, comprising a hard-template process and a soft-template process, has been used to create many types of porous carbon materials. The activation technique is typically used to produce microporous activated carbons.

Adding metal oxides to porous carbon anode material integrates well to enhance electrochemical performance of porous carbon anode materials: V_2O_3 [274], ZnO [275], MoO_2 [276], α-Fe_2O_3 [277], TiO_2 [278,279], SnO_2 [280], V_2O_3 [281], NiO [282,283], and Co_3O_4 [284]. Through the multiple-electron transfer procedure during the conversion reaction, they can address the enormous irreversible capacity issue [270].

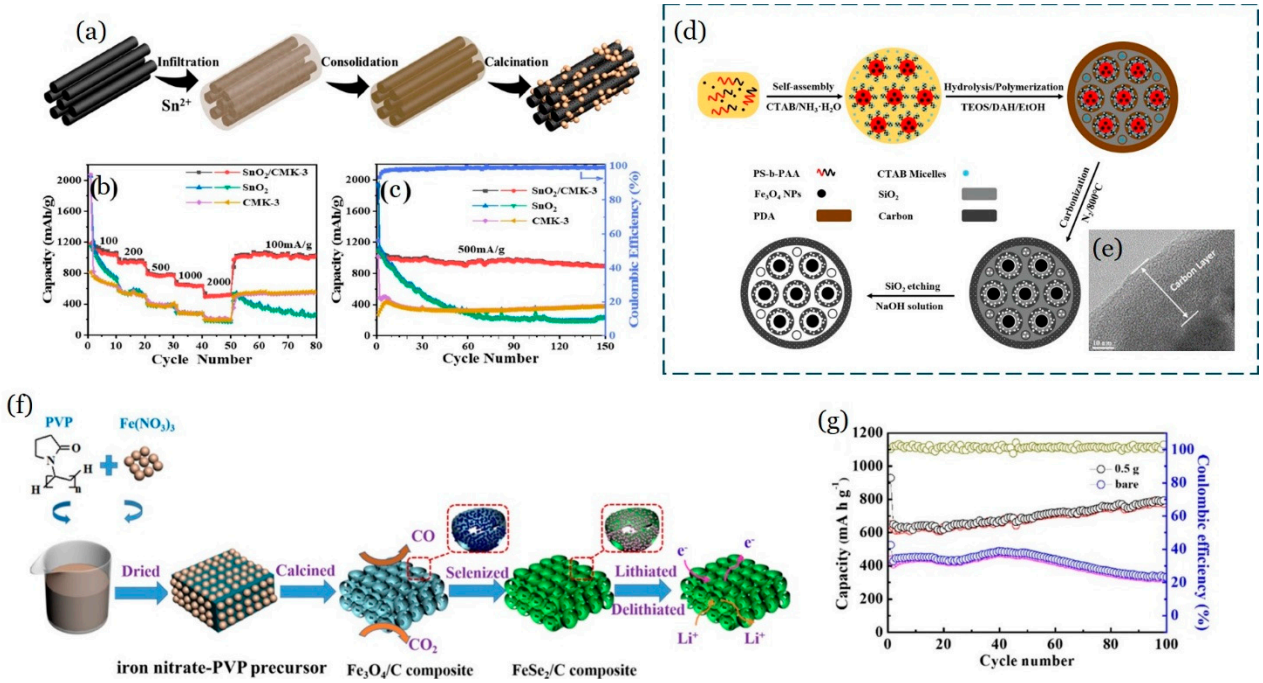

Figure 16. SnO_2, CMK-3, and SnO_2/CMK-3 electrodes. (**a**) Synthesis steps for SnO_2/CMK-3; (**b**) rate performances at different current densities; (**c**) cycle performances at 500 mA/g [280]. (**d**,**e**) Fe_3O_4@N-HPCNs. (**d**) Synthetic procedure of Fe_3O_4@N-HPCNs; (**e**) microporous carbon shell on Fe_3O_4@N-HPCNs [285]. (**f**,**g**) Three-dimensional porous $FeSe_2$/C composite: (**f**) illustration of synthesis of 3D Porous $FeSe_2$/C composite; (**g**) cycling performance and coulombic efficiency of 3D porous $FeSe_2$/C composite under the current density of 100 mA/g with 0.5 g PVP and the bare $FeSe_2$ for LIBs [286].

Li et al. produced SnO_2 nanodots (avg. size of ~5 nm) within the channels of the commercial ordered mesoporous carbon (CMK-3) [280]. The Sn precursor is prefilled under vacuum and easily transformed into SnO_2 by heating at 350 °C in air (Figure 16a). The SnO_2@CMK-3 composite demonstrates a discharge capacity of 898.8 mAh/g at the 150th cycle at 500 mA/g, surpassing that of the bare SnO_2 and CMK-3 electrodes (Figure 14b,c). This elevated electrochemical performance can be attributed to the high conductivity and large pore volume of the CMK-3 carbon matrices, which effectively reduce volume change-induced pulverization and increase electrode conductivity. Three-dimensional Si@TiO_2@C nanohybrids prepared using a three-step synthesis strategy outperformed Si@C and C (derived from polyaniline) electrodes in terms of electrochemical performance [287]. This was due to the existence of a robust TiO_2 shell and a polyaniline-derived porous carbon framework that can withstand volume changes of Si through lithiation and promote the overall electrode's electric conductivity. The homogeneous dispersion of Si nanoparticles in Si@TiO_2@C allowed for larger Li storage sites. The Si@TiO_2@C hybrid electrode has an initial discharge capacity of 1748.6 mAh/g at 100 mA/g, and a steady reversible capacity of 1112.5 mAh/g at 100 mA/g following 500 cycles, having a coulombic efficiency of 98.8%. The electrode demonstrated a high reversible capacity of 508.9 mAh/g at 500 mA/g during the 500th cycle, with a coulombic efficiency of 99.1%.

Fe_3O_4-based materials are regarded as a viable anode choice due to their nontoxicity, theoretical capacity of 924 mAh/g), and low cost [288–290]. However, pure Fe_3O_4 exhibits low conductivity and a substantial volume expansion problem (~200%) during lithiation, leading to poor rate performance and a rapid capacity decline [291]. As previously stated, N-doping is thought to be an effective approach for increasing the Li storage characteristics of carbonaceous materials. A soft-templating method was used to create Fe_3O_4 nanoparticle-embedded and N-doped hierarchically porous carbon nanospheres (Fe_3O_4@N-HPCNs) (Figure 16d) [285]. The nanospheres have a core-shell, hierarchical porous structure with dual mesoporous cores and microporous carbon shells (~30 nm thick, Figure 16e). The

Fe_3O_4@N-HPCNs anode has reversible specific capacities: 1240 mAh/g (after 100 cycles at 0.1 A/g) and 581 mAh/g (after 400 cycles at 1 A/g). Even at 10 A/g, the specific capacity remains around 290 mAh/g.

Xu et al. synthesized N-doped double-shelled hollow mesoporous carbon spheres (N-DHMCSs) using a simple soft-template technique involving self-assembly of amphiphilic anionic block copolymer polystyrene-*b*-poly(acrylic acid) (PS-*b*-PAA) micelles as the soft template, TEOS as the Si source, and dopamine (DA) as carbon and N sources [292]. After carbonizing the DA precursors and removing Si, the resulting N-DHMCSs had a large specific surface area (>600 m^2/g), tunable N doping content (4.02–5.91% in weight ratios), and double-shell hollow structures. The double-shelled carbon structures, hierarchical porous architecture, and appropriate N doping level not only reduce the diffusion channel length and conductivity, but also enhance active sites. When the current density is increased progressively from 0.1 A/g to 5 A/g, the N-DHMCSs (carbonized at 800 °C) had good rate capability. After 100 cycles (0.1 A/g), the same sample had a high discharge specific capacity of 920.3 mAh/g. Pappas et al. studied the performance of carbon nanospheres (CNSs) doped with three heteroatoms (N, P, and S) as LIB anode materials. The CNSs were formed by carbonizing strongly crosslinked organo (phosphazene) nanospheres (OPZs) with a diameter of 300 nm [293]. The OPZs were produced via a single polycondensation process involving hexachlorocyclotriphosphazene (HCCP) and 4,4′-sulphonyldiphenol. The CNS anode material contained micro- and mesopores, had a high specific surface area of 875 m^2/g, and demonstrated good stability and coulombic efficiency throughout a lengthy charge–discharge cycle of up to 1000 cycles at a 1C rate, generating approximately 130 mAh/g.

Melamine-formaldehyde resins are another commonly available and inexpensive potential carbon source [294,295]. To increase the graphitic N content, Sui et al. employed melamine-formaldehyde resin as both a crosslinking agent and a N source, and they created N-doped porous Gr materials via freeze-drying and thermally annealing a Gr/melamine-formaldehyde hydrogel [296]. The end product had a discharge capacity of 672 mAh/g when measured at a current density of 100 mA/g. Likewise, Si nanoparticles (Si NPs) were self-incorporated into melamine-formaldehyde resin microspheres using an HT approach. The precursors were then annealed to form hollow N-doped carbon microspheres (hNC MSs) with 10.8 wt% Si NPs [297]. Melamine was immediately polymerized with formaldehyde, giving N and carbon sources. After 360 cycles, the Si@hNC MS LIB anode maintained a reversible capacity of 872 mAh/g (at 200 mA/g). The hNC MSs significantly reduced the Si volumetric variations caused by repetitive charging and discharging, resulting in a high electrochemical stability of the Si anode [297].

A binder-free anode made of disordered carbon matrix, comprising meso- and macropores and nanosized sp^2-clusters (avg. size ~15–20 nm) prepared via the virtual cathode deposition technique showed specific capacity of ~1250 mAh/g for the first cycle and capacity of >900 mAh/g at a 0.1 C rate, and >600 mAh/g at a 0.5 A/g rate during cycling [298]. A coulombic efficiency > 99.5% was observed for 500 cycles. Further, the anode yielded areal capacity (~4.5 mAh/cm^2) and volumetric (>1400 Ah/L) capacities. The surface area was ~2100 m^2/g. The specific carbon matrix microstructure brought about by the process-induced polymorphism, together with its beneficial mechanical and electrical qualities, was the reason for the enhanced Li^+ intercalation.

Recently, metal selenides have been tested for their Li/Na storage properties because of their relatively high theoretical capacities and appropriate working potentials. These include $MoSe_2$ [299], $FeSe_x$ [300], Sb_2Se_3 [301], $CoSe_x$ [302], Cu_2Se [303], and $NiSe_2$ [304], Iron selenide has gained increased attention due to its extensive Fe resources, superior chemical stability, and high theoretical capacity [305]. However, considerable volume changes occur throughout the cycling process, resulting in structural degradation, and the creation of unstable SEI limits its widespread application. Nanocompositing iron selenides with carbon structures is a good option.

A 3D porous carbon framework embedded with $FeSe_2$ nanoparticles (3D porous $FeSe_2$/C composite) produced via a simple calcined method, following a selenized method without a template, shows reversible capacities of 798.4 and 455.0 mAh/g for LIBs and sodium-ion batteries, respectively, at 100 mA/g after 100 cycles (Figure 16f,g) [286]. The composite has better cycle stability than bare $FeSe_2$ nanoparticles. The uniformity of $FeSe_2$ nanoparticles, the 3D porous structure's accommodative volume stress upon cycling and shortening electron/ion transport paths, and increased conductivity due to carbon as a buffer matrix are the factors for enhanced electrochemical performance.

5. Summary, Challenges, and Outlook

This review examined the common LIB anode materials, including their conducting mechanisms, morphological characteristics, synthesis techniques, and energy storage capabilities. To improve the energy densities of LIBs, nanocarbon-based hybrids can be synthesized to harness the synergistic properties of both nanocarbons and high Li storage capacity materials. Certainly, such composite anode materials can greatly improve battery performance when compared to a single constituent.

In terms of dimensions, the 1D structure has a low density, strong mechanical strength, and outstanding conductivity, making it suitable for use as a conductive network and inhibiting volume expansion for LIB electrodes. Nevertheless, CNT-based anodes cannot be used as a replacement for graphite-based anodes in LIB anode applications because of their highly irreversible capacity and minor improvements in Li storage capacity and cyclability.

The number of defects, lengths, and diameters of CNTs determine the performance of CNT-based anode materials. The chemical etching and ball-milling treatments have been shown to cause structural modifications and the development of surface functional groups on CNTs. The structural alterations, such as lateral defects on the surface of CNTs and shortening of CNT lengths, can boost Li insertion capability. However, both chemical etching and mechanical ball-milling processes typically result in the degradation of graphitic structure, uneven size reduction with lengthy CNTs remaining, and a considerable loss of raw materials. As a result, new technologies must be devised to produce short CNTs with narrow length and breadth distributions and minimal material loss. The actual nature of CNTs, including the number and types of defects, CNT diameters, and lengths that aid in enhancing the anode performance, must be determined. The application of first-principles calculations to determine the electronic properties of CNT can help us in deciding the maximum intercalation density, information on where the intercalated ions sit, and whether the intercalation modifies the structure of the nanotube. The outcome of such calculations can help us choose the promising candidate material for anodes in battery applications without undergoing labor-intensive experimental etiquette. The simplification of nanocarbon synthesis techniques is a necessity for the production of large-scale, low-cost end products. Fabrication of a free-standing thick CNT paper for LIB anodes is critical since it allows for the design of LIB without a current collector and reduces the weight of the power source. Furthermore, the CNT paper's ease of handling allows it to be easily shaped into the various shapes required in a wide range of flexible and lightweight electronic devices. CNTs can be coupled with conducting polymers and high-capacity anode materials like transition oxide, Si, and Ge nanoparticles to create functional inks that can be used to print flexible paper-like electrodes using different printing technologies.

The 2D carbon material has strong physiochemistry, a huge surface area, and good electrical conductivity. It can be employed as a conductive layered structure and volume expansion restricting agent in the LIB anode. Gr offers excellent electronic conductivity, mechanical flexibility, and chemical activity. As a result, it can be used as an appropriate 2D support for assembling nanoparticles with diverse shapes, and excellent results have been produced using Gr–metal oxide nanoparticle composites. Furthermore, Gr can inhibit nanoparticle agglomeration during cycling, and nanoparticles can prevent Gr sheets from stacking again. The effect of defects in Gr on Li adsorption requires further investigation. In such efforts, computational tools can be employed. Graphene functionalized with

heteroatoms and different functional groups can attract Li-ions and improve their energy storage capacity. Multidimensional structures on highly conductive carbon nanomaterials with abundant electroactive sites and high SSA contribute to LIBs' excellent capacitance and cycle performance.

Hybrid materials comprised of 3D carbon nanostructure and transition-metal oxides, carbonate, sulfides, Si, Ge, etc., for LIB anodes have particular characteristics: the porous hierarchical hollow designs enable substantially shorter transport channels for electrolyte ions and electrons, resulting in faster electrode kinetics. The hollow carbon sphere frameworks provide increased electrical conductivity and structural integrity, resulting in accelerated performance and long cycling stability. Three-dimensional structures, particularly porous, hollow, and core-shell spheres, can withstand significant volumetric fluctuations during the charge–discharge process but reduce the volumetric capacity of the whole structure. Despite notable advances, the difficulties connected with their synthesis, dimensional control, and large electrode–electrolyte surface area, which produces the high irreversible capacity, have hampered their widespread use in LIBs. Computational and experimental research is needed to understand the interrelationships between the structural and chemical properties of 3D nanocarbon-based anodes and LIB performance. Density functional theory-based first-principles calculations can be used to predict de-lithiated and lithiated phases, charge distribution, phase stability and transition, and Li-ion diffusion kinetics. The self-templating method, together with Ostwald ripening and the Kirkendall effect, offers a novel approach to creating nanohybrids from hollow carbon spheres. The fabrication of porous carbon materials using metal–organic frameworks as templates and biomass as a sustainable carbon precursor is highly promising.

Small-scale production of high-performance anode materials might be simple in research labs. Real commercial-scale synthesis, however, can be quite challenging and needs complex techniques. The HT method under different temperatures and duration followed by calcination (annealing) is a widely employed technique to synthesize nanocarbon hybrids. However, the HT technique needs very stringent reaction conditions. Such strategies demand preliminary investigations to comprehend the suitable HT reaction parameters. The modified Hummers process is the most popular way used to prepare graphene. However, it involves numerous processes, employs hazardous reactants, and produces heavy metal ions and other hazardous materials. Mechanical exfoliation and chemical vapor deposition, on the other hand, have limited yields and are expensive to undertake. As a result, novel strategies are required to produce large-area graphene in a simple, environmentally friendly, and cost-effective manner on a large scale.

The low ICE of intercalation-type active anode materials is due to the creation of the SEI layer and the irreversible nature of Li adsorption. The poor ICE of alloying-type materials is associated with the formation of the SEI layer, the imperfect reversible reaction caused by the coarsening of active materials, and the irreversible breakdown of certain oxides. As a result, SEI formation continues to be a significant concern. The material qualities and composition of the SEI layer therefore require additional investigation.

MXenes and Xenes, two emerging 2D materials, deserve further attention as anodes due to their high conductivity, adjustable layer distance, and highly exposed active sites. Similarly, transition-metal dichalcogenides have a graphene-like layered structure, and a single layer can be made via the stripping process. This arrangement can aid in the transport of Li ions, and the loosely layered structure can also reduce volume expansion during charging and discharge. It is worth noting that most 2D layered materials may be produced via the mechanical stripping method, although this method is inefficient and cannot produce large-area materials.

The cycling characterization must be performed at a high cycle number since Li-ion batteries are intended for long-term use. Microwave-assisted synthesis and modification of nanocarbons are fast and energy-efficient. Since nanocarbons are good microwave absorbers, this property can be used to functionalize various types of nanocarbons.

Funding: This research received no external funding.

Data Availability Statement: Not applicable.

Acknowledgments: This research was performed during an appointment at the Ames Laboratory, which is operated for the U.S. DOE by Iowa State University.

Conflicts of Interest: The author declares no conflicts of interest.

References

1. Lee, Y.; Blaauw, D.; Sylvester, D. Ultralow power circuit design for wireless sensor nodes for structural health monitoring. *Proc. IEEE* **2016**, *104*, 1529–1546. [CrossRef]
2. Rawat, P.; Singh, K.D.; Chaouchi, H.; Bonnin, J.M. Wireless sensor networks: A survey on recent developments and potential synergies. *J. Supercomput.* **2014**, *68*, 1–48. [CrossRef]
3. Jeong, S.; Foo, Z.; Lee, Y.; Sim, J.-Y.; Blaauw, D.; Sylvester, D. A fully-integrated 71 nW CMOS temperature sensor for low power wireless sensor nodes. *IEEE J. Solid-State Circuits* **2014**, *49*, 1682–1693. [CrossRef]
4. Gaikwad, A.M.; Arias, A.C.; Steingart, D.A. Recent progress on printed flexible batteries: Mechanical challenges, printing technologies, and future prospects. *Energy Technol.* **2015**, *3*, 305–328. [CrossRef]
5. Zamarayeva, A.M.; Gaikwad, A.M.; Deckman, I.; Wang, M.; Khau, B.; Steingart, D.A.; Arias, A.C. Fabrication of a High-Performance Flexible Silver–Zinc Wire Battery. *Adv. Electron. Mater.* **2016**, *2*, 1500296. [CrossRef]
6. Qi, W.; Shapter, J.G.; Wu, Q.; Yin, T.; Gao, G.; Cui, D. Nanostructured anode materials for lithium-ion batteries: Principle, recent progress and future perspectives. *J. Mater. Chem. A* **2017**, *5*, 19521–19540. [CrossRef]
7. Chen, J.; Cheng, F. Combination of lightweight elements and nanostructured materials for batteries. *Acc. Chem. Res.* **2009**, *42*, 713–723. [CrossRef]
8. Kaskhedikar, N.A.; Maier, J. Lithium storage in carbon nanostructures. *Adv. Mater.* **2009**, *21*, 2664–2680. [CrossRef]
9. Yang, Z.; Zhang, J.; Kintner-Meyer, M.C.W.; Lu, X.; Choi, D.; Lemmon, J.P.; Liu, J. Electrochemical energy storage for green grid. *Chem. Rev.* **2011**, *111*, 3577–3613. [CrossRef]
10. Jiang, J.; Li, Y.; Liu, J.; Huang, X.; Yuan, C.; Lou, X.W. Recent advances in metal oxide-based electrode architecture design for electrochemical energy storage. *Adv. Mater.* **2012**, *24*, 5166–5180. [CrossRef]
11. Li, Y.; Wu, J.; Chopra, N. Nano-carbon-based hybrids and heterostructures: Progress in growth and application for lithium-ion batteries. *J. Mater. Sci.* **2015**, *50*, 7843–7865. [CrossRef]
12. Wang, G.; Shen, X.; Yao, J.; Park, J. Graphene nanosheets for enhanced lithium storage in lithium ion batteries. *Carbon* **2009**, *47*, 2049–2053. [CrossRef]
13. Chen, S.; Bao, P.; Xiao, L.; Wang, G. Large-scale and low cost synthesis of graphene as high capacity anode materials for lithium-ion batteries. *Carbon* **2013**, *64*, 158–169. [CrossRef]
14. Zhang, H.; Sun, X.; Zhang, X.; Lin, H.; Wang, K.; Ma, Y. High-capacity nanocarbon anodes for lithium-ion batteries. *J. Alloys Compd.* **2015**, *622*, 783–788. [CrossRef]
15. Roselin, L.S.; Juang, R.-S.; Hsieh, C.-T.; Sagadevan, S.; Umar, A.; Selvin, R.; Hegazy, H.H. Recent advances and perspectives of carbon-based nanostructures as anode materials for Li-ion batteries. *Materials* **2019**, *12*, 1229. [CrossRef]
16. Hu, Y.S.; Adelhelm, P.; Smarsly, B.M.; Hore, S.; Antonietti, M.; Maier, J. Synthesis of hierarchically porous carbon monoliths with highly ordered microstructure and their application in rechargeable lithium batteries with high-rate capability. *Adv. Funct. Mater.* **2007**, *17*, 1873–1878. [CrossRef]
17. Zhou, L.; Zhang, K.; Hu, Z.; Tao, Z.; Mai, L.; Kang, Y.M.; Chou, S.L.; Chen, J. Recent developments on and prospects for electrode materials with hierarchical structures for lithium-ion batteries. *Adv. Energy Mater.* **2018**, *8*, 1701415. [CrossRef]
18. Owen, J.R. Rechargeable lithium batteries. *Chem. Soc. Rev.* **1997**, *26*, 259–267. [CrossRef]
19. Deng, D. Li-ion batteries: Basics, progress, and challenges. *Energy Sci. Eng.* **2015**, *3*, 385–418. [CrossRef]
20. Li, X.; Sun, X.; Hu, X.; Fan, F.; Cai, S.; Zheng, C.; Stucky, G.D. Review on comprehending and enhancing the initial Coulombic efficiency of anode materials in lithium-ion/sodium-ion batteries. *Nano Energy* **2020**, *77*, 105143. [CrossRef]
21. Landi, B.J.; Ganter, M.J.; Cress, C.D.; DiLeo, R.A.; Raffaelle, R.P. Carbon nanotubes for lithium ion batteries. *Energy Environ. Sci.* **2009**, *2*, 638–654. [CrossRef]
22. Thess, A.; Lee, R.; Nikolaev, P.; Dai, H.; Petit, P.; Robert, J.; Xu, C.; Lee, Y.H.; Kim, S.G.; Rinzler, A.G. Crystalline ropes of metallic carbon nanotubes. *Science* **1996**, *273*, 483–487. [CrossRef] [PubMed]
23. Yu, M.F.; Lourie, O.; Dyer, M.J.; Moloni, K.; Kelly, T.F.; Ruoff, R.S. Strength and breaking mechanism of multiwalled carbon nanotubes under tensile load. *Science* **2000**, *287*, 637–640. [CrossRef] [PubMed]
24. De las Casas, C.; Li, W. A review of application of carbon nanotubes for lithium ion battery anode material. *J. Power Sources* **2012**, *208*, 74–85. [CrossRef]
25. Xiong, Z.; Yun, Y.S.; Jin, H.-J. Applications of carbon nanotubes for lithium ion battery anodes. *Materials* **2013**, *6*, 1138–1158. [CrossRef]
26. Yang, S.; Huo, J.; Song, H.; Chen, X. A comparative study of electrochemical properties of two kinds of carbon nanotubes as anode materials for lithium ion batteries. *Electrochim. Acta* **2008**, *53*, 2238–2244. [CrossRef]

27. Yang, Z.H.; Wu, H.Q. Electrochemical intercalation of lithium into raw carbon nanotubes. *Mater. Chem. Phys.* **2001**, *71*, 7–11. [CrossRef]
28. Senami, M.; Ikeda, Y.; Fukushima, A.; Tachibana, A. Theoretical study of adsorption of lithium atom on carbon nanotube. *AIP Adv.* **2011**, *1*, 042106. [CrossRef]
29. Shimoda, H.; Gao, B.; Tang, X.P.; Kleinhammes, A.; Fleming, L.; Wu, Y.; Zhou, O. Lithium intercalation into opened single-wall carbon nanotubes: Storage capacity and electronic properties. *Phys. Rev. Lett.* **2001**, *88*, 015502. [CrossRef]
30. Liu, Y.; Yukawa, H.; Morinaga, M. First-principles study on lithium absorption in carbon nanotubes. *Comput. Mater. Sci.* **2004**, *30*, 50–56. [CrossRef]
31. Song, B.; Yang, J.; Zhao, J.; Fang, H. Intercalation and diffusion of lithium ions in a carbon nanotube bundle by ab initio molecular dynamics simulations. *Energy Environ. Sci.* **2011**, *4*, 1379–1384. [CrossRef]
32. Klink, S.; Ventosa, E.; Xia, W.; La Mantia, F.; Muhler, M.; Schuhmann, W. Tailoring of CNT surface oxygen groups by gas-phase oxidation and its implications for lithium ion batteries. *Electrochem. Commun.* **2012**, *15*, 10–13. [CrossRef]
33. Zhao, M.; Xia, Y.; Liu, X.; Tan, Z.; Huang, B.; Li, F.; Ji, Y.; Song, C. Curvature-induced condensation of lithium confined inside single-walled carbon nanotubes: First-principles calculations. *Phys. Lett. A* **2005**, *340*, 434–439. [CrossRef]
34. Li, J.; Wu, C.; Guan, L. Lithium insertion/extraction properties of nanocarbon materials. *J. Phys. Chem. C* **2009**, *113*, 18431–18435. [CrossRef]
35. Ji, L.; Zhang, X. Evaluation of Si/carbon composite nanofiber-based insertion anodes for new-generation rechargeable lithium-ion batteries. *Energy Environ. Sci.* **2010**, *3*, 124–129. [CrossRef]
36. Huyan, Y.; Wang, J.; Chen, J.; Zhang, Q.; Zhang, B. Magnetic tubular carbon nanofibers as anode electrodes for high-performance lithium-ion batteries. *Int. J. Energy Res.* **2019**, *43*, 8242–8256. [CrossRef]
37. Zhu, G.; Gu, Y.; Wang, Y.; Qu, Q.; Zheng, H. Neuron like Si-carbon nanotubes composite as a high-rate anode of lithium ion batteries. *J. Alloys Compd.* **2019**, *787*, 928–934. [CrossRef]
38. Li, S.; Chen, C.; Fu, K.; Xue, L.; Zhao, C.; Zhang, S.; Hu, Y.; Zhou, L.; Zhang, X. Comparison of Si/C, Ge/C and Sn/C composite nanofiber anodes used in advanced lithium-ion batteries. *Solid State Ion.* **2014**, *254*, 17–26. [CrossRef]
39. Wu, M.; Wang, C.; Chen, J.; Wang, F.; Yi, B. Sn/carbon nanotube composite anode with improved cycle performance for lithium-ion battery. *Ionics* **2013**, *19*, 1341–1347. [CrossRef]
40. Du, G.; Zhong, C.; Zhang, P.; Guo, Z.; Chen, Z.; Liu, H. Tin dioxide/carbon nanotube composites with high uniform SnO_2 loading as anode materials for lithium ion batteries. *Electrochim. Acta* **2010**, *55*, 2582–2586. [CrossRef]
41. Si, Q.; Hanai, K.; Ichikawa, T.; Hirano, A.; Imanishi, N.; Yamamoto, O.; Takeda, Y. High performance Si/C@CNF composite anode for solid-polymer lithium-ion batteries. *J. Power Sources* **2011**, *196*, 6982–6986. [CrossRef]
42. Ren, Y.R.; Qu, M.Z.; Yu, Z.L. SiO/CNTs: A new anode composition for lithium-ion battery. *Sci. China Ser. B Chem.* **2009**, *52*, 2047–2050. [CrossRef]
43. Dirican, M.; Lu, Y.; Fu, K.; Kizil, H.; Zhang, X. SiO_2-confined silicon/carbon nanofiber composites as an anode for lithium-ion batteries. *RSC Adv.* **2015**, *5*, 34744–34751. [CrossRef]
44. Wang, H.; Gao, P.; Lu, S.; Liu, H.; Yang, G.; Pinto, J.; Jiang, X. The effect of tin content to the morphology of Sn/carbon nanofiber and the electrochemical performance as anode material for lithium batteries. *Electrochim. Acta* **2011**, *58*, 44–51. [CrossRef]
45. Hu, Y.; Yang, Q.R.; Ma, J.; Chou, S.L.; Zhu, M.; Li, Y. Sn/SnO_2@C composite nanofibers as advanced anode for lithium-ion batteries. *Electrochim. Acta* **2015**, *186*, 271–276. [CrossRef]
46. Fu, Z.; Li, X.; Xu, G. Novel electrospun SnO_2@carbon nanofibers as high performance anodes for lithium-ion batteries. *Cryst. Res. Technol.* **2014**, *49*, 441–445. [CrossRef]
47. Wu, C.; Li, X.; Li, W.; Li, B.; Wang, Y.; Wang, Y.; Xu, M.; Xing, L. Fe_2O_3 nanorods/carbon nanofibers composite: Preparation and performance as anode of high rate lithium ion battery. *J. Power Sources* **2014**, *251*, 85–91. [CrossRef]
48. He, X.; Hu, Y.; Shen, Z.; Chen, R.; Wu, K.; Cheng, Z.; Zhang, X.W.; Pan, P. Channelized carbon nanofiber with uniform-dispersed GeO_2 as anode for long-lifespan lithium-ion batteries. *J. Alloys Compd.* **2017**, *729*, 313–322. [CrossRef]
49. Fang, Z.; Xu, W.; Huang, T.; Li, M.; Wang, W.; Liu, Y.; Mao, C.; Meng, F.; Wang, M.; Cheng, M. Facile scalable synthesis of Co_3O_4/carbon nanotube hybrids as superior anode materials for lithium-ion batteries. *Mater. Res. Bull.* **2013**, *48*, 4419–4423. [CrossRef]
50. Zhao, M.; Liu, Y.; Jiang, J.; Ma, C.; Yang, G.; Yin, F.; Yang, Y. Sheath/core hybrid $FeCO_3$/carbon nanofibers as anode materials for superior cycling stability and rate performance. *ChemElectroChem* **2017**, *4*, 1450–1456. [CrossRef]
51. Qin, L.; Liang, S.; Pan, A.; Tan, X. Zn_2SnO_4/carbon nanotubes composite with enhanced electrochemical performance as anode materials for lithium-ion batteries. *Mater. Lett.* **2016**, *164*, 44–47. [CrossRef]
52. Joshi, B.; Samuel, E.; Kim, M.W.; Park, S.; Swihart, M.T.; Yoon, W.Y.; Yoon, S.S. Atomic-layer-deposited TiO_2-SnZnO/carbon nanofiber composite as a highly stable, flexible and freestanding anode material for lithium-ion batteries. *Chem. Eng. J.* **2018**, *338*, 72–81. [CrossRef]
53. Li, F.; Liu, W.; Li, K.; Chen, W.; Xu, D.; Yu, X.; Hu, H. One step synthesis of $FeCO_3$ nanorods interwind with carbon nanotubes as anode materials for lithium-ion batteries. *J. Electroanal. Chem.* **2018**, *824*, 67–74. [CrossRef]
54. Narsimulu, D.; Rao, B.N.; Satyanarayana, N.; Srinadhu, E.S. High capacity electrospun $MgFe_2O_4$–C composite nanofibers as an anode material for lithium ion batteries. *Chem. Sel.* **2018**, *3*, 8010–8017. [CrossRef]

55. Cao, K.; Jia, Y.; Wang, S.; Huang, K.J.; Liu, H. Mn_3O_4 nanoparticles anchored on carbon nanotubes as anode material with enhanced lithium storage. *J. Alloys Compd.* **2021**, *854*, 157179. [CrossRef]
56. Velasquez, C.A.; Vasquez, F.; Alvarez-Lainez, M.; Zapata-Gonzalez, A.; Calderon, J.A. Carbon nanofibers impregnated with Fe_3O_4 nanoparticles as a flexible and high capacity negative electrode for lithium-ion batteries. *J. Alloys Compd.* **2021**, *862*, 158045. [CrossRef]
57. Huyan, Y.; Chen, J.; Yang, K.; Zhang, Q.; Zhang, B. Tailoring carboxyl tubular carbon nanofibers/MnO_2 composites for high-performance lithium-ion battery anodes. *J. Am. Ceram. Soc.* **2021**, *104*, 1402–1414. [CrossRef]
58. Rana, M.; Avvaru, V.S.; Boaretto, N.; Marcilla, R.; Etacheri, V.; Vilatela, J.J. High rate hybrid MnO_2@ CNT fabric anodes for Li-ion batteries: Properties and a lithium storage mechanism study by in situ synchrotron X-ray scattering. *J. Mater. Chem. A* **2019**, *7*, 26596–26606. [CrossRef]
59. Zhang, X.; Zhou, Y.; Mao, Y.; Wei, M.; Chu, W.; Huang, K. Rapid synthesis of ultrafine $NiCo_2O_4$ nanoparticles loaded carbon nanotubes for lithium ion battery anode materials. *Chem. Phys. Lett.* **2019**, *715*, 278–283. [CrossRef]
60. Wang, J.G.; Yang, Y.; Huang, Z.H.; Kang, F. MnO-carbon hybrid nanofiber composites as superior anode materials for lithium-ion batteries. *Electrochim. Acta* **2015**, *170*, 164–170. [CrossRef]
61. Jhan, Y.R.; Duh, J.G.; Yang, M.H.; Shieh, D.T. Electroless-plated tin compounds on carbonaceous mixture as anode for lithium-ion battery. *J. Power Sources* **2009**, *193*, 810–815. [CrossRef]
62. Cui, L.-F.; Yang, Y.; Hsu, C.-M.; Cui, Y. Carbon− silicon core− shell nanowires as high capacity electrode for lithium ion batteries. *Nano Lett.* **2009**, *9*, 3370–3374. [CrossRef] [PubMed]
63. Gao, S.; Wang, N.; Li, S.; Li, D.; Cui, Z.; Yue, G.; Liu, J.; Zhao, X.; Jiang, L.; Zhao, Y. A multi-wall Sn/SnO_2@carbon hollow nanofiber anode material for high-rate and long-life lithium-ion batteries. *Angew. Chem. Int. Ed.* **2020**, *59*, 2465–2472. [CrossRef] [PubMed]
64. Chan, C.K.; Peng, H.; Liu, G.; McIlwrath, K.; Zhang, X.F.; Huggins, R.A.; Cui, Y. High-performance lithium battery anodes using silicon nanowires. *Nat. Nanotechnol.* **2008**, *3*, 31–35. [CrossRef]
65. Fu, J.; Liu, H.; Liao, L.; Fan, P.; Wang, Z.; Wu, Y.; Zhang, Z.; Hai, Y.; Lv, G.; Mei, L. Ultrathin Si/CNTs paper-like composite for flexible Li-ion battery anode with high volumetric capacity. *Front. Chem.* **2018**, *6*, 624. [CrossRef]
66. Xue, L.; Xu, G.; Li, Y.; Li, S.; Fu, K.; Shi, Q.; Zhang, X. Carbon-coated Si nanoparticles dispersed in carbon nanotube networks as anode material for lithium-ion batteries. *ACS Appl. Mater. Interfaces* **2013**, *5*, 21–25. [CrossRef]
67. Zhou, C.; Zhang, Y.; Li, Y.; Liu, J. Construction of high-capacitance 3D CoO@ polypyrrole nanowire array electrode for aqueous asymmetric supercapacitor. *Nano Lett.* **2013**, *13*, 2078–2085. [CrossRef]
68. Kasavajjula, U.; Wang, C.; Appleby, A.J. Nano-and bulk-silicon-based insertion anodes for lithium-ion secondary cells. *J. Power Sources* **2007**, *163*, 1003–1039. [CrossRef]
69. Graetz, J.; Ahn, C.C.; Yazami, R.; Fultz, B. Nanocrystalline and thin film germanium electrodes with high lithium capacity and high rate capabilities. *J. Electrochem. Soc.* **2004**, *151*, A698. [CrossRef]
70. Veeraraghavan, B.; Durairajan, A.; Haran, B.; Popov, B.; Guidotti, R. Study of Sn-coated graphite as anode material for secondary lithium-ion batteries. *J. Electrochem. Soc.* **2002**, *149*, A675. [CrossRef]
71. Ji, L.; Jung, K.H.; Medford, A.J.; Zhang, X. Electrospun polyacrylonitrile fibers with dispersed Si nanoparticles and their electrochemical behaviors after carbonization. *J. Mater. Chem.* **2009**, *19*, 4992–4997. [CrossRef]
72. Ji, L.; Lin, Z.; Alcoutlabi, M.; Zhang, X. Recent developments in nanostructured anode materials for rechargeable lithium-ion batteries. *Energy Environ. Sci.* **2011**, *4*, 2682–2699. [CrossRef]
73. Zhu, Y.; Cao, C.; Zhang, J.; Xu, X. Two-dimensional ultrathin $ZnCo_2O_4$ nanosheets: General formation and lithium storage application. *J. Mater. Chem. A* **2015**, *3*, 9556–9564. [CrossRef]
74. Wang, C.; Zhang, X.; Zhang, D.; Yao, C.; Ma, Y. Facile and low-cost fabrication of nanostructured $NiCo_2O_4$ spinel with high specific capacitance and excellent cycle stability. *Electrochim. Acta* **2012**, *63*, 220–227. [CrossRef]
75. Yang, S.; Sun, Y.; Chen, L.; Hernandez, Y.; Feng, X.; Mullen, K. Porous iron oxide ribbons grown on graphene for high-performance lithium storage. *Sci. Rep.* **2012**, *2*, 427. [CrossRef]
76. Cai, F.; Kang, Y.; Chen, H.; Chen, M.; Li, Q. Hierarchical CNT@$NiCo_2O_4$ core–shell hybrid nanostructure for high-performance supercapacitors. *J. Mater. Chem. A* **2014**, *2*, 11509–11515. [CrossRef]
77. Taylor-Pashow, K.M.L.; Della Rocca, J.; Xie, Z.; Tran, S.; Lin, W. Postsynthetic modifications of iron-carboxylate nanoscale metal− organic frameworks for imaging and drug delivery. *J. Am. Ceram. Soc.* **2009**, *131*, 14261–14263. [CrossRef]
78. Nandihalli, N.; Gregory, D.H.; Mori, T. Energy-Saving Pathways for Thermoelectric Nanomaterial Synthesis: Hydrothermal/Solvothermal, Microwave-Assisted, Solution-Based, and Powder Processing. *Adv. Sci.* **2022**, *9*, 2106052. [CrossRef]
79. Li, J.; Wei, M.; Chu, W.; Wang, N. High-stable α-phase NiCo double hydroxide microspheres via microwave synthesis for supercapacitor electrode materials. *Chem. Eng. J.* **2017**, *316*, 277–287. [CrossRef]
80. Tzeng, Y.; Chen, R.; He, J.L. Silicon-based anode of lithium ion battery made of nano silicon flakes partially encapsulated by silicon dioxide. *Nanomaterials* **2020**, *10*, 2467. [CrossRef]
81. Bai, J.; Xi, B.; Mao, H.; Lin, Y.; Ma, X.; Feng, J.; Xiong, S. One-step construction of N, P-codoped porous carbon sheets/CoP hybrids with enhanced lithium and potassium storage. *Adv. Mater.* **2018**, *30*, 1802310. [CrossRef] [PubMed]
82. Pan, Z.; Ren, J.; Guan, G.; Fang, X.; Wang, B.; Doo, S.G.; Son, I.H.; Huang, X.; Peng, H. Synthesizing Nitrogen-Doped Core-Sheath Carbon Nanotube Films for Flexible Lithium Ion Batteries. *Adv. Energy Mater.* **2016**, *6*, 1600271. [CrossRef]

83. Xu, Y.; Zhang, C.; Zhou, M.; Fu, Q.; Zhao, C.; Wu, M.; Lei, Y. Highly nitrogen doped carbon nanofibers with superior rate capability and cyclability for potassium ion batteries. *Nat. Commun.* **2018**, *9*, 1720. [CrossRef]
84. Luan, Y.; Hu, R.; Fang, Y.; Zhu, K.; Cheng, K.; Yan, J.; Ye, K.; Wang, G.; Cao, D. Nitrogen and phosphorus dual-doped multilayer graphene as universal anode for full carbon-based lithium and potassium ion capacitors. *Nano-Micro Lett.* **2019**, *11*, 1–13. [CrossRef]
85. Niu, J.; Liang, J.; Shao, R.; Liu, M.; Dou, M.; Li, Z.; Huang, Y.; Wang, F. Tremella-like N, O-codoped hierarchically porous carbon nanosheets as high-performance anode materials for high energy and ultrafast Na-ion capacitors. *Nano Energy* **2017**, *41*, 285–292. [CrossRef]
86. Chen, M.; Cao, Y.; Ma, C.; Yang, H. AN/S/O-tridoped hard carbon network anode from mercaptan/polyurethane-acrylate resin for potassium-ion batteries. *Nano Energy* **2021**, *81*, 105640. [CrossRef]
87. Cao, M.; Jin, X.; Zhao, J.; Wang, X. Triggering hollow carbon nanotubes via dual doping for fast pseudocapacitive potassium-ion storage. *Appl. Mater. Today* **2023**, *30*, 101694. [CrossRef]
88. Ren, B.; Li, W.; Wei, A.; Bai, X.; Zhang, L.; Liu, Z. Boron and nitrogen co-doped CNT/$Li_4Ti_5O_{12}$ composite for the improved high-rate electrochemical performance of lithium-ion batteries. *J. Alloys Compd.* **2018**, *740*, 784–789. [CrossRef]
89. Zhang, J.; Nie, N.; Liu, Y.; Wang, J.; Yu, F.; Gu, J.; Li, W. Boron and nitrogen codoped carbon layers of $LiFePO_4$ improve the high-rate electrochemical performance for lithium ion batteries. *ACS Appl. Mater. Interfaces* **2015**, *7*, 20134–20143. [CrossRef]
90. Hou, T.; Liu, B.; Sun, X.; Fan, A.; Xu, Z.; Cai, S.; Zheng, C.; Yu, G.; Tricoli, A. Covalent coupling-stabilized transition-metal sulfide/carbon nanotube composites for lithium/sodium-ion batteries. *ACS Nano* **2021**, *15*, 6735–6746. [CrossRef]
91. Raccichini, R.; Varzi, A.; Passerini, S.; Scrosati, B. The role of graphene for electrochemical energy storage. *Nat. Mater.* **2015**, *14*, 271–279. [CrossRef] [PubMed]
92. Zhang, L.; Zhao, K.; Yu, R.; Yan, M.; Xu, W.; Dong, Y.; Ren, W.; Xu, X.; Tang, C.; Mai, L. Phosphorus enhanced intermolecular interactions of SnO2 and graphene as an ultrastable lithium battery anode. *Small* **2017**, *13*, 1603973. [CrossRef]
93. Wu, Q.; Jiang, R.; Liu, H. Carbon layer encapsulated Fe_3O_4@Reduced graphene oxide lithium battery anodes with long cycle performance. *Ceram. Int.* **2020**, *46*, 12732–12739. [CrossRef]
94. Xiong, P.; Zhu, J.; Zhang, L.; Wang, X. Recent advances in graphene-based hybrid nanostructures for electrochemical energy storage. *Nanoscale Horiz.* **2016**, *1*, 340–374. [CrossRef] [PubMed]
95. Fan, X.; Zheng, W.T.; Kuo, J.L. Adsorption and diffusion of Li on pristine and defective graphene. *ACS Appl. Mater. Interfaces* **2012**, *4*, 2432–2438. [CrossRef] [PubMed]
96. Hou, J.; Shao, Y.; Ellis, M.W.; Moore, R.B.; Yi, B. Graphene-based electrochemical energy conversion and storage: Fuel cells, supercapacitors and lithium ion batteries. *Phys. Chem. Chem. Phys.* **2011**, *13*, 15384–15402. [CrossRef]
97. Kim, H.; Kim, S.W.; Park, Y.U.; Gwon, H.; Seo, D.H.; Kim, Y.; Kang, K. SnO_2/graphene composite with high lithium storage capability for lithium rechargeable batteries. *Nano Res.* **2010**, *3*, 813–821. [CrossRef]
98. Tan, Q.; Kong, Z.; Chen, X.; Zhang, L.; Hu, X.; Mu, M.; Sun, H.; Shao, X.; Guan, X.; Gao, M. Synthesis of SnO_2/graphene composite anode materials for lithium-ion batteries. *Appl. Surf. Sci.* **2019**, *485*, 314–322. [CrossRef]
99. Tao, H.; Zhu, S.; Xiong, L.; Yang, X.; Zhang, L. Three-Dimensional Carbon-Coated SnO_2/Reduced Graphene Oxide Foam as a Binder-Free Anode for High-Performance Lithium-Ion Batteries. *ChemElectroChem* **2016**, *3*, 1063–1071. [CrossRef]
100. Liang, B.; Wang, J.; Zhang, S.; Liang, X.; Huang, H.; Huang, D.; Zhou, W.; Guo, J. Hybrid of Co-doped SnO_2 and graphene sheets as anode material with enhanced lithium storage properties. *Appl. Surf. Sci.* **2020**, *533*, 147447. [CrossRef]
101. Gao, C.; Jiang, Z.; Wang, P.; Jensen, L.R.; Zhang, Y.; Yue, Y. Optimized assembling of MOF/SnO_2/Graphene leads to superior anode for lithium ion batteries. *Nano Energy* **2020**, *74*, 104868. [CrossRef]
102. Xia, G.; Li, N.; Li, D.; Liu, R.; Wang, C.; Li, Q.; Lü, X.; Spendelow, J.S.; Zhang, J.; Wu, G. Graphene/Fe_2O_3/SnO_2 ternary nanocomposites as a high-performance anode for lithium ion batteries. *ACS Appl. Mater. Interfaces* **2013**, *5*, 8607–8614. [CrossRef] [PubMed]
103. Shen, H.; Xia, X.; Yan, S.; Jiao, X.; Sun, D.; Lei, W.; Hao, Q. SnO_2/$NiFe_2O_4$/graphene nanocomposites as anode materials for lithium ion batteries. *J. Alloys Compd.* **2021**, *853*, 157017. [CrossRef]
104. Wu, Z.S.; Ren, W.; Wen, L.; Gao, L.; Zhao, J.; Chen, Z.; Zhou, G.; Li, F.; Cheng, H.M. Graphene anchored with Co_3O_4 nanoparticles as anode of lithium ion batteries with enhanced reversible capacity and cyclic performance. *ACS Nano* **2010**, *4*, 3187–3194. [CrossRef]
105. Wang, B.; Wu, X.L.; Shu, C.Y.; Guo, Y.G.; Wang, C.R. Synthesis of CuO/graphene nanocomposite as a high-performance anode material for lithium-ion batteries. *J. Mater. Chem.* **2010**, *20*, 10661–10664. [CrossRef]
106. Sun, Y.; Hu, X.; Luo, W.; Xia, F.; Huang, Y. Reconstruction of conformal nanoscale MnO on graphene as a high-capacity and long-life anode material for lithium ion batteries. *Adv. Funct. Mater.* **2013**, *23*, 2436–2444. [CrossRef]
107. Wang, R.; Wu, S.; Lv, Y.; Lin, Z. Partially crystalline Zn_2GeO_4 nanorod/graphene composites as anode materials for high performance lithium ion batteries. *Langmuir* **2014**, *30*, 8215–8220. [CrossRef]
108. Binitha, G.; Ashish, A.G.; Ramasubramonian, D.; Manikandan, P.; Shaijumon, M.M. Flower-like CoO Microstructures Embedded in 3D Interconnected Graphene Hydrogel as Efficient Anode Material for Lithium-Ion Batteries. In Proceedings of the Electrochemical Society Meeting Abstracts Imlb2016, Riverside Center, Chicago, IL, USA, 23 June 2016; The Electrochemical Society, Inc.: Pennington, NJ, USA, 2016; p. 902.

109. Dong, Y.; Chui, Y.S.; Yang, X.; Ma, R.; Lee, J.M.; Zapien, J.A. Facile Synthesis of Hollow Mesoporous $CoFe_2O_4$ Nanospheres and Graphene Composites as High-Performance Anode Materials for Lithium-Ion Batteries. *ChemElectroChem* **2015**, *2*, 1010–1018. [CrossRef]
110. Lin, L.; Pan, Q. $ZnFe_2O_4$@C/graphene nanocomposites as excellent anode materials for lithium batteries. *J. Mater. Chem. A* **2015**, *3*, 1724–1729. [CrossRef]
111. Wang, F.; Cai, J.; Yu, J.; Li, C.; Yang, Z. Simultaneous electrospinning and electrospraying: Fabrication of a carbon nanofibre/MnO/reduced graphene oxide thin film as a high-performance anode for lithium-ion batteries. *ChemElectroChem* **2018**, *5*, 51–61. [CrossRef]
112. Yang, Z.; Huang, Y.; Hu, J.; Xiong, L.; Luo, H.; Wan, Y. Nanocubic $CoFe_2O_4$/graphene composite for superior lithium-ion battery anodes. *Synth. Met.* **2018**, *242*, 92–98. [CrossRef]
113. Weng, S.C.; Brahma, S.; Huang, P.C.; Huang, Y.C.; Lee, Y.H.; Chang, C.C.; Huang, J.L. Enhanced capacity and significant rate capability of Mn_3O_4/reduced graphene oxide nanocomposite as high performance anode material in lithium-ion batteries. *Appl. Surf. Sci.* **2020**, *505*, 144629. [CrossRef]
114. Wang, L.; Wei, G.; Dong, X.; Zhao, Y.; Xing, Z.; Hong, H.; Ju, Z. Hollow α-Fe_2O_3 Nanotubes Embedded in Graphene Aerogel as High-Performance Anode Material for Lithium-Ion Batteries. *ChemistrySelect* **2019**, *4*, 11370–11377. [CrossRef]
115. Wu, D.; Ouyang, Y.; Zhang, W.; Chen, Z.; Li, Z.; Wang, S.; Wang, F.; Li, H.; Zhang, L.Y. Hollow cobalt oxide nanoparticles embedded porous reduced graphene oxide anode for high performance lithium ion batteries. *Appl. Surf. Sci.* **2020**, *508*, 145311. [CrossRef]
116. Zhou, C.; Liu, J.; Guo, S.; Zhang, P.; Li, S.; Yang, Y.; Wu, J.; Chen, L.; Wang, M. Nanoporous CoO Nanowire Clusters Grown on Three-Dimensional Porous Graphene Cloth as Free-Standing Anode for Lithium-Ion Batteries. *ChemElectroChem* **2020**, *7*, 1573–1580. [CrossRef]
117. Tan, Q.; Wang, C.; Cao, Y.; Liu, X.; Cao, H.; Wu, G.; Xu, B. Synthesis of a zinc ferrite effectively encapsulated by reduced graphene oxide composite anode material for high-rate lithium ion storage. *J. Colloid Interface Sci.* **2020**, *579*, 723–732. [CrossRef]
118. Zhang, X.; Li, S.; El-Khodary, S.A.; Zou, B.; Yang, S.; Ng, D.H.; Liu, X.; Lian, J.; Li, H. Porous α-Fe2O3 nanoparticles encapsulated within reduced graphene oxide as superior anode for lithium-ion battery. *Nanotechnology* **2020**, *31*, 145404. [CrossRef]
119. Lian, X.; Cai, M.; Qin, L.; Cao, Y.; Wu, Q.-H. Synthesis of hierarchical nanospheres Fe_2O_3/graphene composite and its application in lithium-ion battery as a high-performance anode material. *Ionics* **2016**, *22*, 2015–2020. [CrossRef]
120. Zheng, P.; Liu, T.; Su, Y.; Zhang, L.; Guo, S. TiO_2 nanotubes wrapped with reduced graphene oxide as a high-performance anode material for lithium-ion batteries. *Sci. Rep.* **2016**, *6*, 36580. [CrossRef]
121. Wang, S.; Wang, R.; Chang, J.; Hu, N.; Xu, C. Self-supporting Co_3O_4/graphene hybrid films as binder-free anode materials for lithium ion batteries. *Sci. Rep.* **2018**, *8*, 3182. [CrossRef]
122. Wang, X.; Zhou, X.; Yao, K.; Zhang, J.; Liu, Z. A SnO2/graphene composite as a high stability electrode for lithium ion batteries. *Carbon* **2011**, *49*, 133–139. [CrossRef]
123. Zhu, X.; Zhu, Y.; Murali, S.; Stoller, M.D.; Ruoff, R.S. Nanostructured reduced graphene oxide/Fe_2O_3 composite as a high-performance anode material for lithium ion batteries. *ACS Nano* **2011**, *5*, 3333–3338. [CrossRef]
124. Zhou, G.; Wang, D.-W.; Li, F.; Zhang, L.; Li, N.; Wu, Z.-S.; Wen, L.; Lu, G.Q.; Cheng, H.-M. Graphene-wrapped Fe_3O_4 anode material with improved reversible capacity and cyclic stability for lithium ion batteries. *Chem. Mater.* **2010**, *22*, 5306–5313. [CrossRef]
125. Sun, Y.; Hu, X.; Luo, W.; Huang, Y. Self-assembled hierarchical MoO_2/graphene nanoarchitectures and their application as a high-performance anode material for lithium-ion batteries. *ACS Nano* **2011**, *5*, 7100–7107. [CrossRef]
126. Chen, D.; Ji, G.; Ma, Y.; Lee, J.Y.; Lu, J. Graphene-encapsulated hollow Fe3O4 nanoparticle aggregates as a high-performance anode material for lithium ion batteries. *ACS Appl. Mater. Interfaces* **2011**, *3*, 3078–3083. [CrossRef]
127. Zhou, W.; Zhu, J.; Cheng, C.; Liu, J.; Yang, H.; Cong, C.; Guan, C.; Jia, X.; Fan, H.J.; Yan, Q. A general strategy toward graphene@ metal oxide core–shell nanostructures for high-performance lithium storage. *Energy Environ. Sci.* **2011**, *4*, 4954–4961. [CrossRef]
128. Yang, S.; Feng, X.; Müllen, K. Sandwich-like, graphene-based titania nanosheets with high surface area for fast lithium storage. *Adv. Mater.* **2011**, *23*, 3575–3579. [CrossRef] [PubMed]
129. Wang, D.; Kou, R.; Choi, D.; Yang, Z.; Nie, Z.; Li, J.; Saraf, L.V.; Hu, D.; Zhang, J.; Graff, G.L. Ternary self-assembly of ordered metal oxide− graphene nanocomposites for electrochemical energy storage. *ACS Nano* **2010**, *4*, 1587–1595. [CrossRef]
130. Jayashree, M.; Parthibavarman, M.; BoopathiRaja, R.; Prabhu, S.; Ramesh, R. Ultrafine MnO2/graphene based hybrid nanoframeworks as high-performance flexible electrode for energy storage applications. *J. Mater. Sci. Mater. Electron.* **2020**, *31*, 6910–6918. [CrossRef]
131. Shi, Y.; Wen, L.; Li, F.; Cheng, H.-M. Nanosized $Li_4Ti_5O_{12}$/graphene hybrid materials with low polarization for high rate lithium ion batteries. *J. Power Sources* **2011**, *196*, 8610–8617. [CrossRef]
132. Wang, G.; Liu, T.; Luo, Y.; Zhao, Y.; Ren, Z.; Bai, J.; Wang, H. Preparation of Fe_2O_3/graphene composite and its electrochemical performance as an anode material for lithium ion batteries. *J. Alloys Compd.* **2011**, *509*, L216–L220. [CrossRef]
133. Wu, Z.-S.; Zhou, G.; Yin, L.-C.; Ren, W.; Li, F.; Cheng, H.-M. Graphene/metal oxide composite electrode materials for energy storage. *Nano Energy* **2012**, *1*, 107–131. [CrossRef]

134. Fu, L.; Wang, X.; Ma, J.; Zhang, C.; He, J.; Xu, H.; Chai, J.; Li, S.; Chai, F.; Cui, G. Graphene-Encapsulated Copper tin Sulfide Submicron Spheres as High-Capacity Binder-Free Anode for Lithium-Ion Batteries. *ChemElectroChem* **2017**, *4*, 1124–1129. [CrossRef]
135. Qin, G.T.; Ding, L.; Zeng, M.; Zhang, K.B.; Zhang, Y.Q.; Bai, Y.; Wen, J.W.; Li, J. Mesoporous Fe_2O_3/N-doped graphene composite as an anode material for lithium ion batteries with greatly enhanced electrochemical performance. *J. Electroanal. Chem.* **2020**, *866*, 114176. [CrossRef]
136. Wang, F.; Cheng, T.; Zong, J.; Zhao, M.; Yang, S.; Song, X. SnO_2/Graphene Nanocomposite Coated by Carbonized Polyacrylic Acid Hydrogel as a High-Performance Anode for Lithium-Ion Batteries. *ChemistrySelect* **2019**, *4*, 8082–8088. [CrossRef]
137. Wang, J.; Tian, J.; Naren; Wang, X.; Qin, Z.; Shan, Z. Synthesis of MoS_2 and Graphene Composites as the Anode Materials for Li-Ion Batteries. *Energy Technol.* **2018**, *6*, 1913–1920. [CrossRef]
138. Liu, H.; Zou, Y.; Tao, L.; Ma, Z.; Liu, D.; Zhou, P.; Liu, H.; Wang, S. Sandwiched thin-film anode of chemically bonded black phosphorus/graphene hybrid for lithium-ion battery. *Small* **2017**, *13*, 1700758. [CrossRef] [PubMed]
139. Chen, D.; Quan, H.; Huang, Z.; Guo, L. Mesoporous Manganese Sulfide Spheres Anchored on Graphene Sheets as High-Capacity and Long-Life Anode Materials for Lithium-Ion Batteries. *ChemElectroChem* **2015**, *2*, 1314–1320. [CrossRef]
140. Liang, Y.; Li, Y.; Wang, H.; Dai, H. Strongly coupled inorganic/nanocarbon hybrid materials for advanced electrocatalysis. *J. Am. Ceram. Soc.* **2013**, *135*, 2013–2036. [CrossRef]
141. Liang, Y.; Li, Y.; Wang, H.; Zhou, J.; Wang, J.; Regier, T.; Dai, H. Co_3O_4 nanocrystals on graphene as a synergistic catalyst for oxygen reduction reaction. *Nat. Mater.* **2011**, *10*, 780–786. [CrossRef]
142. Liu, Z.; Fu, H.; Gao, B.; Wang, Y.; Li, K.; Sun, Y.; Yin, J.; Kan, J. In-situ synthesis of Fe_2O_3/rGO using different hydrothermal methods as anode materials for lithium-ion batteries. *Rev. Adv. Mater. Sci.* **2020**, *59*, 477–486. [CrossRef]
143. Park, A.R.; Kim, J.S.; Kim, K.S.; Zhang, K.; Park, J.; Park, J.H.; Lee, J.K.; Yoo, P.J. Si–Mn/Reduced graphene oxide nanocomposite anodes with enhanced capacity and stability for lithium-ion batteries. *ACS Appl. Mater. Interfaces* **2014**, *6*, 1702–1708. [CrossRef] [PubMed]
144. Wang, Y.; Su, D.; Ung, A.; Ahn, J.H.; Wang, G. Hollow $CoFe_2O_4$ nanospheres as a high capacity anode material for lithium ion batteries. *Nanotechnology* **2012**, *23*, 055402. [CrossRef] [PubMed]
145. Zhao, S.; Guo, J.; Jiang, F.; Su, Q.; Du, G. Porous $CoFe_2O_4$ nanowire arrays on carbon cloth as binder-free anodes for flexible lithium-ion batteries. *Mater. Res. Bull.* **2016**, *79*, 22–28. [CrossRef]
146. Xia, H.; Zhu, D.; Fu, Y.; Wang, X. $CoFe_2O_4$-graphene nanocomposite as a high-capacity anode material for lithium-ion batteries. *Electrochim. Acta* **2012**, *83*, 166–174. [CrossRef]
147. Zhang, L.; Wei, T.; Jiang, Z.; Liu, C.; Jiang, H.; Chang, J.; Sheng, L.; Zhou, Q.; Yuan, L.; Fan, Z. Electrostatic interaction in electrospun nanofibers: Double-layer carbon protection of $CoFe_2O_4$ nanosheets enabling ultralong-life and ultrahigh-rate lithium ion storage. *Nano Energy* **2018**, *48*, 238–247. [CrossRef]
148. Ren, S.; Zhao, X.; Chen, R.; Fichtner, M. A facile synthesis of encapsulated $CoFe_2O_4$ into carbon nanofibres and its application as conversion anodes for lithium ion batteries. *J. Power Sources* **2014**, *260*, 205–210. [CrossRef]
149. Dou, Q.; Wong, K.W.; Li, Y.; Ng, K.M. Novel nanosheets of ferrite nanoparticle arrays in carbon matrix from single source precursors: An anode material for lithium-ion batteries. *J. Mater. Sci.* **2018**, *53*, 4456–4466. [CrossRef]
150. Zhu, Y.; Lv, X.; Zhang, L.; Guo, X.; Liu, D.; Chen, J.; Ji, J. Liquid-solid-solution assembly of $CoFe_2O_4$/graphene nanocomposite as a high-performance lithium-ion battery anode. *Electrochim. Acta* **2016**, *215*, 247–252. [CrossRef]
151. Liu, X.; Teng, D.; Li, T.; Yu, Y.; Shao, X.; Yang, X. Phosphorus-doped tin oxides/carbon nanofibers webs as lithium-ion battery anodes with enhanced reversible capacity. *J. Power Sources* **2014**, *272*, 614–621. [CrossRef]
152. Xu, H.; Shi, L.; Wang, Z.; Liu, J.; Zhu, J.; Zhao, Y.; Zhang, M.; Yuan, S. Fluorine-doped tin oxide nanocrystal/reduced graphene oxide composites as lithium ion battery anode material with high capacity and cycling stability. *ACS Appl. Mater. Interfaces* **2015**, *7*, 27486–27493. [CrossRef] [PubMed]
153. Zoller, F.; Peters, K.; Zehetmaier, P.M.; Zeller, P.; Doblinger, M.; Bein, T.; Sofer, Z.; Fattakhova-Rohlfing, D. Making ultrafast high-capacity anodes for lithium-ion batteries via antimony doping of nanosized tin oxide/graphene composites. *Adv. Funct. Mater.* **2018**, *28*, 1706529. [CrossRef]
154. Ma, Y.; Ma, Y.; Ulissi, U.; Ji, Y.; Streb, C.; Bresser, D.; Passerini, S. Influence of the doping ratio and the carbon coating content on the electrochemical performance of Co-doped SnO2 for lithium-ion anodes. *Electrochim. Acta* **2018**, *277*, 100–109. [CrossRef]
155. Ye, X.; Zhang, W.; Liu, Q.; Wang, S.; Yang, Y.; Wei, H. One-step synthesis of Ni-doped SnO_2 nanospheres with enhanced lithium ion storage performance. *New J. Chem.* **2015**, *39*, 130–135. [CrossRef]
156. Zhao, K.; Zhang, L.; Xia, R.; Dong, Y.; Xu, W.; Niu, C.; He, L.; Yan, M.; Qu, L.; Mai, L. SnO_2 Quantum dots@graphene oxide as a high-rate and long-life anode material for lithium-ion batteries. *Small* **2016**, *12*, 588–594. [CrossRef]
157. Hu, R.; Chen, D.; Waller, G.; Ouyang, Y.; Chen, Y.; Zhao, B.; Rainwater, B.; Yang, C.; Zhu, M.; Liu, M. Dramatically enhanced reversibility of Li_2O in SnO_2-based electrodes: The effect of nanostructure on high initial reversible capacity. *Energy Environ. Sci.* **2016**, *9*, 595–603. [CrossRef]
158. Hu, R.; Zhang, H.; Lu, Z.; Liu, J.; Zeng, M.; Yang, L.; Yuan, B.; Zhu, M. Unveiling critical size of coarsened Sn nanograins for achieving high round-trip efficiency of reversible conversion reaction in lithiated SnO_2 nanocrystals. *Nano Energy* **2018**, *45*, 255–265. [CrossRef]

159. Han, M.A.; Kim, H.J.; Lee, H.C.; Park, J.S.; Lee, H.N. Effects of porosity and particle size on the gas sensing properties of SnO_2 films. *Appl. Surf. Sci.* **2019**, *481*, 133–137. [CrossRef]
160. Yang, F.; Li, W.; Tang, B. Facile synthesis of amorphous UiO-66 (Zr-MOF) for supercapacitor application. *J. Alloys Compd.* **2018**, *733*, 8–14. [CrossRef]
161. Huang, W.; Liu, N.; Zhang, X.; Wu, M.; Tang, L. Metal organic framework g-C3N4/MIL-53 (Fe) heterojunctions with enhanced photocatalytic activity for Cr (VI) reduction under visible light. *Appl. Surf. Sci.* **2017**, *425*, 107–116. [CrossRef]
162. Peng, H.J.; Hao, G.X.; Chu, Z.H.; He, C.L.; Lin, X.M.; Cai, Y.P. Mesoporous spindle-like hollow CuO/C fabricated from a Cu-based metal-organic framework as anodes for high-performance lithium storage. *J. Alloys Compd.* **2017**, *727*, 1020–1026. [CrossRef]
163. Courtney, I.A.; McKinnon, W.R.; Dahn, J.R. On the aggregation of tin in SnO composite glasses caused by the reversible reaction with lithium. *J. Electrochem. Soc.* **1999**, *146*, 59. [CrossRef]
164. Yoo, E.; Kim, J.; Hosono, E.; Zhou, H.S.; Kudo, T.; Honma, I. Large reversible Li storage of graphene nanosheet families for use in rechargeable lithium ion batteries. *Nano Lett.* **2008**, *8*, 2277–2282. [CrossRef] [PubMed]
165. Teh, P.F.; Sharma, Y.; Pramana, S.S.; Srinivasan, M. Nanoweb anodes composed of one-dimensional, high aspect ratio, size tunable electrospun $ZnFe_2O_4$ nanofibers for lithium ion batteries. *J. Mater. Chem.* **2011**, *21*, 14999–15008. [CrossRef]
166. Bresser, D.; Paillard, E.; Kloepsch, R.; Krueger, S.; Fiedler, M.; Schmitz, R.; Baither, D.; Winter, M.; Passerini, S. Carbon coated $ZnFe_2O_4$ nanoparticles for advanced lithium-ion anodes. *Adv. Energy Mater.* **2013**, *3*, 513–523. [CrossRef]
167. Qiu, D.; Ma, L.; Zheng, M.; Lin, Z.; Zhao, B.; Wen, Z.; Hu, Z.; Pu, L.; Shi, Y. MnO nanoparticles anchored on graphene nanosheets via in situ carbothermal reduction as high-performance anode materials for lithium-ion batteries. *Mater. Lett.* **2012**, *84*, 9–12. [CrossRef]
168. Luo, W.; Hu, X.; Sun, Y.; Huang, Y. Controlled synthesis of mesoporous MnO/C networks by microwave irradiation and their enhanced lithium-storage properties. *ACS Appl. Mater. Interfaces* **2013**, *5*, 1997–2003. [CrossRef]
169. Wang, W.; Dahl, M.; Yin, Y. Hollow nanocrystals through the nanoscale Kirkendall effect. *Chem. Mater.* **2013**, *25*, 1179–1189. [CrossRef]
170. Ma, Y.; Ma, Y.; Geiger, D.; Kaiser, U.; Zhang, H.; Kim, G.T.; Diemant, T.; Behm, R.J.; Varzi, A.; Passerini, S. ZnO/$ZnFe_2O_4$/N-doped C micro-polyhedrons with hierarchical hollow structure as high-performance anodes for lithium-ion batteries. *Nano Energy* **2017**, *42*, 341–352. [CrossRef]
171. Bresser, D.; Mueller, F.; Fiedler, M.; Krueger, S.; Kloepsch, R.; Baither, D.; Winter, M.; Paillard, E.; Passerini, S. Transition-metal-doped zinc oxide nanoparticles as a new lithium-ion anode material. *Chem. Mater.* **2013**, *25*, 4977–4985. [CrossRef]
172. Sun, X.; Zhang, H.; Zhou, L.; Huang, X.; Yu, C. Polypyrrole-coated zinc ferrite hollow spheres with improved cycling stability for lithium-ion batteries. *Small* **2016**, *12*, 3732–3737. [CrossRef] [PubMed]
173. Wang, S.; Shi, L.; Chen, G.; Ba, C.; Wang, Z.; Zhu, J.; Zhao, Y.; Zhang, M.; Yuan, S. In situ synthesis of tungsten-doped SnO_2 and graphene nanocomposites for high-performance anode materials of lithium-ion batteries. *ACS Appl. Mater. Interfaces* **2017**, *9*, 17163–17171. [CrossRef] [PubMed]
174. Ma, X.; Ning, G.; Qi, C.; Xu, C.; Gao, J. Phosphorus and nitrogen dual-doped few-layered porous graphene: A high-performance anode material for lithium-ion batteries. *ACS Appl. Mater. Interfaces* **2014**, *6*, 14415–14422. [CrossRef]
175. Zheng, Y.; Jiao, Y.; Ge, L.; Jaroniec, M.; Qiao, S.Z. Two-step boron and nitrogen doping in graphene for enhanced synergistic catalysis. *Angew. Chem. Int. Ed.* **2013**, *52*, 3110–3116. [CrossRef]
176. Wu, Z.-S.; Ren, W.; Xu, L.; Li, F.; Cheng, H.-M. Doped graphene sheets as anode materials with superhigh rate and large capacity for lithium ion batteries. *ACS Nano* **2011**, *5*, 5463–5471. [CrossRef] [PubMed]
177. Ma, C.; Shao, X.; Cao, D. Nitrogen-doped graphene nanosheets as anode materials for lithium ion batteries: A first-principles study. *J. Mater. Chem.* **2012**, *22*, 8911–8915. [CrossRef]
178. Wang, X.; Weng, Q.; Liu, X.; Wang, X.; Tang, D.-M.; Tian, W.; Zhang, C.; Yi, W.; Liu, D.; Bando, Y. Atomistic origins of high rate capability and capacity of N-doped graphene for lithium storage. *Nano Lett.* **2014**, *14*, 1164–1171. [CrossRef]
179. Nankya, R.; Opar, D.O.; Kim, M.-J.; Paek, S.-M.; Jung, H. Synergetic effect of nitrogen and sulfur co-doping in mesoporous graphene for enhanced energy storage properties in supercapacitors and lithium-ion batteries. *J. Solid State Chem.* **2020**, *289*, 121451. [CrossRef]
180. Jiao, D.; Xie, Z.; Wan, Q.; Wei, Z.; Yan, X.; Butt, F.K.; Qu, M. Improved lithium storage properties of the reduced graphene oxide/graphite composites based on functional groups control synthesis. *Int. J. Electrochem. Sci.* **2019**, *14*, 848–860. [CrossRef]
181. Sun, D.; Yang, J.; Yan, X. Hierarchically porous and nitrogen, sulfur-codoped graphene-like microspheres as a high capacity anode for lithium ion batteries. *Chem. Commun.* **2015**, *51*, 2134–2137. [CrossRef]
182. Shin, W.H.; Jeong, H.M.; Kim, B.G.; Kang, J.K.; Choi, J.W. Nitrogen-doped multiwall carbon nanotubes for lithium storage with extremely high capacity. *Nano Lett.* **2012**, *12*, 2283–2288. [CrossRef] [PubMed]
183. Nakajima, T.; Koh, M.; Singh, R.N.; Shimada, M. Electrochemical behavior of surface-fluorinated graphite. *Electrochim. Acta* **1999**, *44*, 2879–2888. [CrossRef]
184. Huang, S.; Li, Y.; Feng, Y.; An, H.; Long, P.; Qin, C.; Feng, W. Nitrogen and fluorine co-doped graphene as a high-performance anode material for lithium-ion batteries. *J. Mater. Chem. A* **2015**, *3*, 23095–23105. [CrossRef]
185. Liu, T.; Zhang, L.; Cheng, B.; Yu, J. Hollow carbon spheres and their hybrid nanomaterials in electrochemical energy storage. *Adv. Energy Mater.* **2019**, *9*, 1803900. [CrossRef]

186. Yin, Y.; Rioux, R.M.; Erdonmez, C.K.; Hughes, S.; Somorjai, G.A.; Alivisatos, A.P. Formation of hollow nanocrystals through the nanoscale Kirkendall effect. *Science* **2004**, *304*, 711–714. [CrossRef]
187. Yang, H.G.; Zeng, H.C. Preparation of hollow anatase TiO_2 nanospheres via Ostwald ripening. *J. Phys. Chem. B* **2004**, *108*, 3492–3495. [CrossRef]
188. Sun, Y.; Wiley, B.; Li, Z.-Y.; Xia, Y. Synthesis and optical properties of nanorattles and multiple-walled nanoshells/nanotubes made of metal alloys. *JACS* **2004**, *126*, 9399–9406. [CrossRef] [PubMed]
189. Zhang, Q.; Zhang, T.; Ge, J.; Yin, Y. Permeable silica shell through surface-protected etching. *Nano Lett.* **2008**, *8*, 2867–2871. [CrossRef]
190. Fan, H.J.; Gosele, U.; Zacharias, M. Formation of nanotubes and hollow nanoparticles based on Kirkendall and diffusion processes: A review. *Small* **2007**, *3*, 1660–1671. [CrossRef]
191. Du, Y.; Hou, M.; Zhou, D.; Wang, Y.; Wang, C.; Xia, Y. Interconnected sandwich structure carbon/Si-SiO_2/carbon nanospheres composite as high performance anode material for lithium-ion batteries. *J. Energy Chem.* **2014**, *23*, 315–323. [CrossRef]
192. Zhou, Y.; Guo, H.; Yang, Y.; Wang, Z.; Li, X.; Zhou, R.; Peng, W. Facile synthesis of silicon/carbon nanospheres composite anode materials for lithium-ion batteries. *Mater. Lett.* **2016**, *168*, 138–142. [CrossRef]
193. Liu, X.; Chen, Y.; Liu, H.; Liu, Z.Q. SiO_2@C hollow sphere anodes for lithium-ion batteries. *J. Mater. Sci. Technol.* **2017**, *33*, 239–245. [CrossRef]
194. Cao, B.; Liu, Z.; Xu, C.; Huang, J.; Fang, H.; Chen, Y. High-rate-induced capacity evolution of mesoporous C@SnO_2@ C hollow nanospheres for ultra-long cycle lithium-ion batteries. *J. Power Sources* **2019**, *414*, 233–241. [CrossRef]
195. Lei, Y.; Li, S.; Du, M.; Mi, J.; Gao, D.C.; Hao, L.; Jiang, L.J.; Luo, M.; Jiang, W.Q.; Li, F. Preparation of double-shell Si@SnO_2@C nanocomposite as anode for lithium-ion batteries by hydrothermal method. *Rare Met.* **2023**, *42*, 2972–2981. [CrossRef]
196. Chen, F.; Chen, Z.; Dai, Z.; Wang, S.; Zhang, Z.; Chen, D. Self-templating synthesis of carbon-encapsulated SnO_2 hollow spheres: A promising anode material for lithium-ion batteries. *J. Alloys Compd.* **2020**, *816*, 152495. [CrossRef]
197. Lu, B.; Ma, B.; Deng, X.; Wu, B.; Wu, Z.; Luo, J.; Wang, X.; Chen, G. Dual stabilized architecture of hollow Si@TiO_2@C nanospheres as anode of high-perforance Li-ion battery. *Chem. Eng. J.* **2018**, *351*, 269–279. [CrossRef]
198. Jo, A.H.; Kim, S.Y.; Kim, J.H.; Kim, Y.A.; Yang, C.M. Robust Core–Shell Carbon-Coated Silicon-Based Composite Anode with Electrically Interconnected Spherical Framework for Lithium-Ion Battery. *Int. J. Energy Res.* **2023**, 6874429. [CrossRef]
199. Zhan, L.; Wang, Y.; Qiao, W.; Ling, L.; Yang, S. Hollow carbon spheres with encapsulation of Co_3O_4 nanoparticles as anode material for lithium ion batteries. *Electrochim. Acta* **2012**, *78*, 440–445. [CrossRef]
200. Luo, Y.; Zhou, X.; Zhong, Y.; Yang, M.; Wei, J.; Zhou, Z. Preparation of core–shell porous magnetite@carbon nanospheres through chemical vapor deposition as anode materials for lithium-ion batteries. *Electrochim. Acta* **2015**, *154*, 136–141. [CrossRef]
201. Wang, K.; Chen, M.; He, Z.; Huang, L.A.; Zhu, S.; Pei, S.; Guo, J.; Shao, H.; Wang, J. Hierarchical Fe_3O_4@ C nanospheres derived from Fe_2O_3/MIL-100 (Fe) with superior high-rate lithium storage performance. *J. Alloys Compd.* **2018**, *755*, 154–162. [CrossRef]
202. Liu, Y.; Li, Y.; Zhong, M.; Hu, Y.; Hu, P.; Zhu, M.; Li, W.; Li, Y. A facile synthesis of core-shell structured ZnO@C nanosphere and their high performance for lithium ion battery anode. *Mater. Lett.* **2016**, *171*, 244–247. [CrossRef]
203. Wang, W.L.; Park, J.Y.; Jin, E.M.; Gu, H.B. Hierarchical mesoporous rutile TiO_2/C composite nanospheres as lithium-ion battery anode materials. *Ceram. Int.* **2016**, *42*, 598–606. [CrossRef]
204. Chen, Y.; Wu, J.; Yang, W.; Fu, Y.; Zhou, R.; Chen, S.; Zhang, L.; Song, Y.; Wang, L. Zn/Fe-MOFs-derived hierarchical ball-in-ball ZnO/$ZnFe_2O_4$@ carbon nanospheres with exceptional lithium storage performance. *J. Alloys Compd.* **2016**, *688*, 211–218. [CrossRef]
205. Liu, R.; Zhang, C.; Wang, Q.; Shen, C.; Wang, Y.; Dong, Y.; Zhang, N.; Wu, M. Facile synthesis of α-Fe_2O_3@C hollow spheres as ultra-long cycle performance anode materials for lithium ion battery. *J. Alloys Compd.* **2018**, *742*, 490–496. [CrossRef]
206. Liu, K.; Zou, F.; Sun, Y.; Yu, Z.; Liu, X.; Zhou, L.; Xia, Y.; Vogt, B.D.; Zhu, Y. Self-assembled Mn_3O_4/C nanospheres as high-performance anode materials for lithium ion batteries. *J. Power Sources* **2018**, *395*, 92–97. [CrossRef]
207. Yu, M.; Sun, Y.; Du, H.; Wang, C.; Li, W.; Dong, R.; Sun, H.; Geng, B. Hollow porous carbon spheres doped with a low content of Co_3O_4 as anode materials for high performance lithium-ion batteries. *Electrochim. Acta* **2019**, *317*, 562–569. [CrossRef]
208. Trukawka, M.; Wenelska, K.; Singer, L.; Klingeler, R.; Chen, X.; Mijowska, E. Hollow carbon spheres loaded with uniform dispersion of copper oxide nanoparticles for anode in lithium-ion batteries. *J. Alloys Compd.* **2021**, *853*, 156700. [CrossRef]
209. Zhou, Y.; Zhang, P.; Sun, Y.; Shen, Y.; Xie, A. Rapid Synthesis and Good Performance of TiO_2/Nitrogen-Doped Carbon Spheres as Anode Materials for Lithium Ion Batteries. *Energy Technol.* **2018**, *6*, 1660–1666. [CrossRef]
210. Guo, L.; Ding, Y.; Qin, C.; Song, W.; Sun, S.; Fang, K.; Li, W.; Du, J.; Wang, F. Anchoring Mn_3O_4 nanoparticles onto nitrogen-doped porous carbon spheres derived from carboxymethyl chitosan as superior anodes for lithium-ion batteries. *J. Alloys Compd.* **2018**, *735*, 209–217. [CrossRef]
211. Dou, P.; Cao, Z.; Wang, C.; Zheng, J.; Xu, X. Ultrafine Sn nanoparticles embedded in shell of N-doped hollow carbon spheres as high rate anode for lithium-ion batteries. *Appl. Surf. Sci.* **2017**, *404*, 342–349. [CrossRef]
212. Hong, Y.J.; Kang, Y.C. General formation of tin nanoparticles encapsulated in hollow carbon spheres for enhanced lithium storage capability. *Small* **2015**, *11*, 2157–2163. [CrossRef] [PubMed]
213. Zhang, W.M.; Hu, J.S.; Guo, Y.G.; Zheng, S.F.; Zhong, L.S.; Song, W.G.; Wan, L.J. Tin-nanoparticles encapsulated in elastic hollow carbon spheres for high-performance anode material in lithium-Ion batteries. *Adv. Mater.* **2008**, *20*, 1160–1165. [CrossRef]

214. Zhang, N.; Wang, Y.; Jia, M.; Liu, Y.; Xu, J.; Jiao, L.; Cheng, F. Ultrasmall Sn nanoparticles embedded in spherical hollow carbon for enhanced lithium storage properties. *Chem. Commun.* **2018**, *54*, 1205–1208. [CrossRef] [PubMed]
215. Zhang, W.; Wang, X.; Zhou, H.; Chen, J.; Zhang, X. Fe_3O_4C open hollow sphere assembled by nanocrystals and its application in lithium ion battery. *J. Alloys Compd.* **2012**, *521*, 39–44. [CrossRef]
216. Yan, Z.; Jiang, X.; Dai, Y.; Xiao, W.; Li, X.; Du, N.; He, G. Pulverization control by confining Fe_3O_4 nanoparticles individually into macropores of hollow carbon spheres for high-performance Li-ion batteries. *ACS Appl. Mater. Interfaces* **2018**, *10*, 2581–2590. [CrossRef]
217. Kim, Y.; Choi, E.; Kim, J.G.; Lee, S.; Yoon, W.; Ham, M.H.; Kim, W.B. Size-Controlled Hollow Spheres of C/α-Fe_2O_3 Prepared through the Quasiemulsion-Templated Method and Their Electrochemical Properties for Lithium-Ion Storage. *ChemElectroChem* **2017**, *4*, 2045–2051. [CrossRef]
218. Zheng, F.; He, M.; Yang, Y.; Chen, Q. Nano electrochemical reactors of Fe_2O_3 nanoparticles embedded in shells of nitrogen-doped hollow carbon spheres as high-performance anodes for lithium-ion batteries. *Nanoscale* **2015**, *7*, 3410–3417. [CrossRef]
219. Geng, H.; Zhou, Q.; Pan, Y.; Gu, H.; Zheng, J. Preparation of fluorine-doped, carbon-encapsulated hollow Fe_3O_4 spheres as an efficient anode material for Li-ion batteries. *Nanoscale* **2014**, *6*, 3889–3894. [CrossRef] [PubMed]
220. Zhao, Y.; Li, J.; Wu, C.; Ding, Y.; Guan, L. A Yolk–Shell Fe_3O_4@C Composite as an Anode Material for High-Rate Lithium Batteries. *ChemPlusChem* **2012**, *77*, 748–751. [CrossRef]
221. Balach, J.; Wu, H.; Polzer, F.; Kirmse, H.; Zhao, Q.; Wei, Z.; Yuan, J. Poly (ionic liquid)-derived nitrogen-doped hollow carbon spheres: Synthesis and loading with Fe_2O_3 for high-performance lithium ion batteries. *RSC Adv.* **2013**, *3*, 7979–7986. [CrossRef]
222. Li, D.; Feng, C.; Liu, H.; Guo, Z. Hollow carbon spheres with encapsulated germanium as an anode material for lithium ion batteries. *J. Mater. Chem. A* **2015**, *3*, 978–981. [CrossRef]
223. Lou, X.W.; Li, C.M.; Archer, L.A. Designed synthesis of coaxial SnO_2@carbon hollow nanospheres for highly reversible lithium storage. *Adv. Mater.* **2009**, *21*, 2536–2539. [CrossRef]
224. Yu, L.; Liu, J.; Xu, X.; Zhang, L.; Hu, R.; Liu, J.; Yang, L.; Zhu, M. Metal–organic framework-derived NiSb alloy embedded in carbon hollow spheres as superior lithium-ion battery anodes. *ACS Appl. Mater. Interfaces* **2017**, *9*, 2516–2525. [CrossRef] [PubMed]
225. Li, X.; Zhang, Y.; Zhang, H.; Feng, Y.; Wang, Y. Porous double-shelled SnO_2@ C hollow spheres as high-performance anode material for lithium ion batteries. *Electrochim. Acta* **2016**, *195*, 208–215. [CrossRef]
226. Li, J.; Wu, P.; Ye, Y.; Wang, H.; Zhou, Y.; Tang, Y.; Lu, T. Designed synthesis of SnO_2@C yolk–shell spheres for high-performance lithium storage. *CrystEngComm* **2014**, *16*, 517–521. [CrossRef]
227. Li, L.; Zhang, L.; Chai, F.; Wang, T.; Li, Z.; Xie, H.; Wang, C.; Su, Z. SnO_2@N-Doped Carbon Hollow Nanoclusters for Advanced Lithium-Ion Battery Anodes. *Eur. J. Inorg. Chem.* **2016**, *2016*, 812–817. [CrossRef]
228. Guo, H.; Mao, R.; Tian, D.; Wang, W.; Zhao, D.; Yang, X.; Wang, S. Morphology-controlled synthesis of SnO_2/C hollow core–shell nanoparticle aggregates with improved lithium storage. *J. Mater. Chem. A* **2013**, *1*, 3652–3658. [CrossRef]
229. Lou, X.W.; Deng, D.; Lee, J.Y.; Archer, L.A. Preparation of SnO_2/carbon composite hollow spheres and their lithium storage properties. *Chem. Mater.* **2008**, *20*, 6562–6566. [CrossRef]
230. Hu, L.L.; Yang, L.P.; Zhang, D.; Tao, X.S.; Zeng, C.; Cao, A.M.; Wan, L.J. Designed synthesis of SnO_2–C hollow microspheres as an anode material for lithium-ion batteries. *Chem. Commun.* **2017**, *53*, 11189–11192. [CrossRef]
231. Wang, Y.; Guo, W.; Yang, Y.; Yu, Y.; Li, Q.; Wang, D.; Zhang, F. Rational design of SnO_2@C@MnO_2 hierarchical hollow hybrid nanospheres for a Li-ion battery anode with enhanced performances. *Electrochim. Acta* **2018**, *262*, 1–8. [CrossRef]
232. Zhang, H.; Li, L.; Li, Z.; Zhong, W.; Liao, H.; Li, Z. Controllable synthesis of SnO_2@ carbon hollow sphere based on bi-functional metallo-organic molecule for high-performance anode in Li-ion batteries. *Appl. Surf. Sci.* **2018**, *442*, 65–70. [CrossRef]
233. Choi, J.; Kim, W.S.; Hong, S.H. Highly stable SnO_2–Fe_2O_3–C hollow spheres for reversible lithium storage with extremely long cycle life. *Nanoscale* **2018**, *10*, 4370–4376. [CrossRef] [PubMed]
234. Jaumann, T.; Gerwig, M.; Balach, J.; Oswald, S.; Brendler, E.; Hauser, R.; Kieback, B.; Eckert, J.; Giebeler, L.; Kroke, E. Dichlorosilane-derived nano-silicon inside hollow carbon spheres as a high-performance anode for Li-ion batteries. *J. Mater. Chem. A* **2017**, *5*, 9262–9271. [CrossRef]
235. Wang, C.-W.; Liu, K.-W.; Chen, W.-F.; Zhou, J.-D.; Lin, H.-P.; Hsu, C.-H.; Kuo, P.-L. Mesoporous SiO_2/carbon hollow spheres applied towards a high rate-performance Li-battery anode. *Inorg. Chem. Front.* **2016**, *3*, 1398–1405. [CrossRef]
236. Xu, Y.; Jian, G.; Zachariah, M.R.; Wang, C. Nano-structured carbon-coated CuO hollow spheres as stable and high rate anodes for lithium-ion batteries. *J. Mater. Chem. A* **2013**, *1*, 15486–15490. [CrossRef]
237. Li, F.; Zou, Q.Q.; Xia, Y.Y. CoO-loaded graphitable carbon hollow spheres as anode materials for lithium-ion battery. *J. Power Sources* **2008**, *177*, 546–552. [CrossRef]
238. Wang, Y.; Yu, L.; Lou, X.W. Formation of triple-shelled molybdenum–polydopamine hollow spheres and their conversion into MoO_2/carbon composite hollow spheres for lithium-ion batteries. *Angew. Chem. Int. Ed.* **2016**, *55*, 14668–14672. [CrossRef]
239. Jun, Z.; Jia-jia, C.; Cheng-long, Z.; Hang, Q.; Ming-sen, Z.; Quan-feng, D. The synthesis of a core–shell MnO_2/3D-ordered hollow carbon sphere composite and its superior electrochemical capability for lithium ion batteries. *J. Mater. Chem. A* **2014**, *2*, 6343–6347. [CrossRef]
240. Zang, J.; Ye, J.; Qian, H.; Lin, Y.; Zhang, X.; Zheng, M.; Dong, Q. Hollow carbon sphere with open pore encapsulated MnO2 nanosheets as high-performance anode materials for lithium ion batteries. *Electrochim. Acta* **2018**, *260*, 783–788. [CrossRef]

241. Jin, L.; Qiu, Y.; Deng, H.; Li, W.; Li, H.; Yang, S. Hollow $CuFe_2O_4$ spheres encapsulated in carbon shells as an anode material for rechargeable lithium-ion batteries. *Electrochim. Acta* **2011**, *56*, 9127–9132. [CrossRef]
242. Ding, C.; Jiang, X.; Huang, X.; Zhang, H.; Zhong, W.; Xia, Y.; Dai, C. Hierarchically porous Zn-Co-O NCs-in-carbon hollow microspheres with high rate-capacity and cycle stability as anode materials for lithium-ion batteries. *J. Alloys Compd.* **2018**, *736*, 181–189. [CrossRef]
243. Ma, M.; Wang, H.; Liang, S.; Guo, S.; Zhang, Y.; Du, X. Porous carbon-wrapped cerium oxide hollow spheres synthesized via microwave hydrothermal for long-cycle and high-rate lithium-ion batteries. *Electrochim. Acta* **2017**, *256*, 110–118. [CrossRef]
244. Zhang, Y.; Wang, Y.; Yang, J.; Shi, W.; Yang, H.; Huang, W.; Dong, X. MoS_2 coated hollow carbon spheres for anodes of lithium ion batteries. *2D Mater.* **2016**, *3*, 024001. [CrossRef]
245. Li, H.; Yu, H.; Zhang, X.; Guo, G.; Hu, J.; Dong, A.; Yang, D. Bowl-like 3C-SiC nanoshells encapsulated in hollow graphitic carbon spheres for high-rate lithium-ion batteries. *Chem. Mater.* **2016**, *28*, 1179–1186. [CrossRef]
246. Pei, J.; Geng, H.; Ang, E.H.; Zhang, L.; Cao, X.; Zheng, J.; Gu, H. Controlled synthesis of hollow C@TiO_2@ MoS_2 hierarchical nanospheres for high-performance lithium-ion batteries. *Nanoscale* **2018**, *10*, 17327–17334. [CrossRef]
247. Zeng, X.; Ding, Z.; Ma, C.; Wu, L.; Liu, J.; Chen, L.; Ivey, D.G.; Wei, W. Hierarchical nanocomposite of hollow N-doped carbon spheres decorated with ultrathin WS_2 nanosheets for high-performance lithium-ion battery anode. *ACS Appl. Mater. Interfaces* **2016**, *8*, 18841–18848. [CrossRef]
248. Zhang, H.; Zhou, L.; Huang, X.; Song, H.; Yu, C. Encapsulation of selenium sulfide in double-layered hollow carbon spheres as advanced electrode material for lithium storage. *Nano Res.* **2016**, *9*, 3725–3734. [CrossRef]
249. Ji, S.; Zhang, L.; Yu, L.; Xu, X.; Liu, J. In situ carbon-coating and Ostwald ripening-based route for hollow Ni_3S_4@C spheres with superior Li-ion storage performances. *RSC Adv.* **2016**, *6*, 101752–101759. [CrossRef]
250. Lou, X.W.; Chen, J.S.; Chen, P.; Archer, L.A. One-pot synthesis of carbon-coated SnO_2 nanocolloids with improved reversible lithium storage properties. *Chem. Mater.* **2009**, *21*, 2868–2874. [CrossRef]
251. Wu, P.; Du, N.; Zhang, H.; Zhai, C.; Yang, D. Self-templating synthesis of SnO_2–carbon hybrid hollow spheres for superior reversible lithium ion storage. *ACS Appl. Mater. Interfaces* **2011**, *3*, 1946–1952. [CrossRef]
252. Li, H.Z.; Yang, L.Y.; Liu, J.; Li, S.; Fang, L.; Lu, Y.K.; Yang, H.R.; Liu, S.L.; Lei, M. Improved electrochemical performance of yolk-shell structured SnO_2@ void@ C porous nanowires as anode for lithium and sodium batteries. *J. Power Sources* **2016**, *324*, 780–787. [CrossRef]
253. Hwa, Y.; Kim, W.S.; Yu, B.C.; Hong, S.H.; Sohn, H.J. Enhancement of the cyclability of a Si anode through Co_3O_4 coating by the Sol–Gel method. *J. Phys. Chem. C* **2013**, *117*, 7013–7017. [CrossRef]
254. Liu, D.H.; Lü, H.Y.; Wu, X.L.; Wang, J.; Yan, X.; Zhang, J.P.; Geng, H.; Zhang, Y.; Yan, Q. A new strategy for developing superior electrode materials for advanced batteries: Using a positive cycling trend to compensate the negative one to achieve ultralong cycling stability. *Nanoscale Horiz.* **2016**, *1*, 496–501. [CrossRef] [PubMed]
255. Qiu, M.C.; Yang, L.W.; Qi, X.; Li, J.; Zhong, J.X. Fabrication of ordered NiO coated Si nanowire array films as electrodes for a high performance lithium ion battery. *ACS Appl. Mater. Interfaces* **2010**, *2*, 3614–3618. [CrossRef] [PubMed]
256. Li, W.; Wang, F.; Liu, Y.; Wang, J.; Yang, J.; Zhang, L.; Elzatahry, A.A.; Al-Dahyan, D.; Xia, Y.; Zhao, D. General strategy to synthesize uniform mesoporous TiO_2/graphene/mesoporous TiO_2 sandwich-like nanosheets for highly reversible lithium storage. *Nano Lett.* **2015**, *15*, 2186–2193. [CrossRef] [PubMed]
257. Ou, J.; Li, B.; Deng, H.; Li, K.; Wang, H. A carbon-covered silicon material modified by phytic acid with 3D conductive network as anode for lithium-ion batteries. *Adv. Powder Technol.* **2023**, *34*, 103891. [CrossRef]
258. Yang, J.; Hou, J.; Niu, Y.; Li, W.; Yi, F.; Liu, S.; Li, G.; Xu, M. Improved cycle capability of Titanium-doped Fe_2O_3 anode material for Li-ion batteries. *J. Alloys Compd.* **2017**, *722*, 414–419. [CrossRef]
259. Reddy, M.V.; Yu, T.; Sow, C.H.; Shen, Z.X.; Lim, C.T.; Subba Rao, G.V.; Chowdari, B. α-Fe_2O_3 nanoflakes as an anode material for Li-ion batteries. *Adv. Funct. Mater.* **2007**, *17*, 2792–2799. [CrossRef]
260. Chen, P.C.; Shen, G.; Shi, Y.; Chen, H.; Zhou, C. Preparation and characterization of flexible asymmetric supercapacitors based on transition-metal-oxide nanowire/single-walled carbon nanotube hybrid thin-film electrodes. *ACS Nano* **2010**, *4*, 4403–4411. [CrossRef]
261. Wu, X.-L.; Jiang, L.-Y.; Cao, F.-F.; Guo, Y.-G.; Wan, L.-J. $LiFePO_4$ Nanoparticles Embedded in a Nanoporous Carbon Matrix: Superior Cathode Material for Electrochemical Energy-Storage Devices. *Adv. Mater* **2009**, *21*, 2710–2714. [CrossRef]
262. Wang, L.; He, X.; Li, J.; Sun, W.; Gao, J.; Guo, J.; Jiang, C. Nano-structured phosphorus composite as high-capacity anode materials for lithium batteries. *Angew. Chem. (Int. Ed. Engl.)* **2012**, *51*, 9034–9037. [CrossRef] [PubMed]
263. Cheng, F.; Shen, J.; Peng, B.; Pan, Y.; Tao, Z.; Chen, J. Rapid room-temperature synthesis of nanocrystalline spinels as oxygen reduction and evolution electrocatalysts. *Nat. Chem.* **2011**, *3*, 79–84. [CrossRef]
264. Maharajan, S.; Kwon, N.H.; Brodard, P.; Fromm, K.M. A nano-rattle SnO_2@ carbon composite anode material for high-energy Li-ion batteries by melt diffusion impregnation. *Nanomaterials* **2020**, *10*, 804. [CrossRef] [PubMed]
265. Zhu, S.; Zhou, H.; Hibino, M.; Honma, I.; Ichihara, M. Synthesis of MnO_2 nanoparticles confined in ordered mesoporous carbon using a sonochemical method. *Adv. Funct. Mater.* **2005**, *15*, 381–386.
266. Sun, B.; Liu, H.; Munroe, P.; Ahn, H.; Wang, G. Nanocomposites of CoO and a mesoporous carbon (CMK-3) as a high performance cathode catalyst for lithium-oxygen batteries. *Nano Res.* **2012**, *5*, 460–469.

267. Zheng, Z.; Wang, Y.; Zhang, A.; Zhang, T.; Cheng, F.; Tao, Z.; Chen, J. Porous Li_2FeSiO_4/C nanocomposite as the cathode material of lithium-ion batteries. *J. Power Sources* **2012**, *198*, 229–235. [CrossRef]
268. Yoo, H.; Jo, M.; Jin, B.-S.; Kim, H.-S.; Cho, J. Flexible morphology design of 3D-macroporous LiMnPO4 cathode materials for Li secondary batteries: Ball to flake. *Adv. Energy Mater.* **2011**, *1*, 347–351.
269. Thepkaew, J.; Therdthianwong, S.; Therdthianwong, A. Effect of pre-treatment approach of a carbon support on activity of PtSn/C electrocatalysts for direct ethanol fuel cells. *J. Appl. Electrochem.* **2011**, *41*, 435–444.
270. Naraprawatphong, R.; Chokradjaroen, C.; Thiangtham, S.; Yang, L.; Saito, N. Nanoscale advanced carbons as an anode for lithium-ion battery. *Mater. Today Adv.* **2022**, *16*, 100290. [CrossRef]
271. Zhang, K.; Hu, Z.; Chen, J. Functional porous carbon-based composite electrode materials for lithium secondary batteries. *J. Energy Chem.* **2013**, *22*, 214–225. [CrossRef]
272. Ryoo, R.; Joo, S.H.; Jun, S. Synthesis of highly ordered carbon molecular sieves via template-mediated structural transformation. *J. Phys. Chem. B* **1999**, *103*, 7743–7746. [CrossRef]
273. Hu, Z.; Srinivasan, M.P.; Ni, Y. Preparation of mesoporous high-surface-area activated carbon. *Adv. Mater.* **2000**, *12*, 62–65. [CrossRef]
274. Zeng, L.; Zheng, C.; Xi, J.; Fei, H.; Wei, M. Composites of V_2O_3–ordered mesoporous carbon as anode materials for lithium-ion batteries. *Carbon* **2013**, *62*, 382–388. [CrossRef]
275. Shen, X.; Mu, D.; Chen, S.; Wu, B.; Wu, F. Enhanced electrochemical performance of ZnO-loaded/porous carbon composite as anode materials for lithium ion batteries. *ACS Appl. Mater. Interfaces* **2013**, *5*, 3118–3125. [CrossRef]
276. Chen, A.; Li, C.; Tang, R.; Yin, L.; Qi, Y. MoO_2–ordered mesoporous carbon hybrids as anode materials with highly improved rate capability and reversible capacity for lithium-ion battery. *Phys. Chem. Chem. Phys.* **2013**, *15*, 13601–13610. [CrossRef]
277. Kwon, K.M.; Kim, I.G.; Lee, K.-Y.; Kim, H.; Kim, M.S.; Cho, W.I.; Choi, J.; Nah, I.W. α-Fe_2O_3 anchored on porous N doped carbon derived from green microalgae via spray pyrolysis as anode materials for lithium ion batteries. *J. Ind. Eng. Chem.* **2019**, *69*, 39–47. [CrossRef]
278. Wu, R.; Shen, S.; Xia, G.; Zhu, F.; Lastoskie, C.; Zhang, J. Soft-templated self-assembly of mesoporous anatase TiO_2/carbon composite nanospheres for high-performance lithium ion batteries. *ACS Appl. Mater. Interfaces* **2016**, *8*, 19968–19978. [CrossRef]
279. Chang, P.-y.; Huang, C.-h.; Doong, R.-a. Ordered mesoporous carbon–TiO_2 materials for improved electrochemical performance of lithium ion battery. *Carbon* **2012**, *50*, 4259–4268. [CrossRef]
280. Li, Y.; Zhu, L.; Yao, T.; Liu, T.; Qian, R.; Li, F.; Han, X.; Yu, L.; Wang, H. Space-confined synthesis of ultrasmall SnO2 nanodots within ordered mesoporous carbon CMK-3 for high-performance lithium ion batteries. *Energy Fuels* **2020**, *34*, 7709–7715. [CrossRef]
281. Wang, J.; Liu, Z.; Yang, W.; Han, L.; Wei, M. A one-step synthesis of porous V_2O_3@ C hollow spheres as a high-performance anode for lithium-ion batteries. *Chem. Commun.* **2018**, *54*, 7346–7349. [CrossRef] [PubMed]
282. Yang, Z.; Li, Z.; Li, P.; Gao, C.; Zhang, H. NiO/Ni nanocomposites embedded in 3D porous carbon with high performance for lithium-ion storage. *J. Mater. Sci.* **2020**, *55*, 1659–1672. [CrossRef]
283. Verrelli, R.; Hassoun, J. High-capacity NiO–(mesocarbon microbeads) conversion anode for lithium-ion battery. *ChemElectroChem* **2015**, *2*, 988–994. [CrossRef]
284. Qiu, B.; Guo, W.; Liang, Z.; Xia, W.; Gao, S.; Wang, Q.; Yu, X.; Zhao, R.; Zou, R. Fabrication of Co_3O_4 nanoparticles in thin porous carbon shells from metal–organic frameworks for enhanced electrochemical performance. *RSC Adv.* **2017**, *7*, 13340–13346. [CrossRef]
285. Mao, J.; Niu, D.; Zheng, N.; Jiang, G.; Zhao, W.; Shi, J.; Li, Y. Fe_3O_4-embedded and N-doped hierarchically porous carbon nanospheres as high-performance lithium ion battery anodes. *ACS Sustain. Chem. Eng.* **2019**, *7*, 3424–3433. [CrossRef]
286. Wang, H.; Wang, X.; Li, Q.; Li, H.; Xu, J.; Li, X.; Zhao, H.; Tang, Y.; Zhao, G.; Li, H. Constructing three-dimensional porous carbon framework embedded with $FeSe_2$ nanoparticles as an anode material for rechargeable batteries. *ACS Appl. Mater. Interfaces* **2018**, *10*, 38862–38871. [CrossRef]
287. Hou, L.; Xiong, S.; Cui, R.; Jiang, Y.; Chen, R.; Liang, W.; Gao, Z.; Gao, F. Three-Dimensional Porous Carbon Framework Confined Si@ TiO_2 Nanoparticles as Anode Material for High-Capacity Lithium-Ion Batteries. *ChemElectroChem* **2022**, *9*, e202101447. [CrossRef]
288. Hao, S.; Zhang, B.; Wang, Y.; Li, C.; Feng, J.; Ball, S.; Srinivasan, M.; Wu, J.; Huang, Y. Hierarchical three-dimensional Fe_3O_4@ porous carbon matrix/graphene anodes for high performance lithium ion batteries. *Electrochim. Acta* **2018**, *260*, 965–973. [CrossRef]
289. Luo, H.; Ji, D.; Yang, Z.; Huang, Y.; Xiong, G.; Zhu, Y.; Guo, R.; Wan, Y. An ultralight and highly compressible anode for Li-ion batteries constructed from nitrogen-doped carbon enwrapped Fe3O4 nanoparticles confined in a porous 3D nitrogen-doped graphene network. *Chem. Eng. J.* **2017**, *326*, 151–161. [CrossRef]
290. Wang, Y.; Gao, Y.; Shao, J.; Holze, R.; Chen, Z.; Yun, Y.; Qu, Q.; Zheng, H. Ultrasmall Fe_3O_4 nanodots within N-doped carbon frameworks from MOFs uniformly anchored on carbon nanowebs for boosting Li-ion storage. *J. Mater. Chem. A* **2018**, *6*, 3659–3666. [CrossRef]
291. Ma, F.-X.; Hu, H.; Wu, H.B.; Xu, C.-Y.; Xu, Z.; Zhen, L.; XW, D.L. Formation of Uniform Fe_3O_4 Hollow Spheres Organized by Ultrathin Nanosheets and Their Excellent Lithium Storage Properties. *Adv. Mater.* **2015**, *27*, 4097–4101. [CrossRef]

292. Xu, C.; Niu, D.; Zheng, N.; Yu, H.; He, J.; Li, Y. Facile synthesis of nitrogen-doped double-shelled hollow mesoporous carbon nanospheres as high-performance anode materials for lithium ion batteries. *ACS Sustain. Chem. Eng.* **2018**, *6*, 5999–6007. [CrossRef]
293. Pappas, G.S.; Ferrari, S.; Huang, X.; Bhagat, R.; Haddleton, D.M.; Wan, C. Heteroatom doped-carbon nanospheres as anodes in lithium ion batteries. *Materials* **2016**, *9*, 35. [CrossRef] [PubMed]
294. Ma, F.; Zhao, H.; Sun, L.; Li, Q.; Huo, L.; Xia, T.; Gao, S.; Pang, G.; Shi, Z.; Feng, S. A facile route for nitrogen-doped hollow graphitic carbon spheres with superior performance in supercapacitors. *J. Mater. Chem.* **2012**, *22*, 13464–13468. [CrossRef]
295. Friedel, B.; Greulich-Weber, S. Preparation of monodisperse, submicrometer carbon spheres by pyrolysis of melamine–formaldehyde resin. *Small* **2006**, *2*, 859–863. [CrossRef]
296. Sui, Z.-Y.; Wang, C.; Yang, Q.-S.; Shu, K.; Liu, Y.-W.; Han, B.-H.; Wallace, G.G. A highly nitrogen-doped porous graphene–an anode material for lithium ion batteries. *J. Mater. Chem. A* **2015**, *3*, 18229–18237. [CrossRef]
297. Yin, L.; Park, M.; Jeon, I.; Hwang, J.H.; Kim, J.P.; Lee, H.W.; Park, M.; Jeong, S.Y.; Cho, C.-R. Silicon nanoparticle self-incorporated in hollow nitrogen-doped carbon microspheres for lithium-ion battery anodes. *Electrochim. Acta* **2021**, *368*, 137630. [CrossRef]
298. Yarmolich, D.; Odarchenko, Y.; Murphy, C.; Petrucco, E.A.; Cookson, J.; Yarmolich, D.; Zhao, T.; Kim, H.-K.; Kumar, R.V.; Tomov, R.I. Novel binder-free carbon anode for high capacity Li-ion batteries. *Nano Energy* **2021**, *83*, 105816. [CrossRef]
299. Upadhyay, S.; Pandey, O. Studies on 2D-molybdenum diselenide ($MoSe_2$) based electrode materials for supercapacitor and batteries: A critical analysis. *J. Energy Storage* **2021**, *40*, 102809. [CrossRef]
300. Zhang, K.; Hu, Z.; Liu, X.; Tao, Z.; Chen, J. FeSe2 microspheres as a high-performance anode material for Na-ion batteries. *Adv. Mater.* **2015**, *27*, 3305–3309. [CrossRef]
301. Ge, P.; Cao, X.; Hou, H.; Li, S.; Ji, X. Rodlike Sb_2Se_3 wrapped with carbon: The exploring of electrochemical properties in sodium-ion batteries. *ACS Appl. Mater. Interfaces* **2017**, *9*, 34979–34989. [CrossRef]
302. Ge, P.; Hou, H.; Li, S.; Huang, L.; Ji, X. Three-dimensional hierarchical framework assembled by cobblestone-like $CoSe_2$@ C nanospheres for ultrastable sodium-ion storage. *ACS Appl. Mater. Interfaces* **2018**, *10*, 14716–14726. [CrossRef] [PubMed]
303. Yue, J.-L.; Sun, Q.; Fu, Z.-W. Cu_2Se with facile synthesis as a cathode material for rechargeable sodium batteries. *Chem. Commun.* **2013**, *49*, 5868–5870. [CrossRef] [PubMed]
304. Zhu, S.; Li, Q.; Wei, Q.; Sun, R.; Liu, X.; An, Q.; Mai, L. $NiSe_2$ nanooctahedra as an anode material for high-rate and long-life sodium-ion battery. *ACS Appl. Mater. Interfaces* **2017**, *9*, 311–316. [CrossRef] [PubMed]
305. Park, G.D.; Kim, J.H.; Kang, Y.C. Large-scale production of spherical $FeSe_2$-amorphous carbon composite powders as anode materials for sodium-ion batteries. *Mater. Charact.* **2016**, *120*, 349–356. [CrossRef]